Theses and Dissertations

Student Graduate Works

12-24-2015

Optimal Attitude Control of Agile Spacecraft Using Combined Reaction Wheel and Control Moment Gyroscope Arrays

Cole C. Doupe

OPTIMAL ATTITUDE CONTROL OF AGILE SPACECRAFT USING COMBINED REACTION WHEEL AND CONTROL MOMENT GYROSCOPE ARRAYS

DISSERTATION

Cole C. Doupe, Major, USAF

AFIT-ENY-DS-15-D-042

DEPARTMENT OF THE AIR FORCE
AIR UNIVERSITY

AIR FORCE INSTITUTE OF TECHNOLOGY

Wright-Patterson Air Force Base, Ohio

AFIT-ENY-DS-15-D-042

OPTIMAL ATTITUDE CONTROL OF AGILE SPACECRAFT USING COMBINED

REACTION WHEEL AND CONTROL MOMENT GYROSCOPE ARRAYS

DISSERTATION

Presented to the Faculty

Graduate School of Engineering and Management

Air Force Institute of Technology

Air University

Air Education and Training Command

in Partial Fulfillment of the Requirements for the

Degree of Doctor of Philosphy in Space Systems

Cole C. Doupe, B.S., M.S.

Major, USAF

December 2015

AFIT-ENY-DS-15-D-042

OPTIMAL ATTITUDE CONTROL OF AGILE SPACECRAFT USING COMBINED

REACTION WHEEL AND CONTROL MOMENT GYROSCOPE ARRAYS

Cole C. Doupe, B.S., M.S.
Major, USAF

Committee Membership:

Dr. Eric D. Swenson
Chair

Dr. Richard G. Cobb
Member

Major Scott J. Pierce
Member

ADEDEJI B. BADIRU, Ph.D.
Dean, Graduate School of Engineering
and Management

AFIT-ENY-DS-15-D-042

Abstract

This dissertation explores the benefits of combined control moment gyroscope (CMG) and reaction wheel array (RWA) actuation for agile spacecraft. Agile spacecraft are capable of slewing to multiple targets in minimum time. CMGs provide the largest torque capability of current momentum exchange actuation devices but also introduce singularity events in operation. RWAs produce less torque capability than CMGs but can achieve greater pointing accuracy. In this research, a combined RWA and CMG (RWCMG) system is evaluated using analytical simulations and hardware experiments. A closed-loop control scheme is developed which takes advantage of the strengths of each actuator set. The CMGs perform slews for a representative target field. Borrowing from variable-speed CMG theory, a system of switching between CMG and RWA actuation allows the RWA to assume control of the spacecraft when desired pointing tolerance is met for a given target. During collection, the CMG gimbals may travel along null motion trajectories toward preferred angles to prepare for the next slew. Preferred gimbal angles are pre-computed off-line using optimization techniques or set based on look-up tables. Logic is developed to ensure CMG gimbal angles travel the shortest path to the preferred values. The proportional-integral-derivative, quaternion feedback, and nonlinear Lyapunov-based controllers are assessed for the RWCMG system. Extended and unscented Kalman filter techniques are explored for improved accuracy in analytical simulation. Results of RWCMG hardware experiments show improvements in slew capability, pointing accuracy, and singularity avoidance compared to traditional CMG-only systems.

Acknowledgements

Table of Contents

List of Figures

List of Tables

List of Abbreviations

OPTIMAL ATTITUDE CONTROL OF AGILE SPACECRAFT USING COMBINED

REACTION WHEEL AND CONTROL MOMENT GYROSCOPE ARRAYS

I.   Introduction

Current imagery missions require agile satellites that are capable of slewing between targets in minimal time to maximize the amount of information collected. The main goal of this research is to improve upon existing approaches for agile spacecraft control. Control moment gyroscopes (CMG), are often the actuator of choice among satellite designers due to a relatively high torque output but require complex control algorithms to avoid mathematical errors and hardware issues called singularities [4–6]. Reaction wheels, another common attitude control actuator, typically have far less torque capability but have relatively simple control algorithms and do not risk encountering singularities [7]. Both CMG and reaction wheel hardware is fairly common and very mature in modern spacecraft; however, only one or the other actuator is currently used in a single spacecraft. Variable speed CMGs are essentially gyroscopes which have the capability to vary the rotor rate of rotation, acting as a combined CMG and reaction wheel. Variable speed CMGs are a frequently researched topic in existing literature but have never been implemented in hardware or flown in space since motors capable of varying the angular rate of gyroscope rotors would need to be much larger than constant speed motors and also require gimbals [8–13]. However, the equations of motion developed for variable speed CMGs are directly applicable to a system which combines traditional constant speed CMGs and reaction wheels, which is presented in this research. The extent of research on a system in which separate CMGs and reaction wheel arrays (RWA) are combined as a spacecraft (s/c) control system is quite limited [13; 14]. After an extensive search of the literature, no harware

1

testing of a combined RWA and CMG (RWCMG) control system has been documented. The pursuit of this research is to seek improvement in s/c slew times, pointing accuracy, and singularity avoidance by investigating the RWCMG control system first in analytical simulation and then in hardware experiments. This chapter begins with explaining the agile s/c mission which would benefit from a RWCMG control system. The section then introduces CMG actuation followed by a brief explanation of singularities. Next, it highlights the relevant technical disciplines involved with RWCMG research. Finally, research objectives and an overview of the entire document are given.

1.1 Motivation: Satellite Tracking Mission

The satellite imagery business has been booming and shows no trend of decline [15–19]. As seen from the recent search for missing Malaysia Airlines Flight 370, significant amounts of s/c imagery is often desired with extreme timeliness standards. The search for the missing aircraft initially employed imaging satellites to scan large area sweeps in an attempt to locate wreckage before the transmitter battery in the black box expired. Once a likely target area was discovered, satellite use shifted from wide-area sweeps to multiple point target imaging. Because the revisit time of low Earth orbit (LEO) satellites over a particular area on Earth is once a day on average, satellites need to be agile - have the ability to quickly slew attitude from one target to another - to collect the information in the least amount of time.

In order to accomplish the representative imaging mission of Figure 1.1, the s/c control actuators, whether CMGs or RWAs, must perform two basic functions: slew between targets and control a precise attitude to image a target for a desired duration, referred to as collect. With only one set of control actuators, the slew and collect functions must be accomplished by the same set of devices. This research seeks to evaluate a control system in which the CMGs perform the slew function, benefitting from their higher torque levels, and the RWA performs the collect function with their greater pointing accuracy. While the s/c is

2

performing the collect function on a target, the CMG array is not needed to provide control torque. During this time of control dormancy, CMG gimbal angles may be allowed to travel paths of null motion - generating zero torque output - to seek optimal angles with which to perform the slew function for the next target in the mission. Such a control scheme has not been previously investigated and is a key aspect of this RWCMG system research. To explain the necessary technical disciplines involved with research on the RWCMG system, a brief introduction to CMG actuation is first required.

1.2 Control Moment Gyroscope Actuation

Agile s/c typically contain an array of CMG actuators [20]. A single CMG consists of a rotor which rotates on either one or two gimbals. A single-gimbal CMG (SGCMG) has one gimbal and a double-gimbal CMG (DGCMG) has two gimbals. SGCMG use is more common than DGCMG due to hardware simplicity and is the configuration used in this research. The SGCMG geometry is illustrated in Figure 1.2. The rotor rotates with an angular momentum vector $\vec{h}_i$ which is fixed with respect to the rotor frame direction $\hat{r}_{i3}$ and gimbal frame direction $\hat{g}_{i3}$. The subscript i denotes the ith CMG in an array. The rotor spins at an angular rate of $\dot{\psi}$ in the direction shown by the arrow. The gimbal can rotate about the second gimbal frame axis $\hat{g}_{i2}$ through an angle of δ_i from the reference gimbal angle. Hash marks in Figure 1.2 represent bearings that allow the $\hat{g}_{i2}$ axis to spin but constrains all translation degrees of freedom. Typically, CMG gimbals are angled with respect to the s/c body frame an angle of $90 - \beta$ degrees. This β angle designates which two axes the CMG can control. In this example, torque can be generated in the plane defined by $\hat{g}_{i3}$ and $\hat{g}_{i1}$.

Arrays of CMGs allow torque to be exerted in all three body frame axes. A typical configuration for CMG arrays is the pyramid or tetrahedron as show in Figure 1.3. Four CMGs allow redundancy in the architecture. The angular momentum vectors $\vec{h}_i$ in Fig. 1.3 are not fixed with respect to the body frame $\hat{b}$ but are shown in the position when the corresponding δ_i angles are defined as zero. The moments of inertia of each CMG rotor in
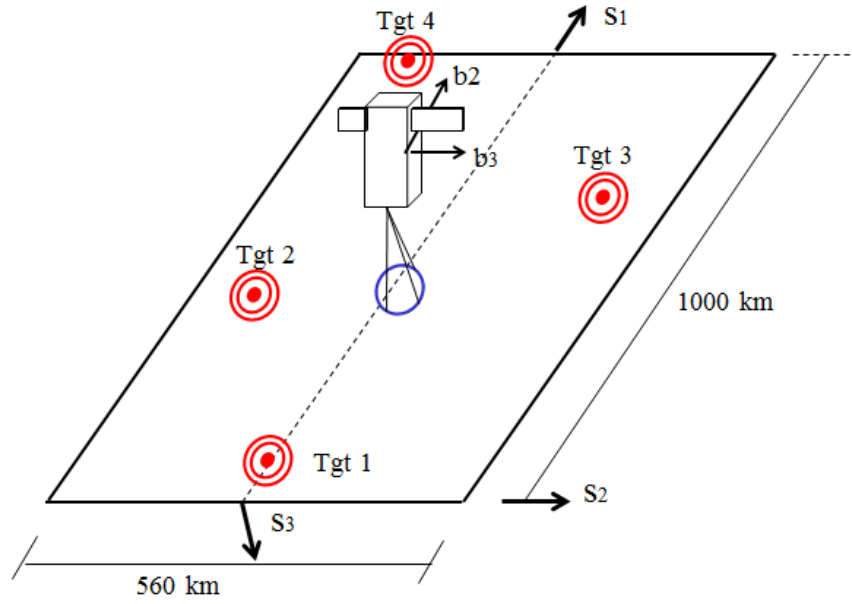
Figure 1.1: Representative 2D Multiple Target Observation Field
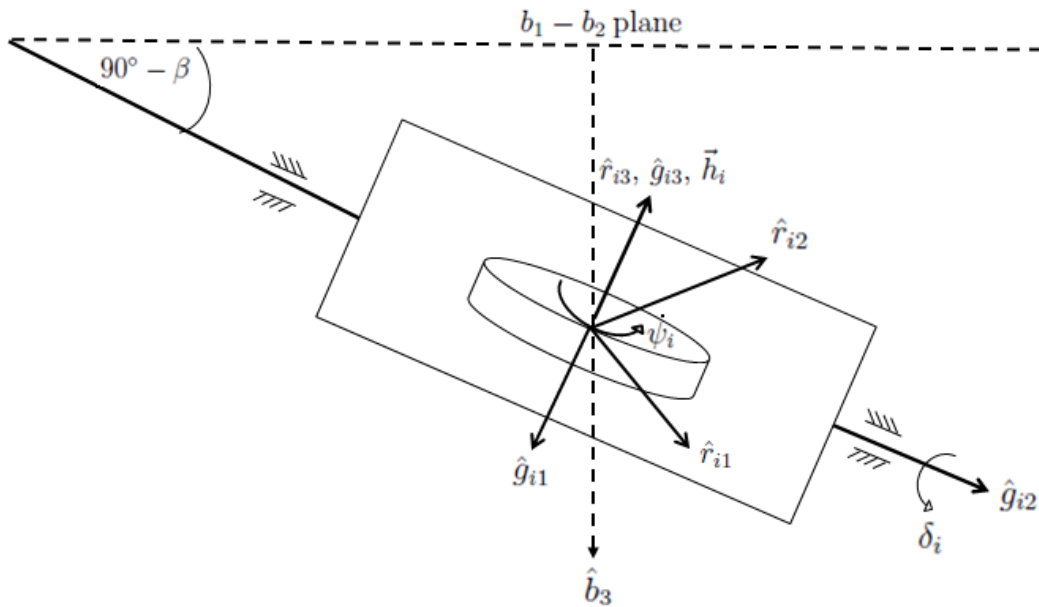
Figure 1.2: Single-Gimbal Control Moment Gyroscope Geometry
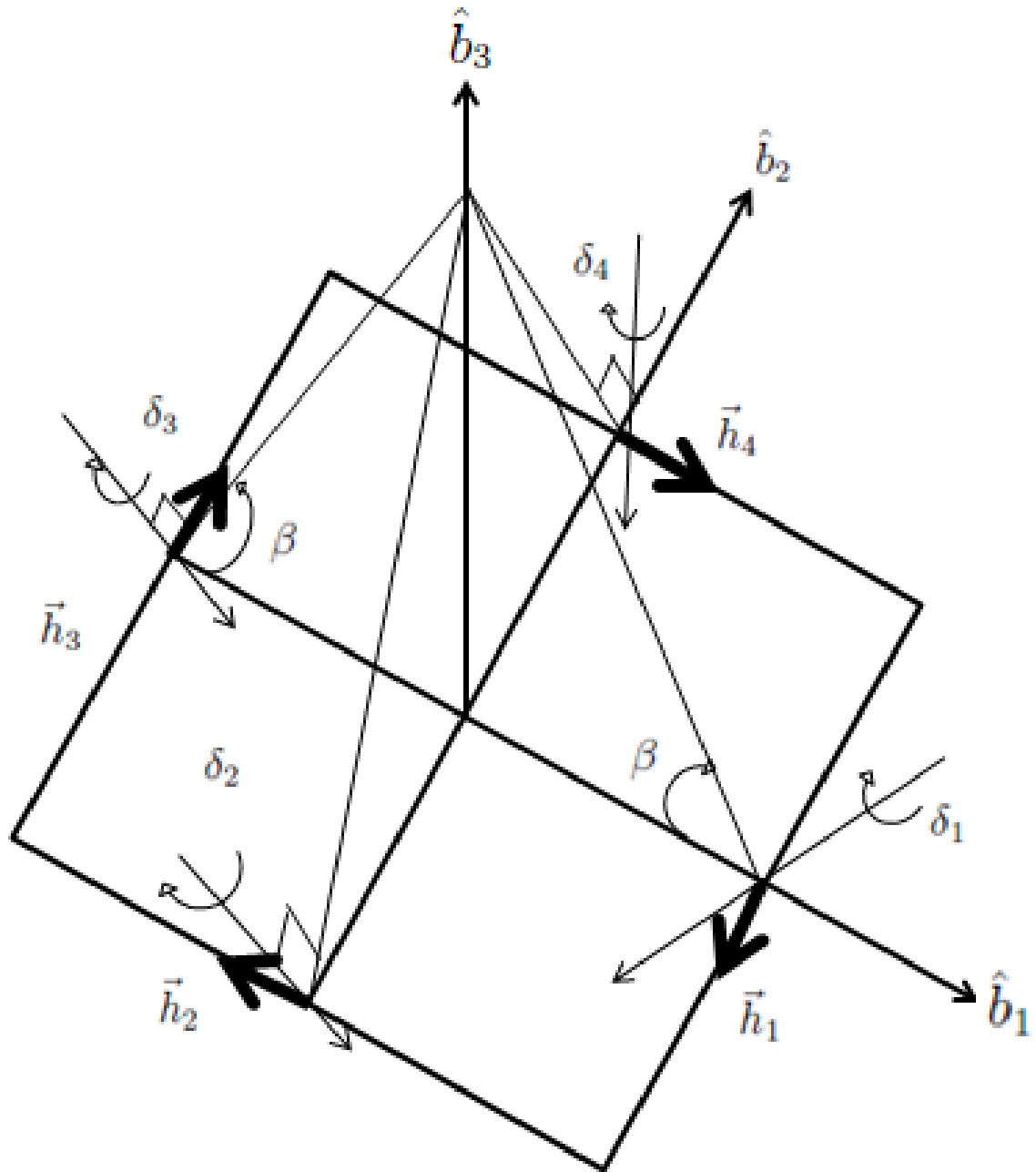
Figure 1.3: Four Control Moment Gyroscope Pyramid Geometry, Showing a Singularity with all $\vec{h}_i$ Lying in a Plane

the respective rotor frame $\hat{r}$ are assumed to be the same - all rotors are the same mass and dimensions. Since the rotors are typically circular disks, the moment of inertia about the $\hat{r}_1$ and $\hat{r}_2$ axes are the same while the moment of inertia for the $\hat{r}_3$ axis is larger than the moments about $\hat{r}_1$ and $\hat{r}_2$.

It is possible for the angular momentum vectors of all gyros to be arrayed in a two dimensional plane as shown in Fig. 1.3. A change in angular momentum in this plane is not possible until the desired angular momentum, some rotor rotation rates, or some gimbal angles change – this condition is called a singularity. This geometrical explanation of a CMG singularity, where all gimbal transverse axes lie in the same plane as the desired commanded torque, is commonly called gimbal lock. Gimbal array angular momentum capability is traditionally represented as a three dimensional surface. Example external and internal surface maps for unit CMG angular momentum are shown in Figure 1.4.
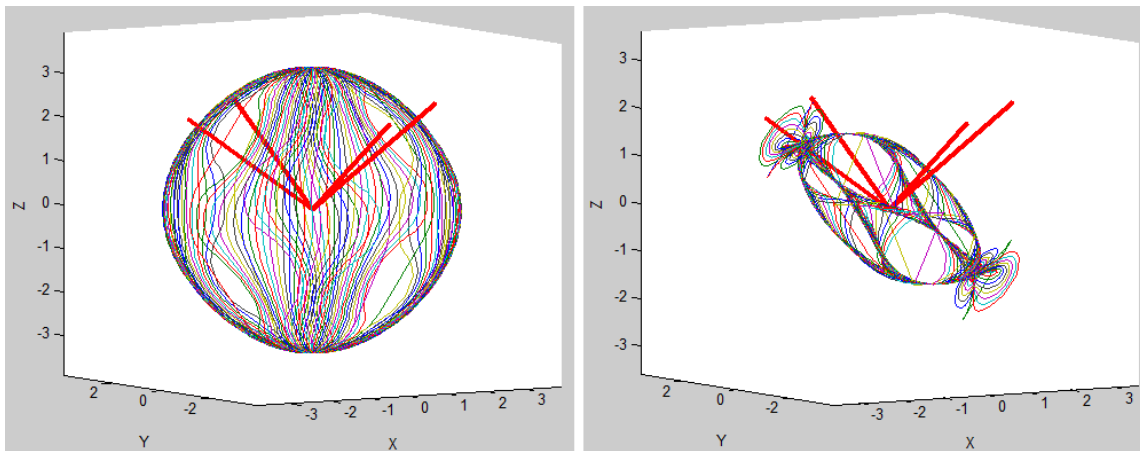
Figure 1.4: Maps of Standard Four-CMG Pyramid Unit Angular Momentum Space, External (left), Internal (right) (one of four shown) [1]

Axes in the surface map plots are the gimbal axes, and the holes around the axes show array angular momentums that are unachievable. Desired array angular momentum on or outside the external surface map are external singularities which are avoided by CMG array design. In other words, engineers know the dimensions, mass, and inertia properties of the

6

satellite when developing the attitude control system, and they typically over design rotor sizes, quantities of CMGs, and gimbal β angles to avoid external singularities. Holes in the internal surface map represent conditions such as gimbal lock. Internal singularities must be accounted for in control algorithms [8]. Further discussion of internal singularities is provided in Section 2.5.

Coupled tightly with the concept of CMG singular conditions is the concept of null motion. One key element of attitude control is ability to slew a satellite in any three-dimensional direction. Computing the CMG gimbal angle rotations for a four-CMG pyramid configuration, as in Figure 1.3, is an over determined problem - four gimbal rates for controlling three axes. For a traditional constant rotor rotation rate CMG array, there exists one degree of freedom in which gimbal angle trajectories can maneuver without theoretically imparting a torque on the s/c - this is referred to as null motion. If the CMG rotor rotation rates are variable, then this null space increases from one to five dimensions. However, based on an extensive search of literature and markets, VSCMG hardware to accomplish this control scheme does not currently exist. Motors that are capable of varying rotor rate present a serious mechanical challenge to gimbal. Alternatively, a combination of traditional constant speed four-CMG pyramid with one degree of null space can be combined with N separate reaction wheels to allow $1 + N$ degrees of null space. The same mathematical models can be used for both architectures. Combining CMG and RWA hardware allows investigation into how the null space can be used to improve agile s/c control. The overall goal of this research is to evaluate how one can take advantage of the high-torque capabilities of the CMG and the pointing accuracy advantages of the RWA to reduce mission completion time, reduce pointing error, and improve singularity avoidance. To the knowledge of the author, a RWCMG control scheme has not been tested in hardware experiments to date. Eight major technical disciplines require consideration in conducting this research and are introduced in the following section.

1.3 Relevant Research Areas

Efficient implementation of a combined control array for improving agile satellite actuation must begin with a study of the following research areas:

- Multiple Target Collection

- Variable Speed CMG Arrays

- Applicable Controllers

- Singularity Avoidance

- Null Motion

- Stochastic Estimation

- Preferred Gimbal Angles

- Applied Optimization

This section now presents an introductory preview of each of the relevant disciplines presented above to give the reader a better understanding of how each area is related to the overall research goals. Additionally, each research area is discussed in greater detail in Chapter II.

As explained in Section 1.1, multiple target collection involves imaging one target at a time and slewing between targets when a designated dwell time has been achieved on the current target. Wie [21] developed nonlinear feedback control algorithms for SGCMG-actuated rapid targeting of agile s/c. Wie's method employed a means to limit s/c slew rate and control input of the numerical simulation to add robustness to his approach. Nanamori [22] expanded on the work of Wie to implement preferred gimbal angles to multiple target collection. These preferred gimbal angles were only set at the beginning

of the multiple target mission for the first target. Nanamori showed that an initial off-line optimization of initial gimbal angles resulted in reduced power consumption and reduced internal disturbances from Wie's method of multiple target slews. In this presented research, various linear and nonlinear controllers are evaluated in a representative multiple target imaging mission. Null motion allows preferred gimbal angles to be sought during each collect phase for the following target.

Knowledge of the next area, VSCMG arrays, is the key in developing RWCMG equations of motion. As mentioned above, VSCMG equations can be adapted to traditional SGCMG systems by keeping CMG rotor spin rates $\dot{\psi}_i$ constant and VSCMG equations of motion can be adapted to reaction wheel-only systems by keeping gimbal rates $\dot{\delta}_i$ constant. Extending the concept further, VSCMG equations can also be used for a RWCMG system by treating each actuator as a VSCMG and holding the appropriate variable constant as described above. Schaub [8] derived VSCMG equations for control, null motion, and singularity avoidance. Schaub's textbook does not go so far as to apply the VSCMG equations to the multiple target slew application. Kim [10] developed a method for using null motion with VSCMGs to initially spin up the rotors during s/c commissioning without causing disturbance torque to the vehicle. The focus of the current research is not on initial spin-up of CMG's. However, the methods of incorporating null motion with VSCMG equations of motion are studied to implement null motion during imagery collection mode.

Critical to the design of a CMG attitude control system is an examination of applicable controllers. The standard proportional-integral-derivative (PID) controller is the most commonly used algorithm for CMG systems [23–29]. Using three gains - proportional, integral, and derivative - one can influence maneuver speed, overshoot, settling time, and steady-state error. Performance of the PID has been well documented in the literature for decades. Beyond the PID, Wie [27] recommended a form of saturated quaternion feedback control for the multiple target slew mission. Schaub [8] developed a third nonlinear

9

Lyapunov-based controller which incorporates the gyroscopic term in Eulers equations and allows for tracking a desired angular velocity trajectory. The Schaub nonlinear controller has appeal for the agile s/c application where ground targets are in motion from the perspective of the satellite. The PID, quaternion feedback, and nonlinear Lyapunov-based controllers are all tested in RWCMG analytical simulations and hardware experiments in this research to determine the best method of control for agile s/c application.

When using CMG arrays as actuators, a study of singularity avoidance and null motion theories are equally important. Wie [21] used a generalized singularity robust (SR) inverse in place of the standard pseudo inverse for solution of the gimbal angles. The Wie SR inverse method guaranteed escape from internal singularities (caused by numerical obstructions in control or steering logic) but came at the cost of transient pointing errors. Kurukowa [30] presented a survey of several singularity avoidance techniques including off-diagonal SR inverse steering and VSCMG techniques but concluded that no perfect steering law exists. He stated the method should be chosen based on mission requirements. Schaub [8] developed equations for VSCMG null motion. The null motion does not guarantee reorientation of gimbals between any two arbitrary angle/rotor rate sets without imparting torque, even with the added degrees of null space afforded by variable rotor rotation rates. Schaub's null motion equation is adapted in this presented research for seeking preferred gimbal angles during RWCMG imagery collect modes in order to reduce slew times and avoid singularities.

Using null motion with the RWCMG system requires minimizing disturbance torque. One tool for reducing the effect of noise signals in control systems is stochastic estimation. Generating accurate knowledge of system states, which include s/c attitude and attitude rates, is assisted with filtering techniques. Previous research in filtering for spacecraft simulations determined that Kalman filtering is computationally feasible for real-time application [31]. Though vibrations from null motion are mathematically avoided in the

10

analytical simulation of the current research, the Extended Kalman Filter and Unscented Kalman Filter are implemented in order to reduce measurement and dynamic noise. CMG gimbals traveling null motion trajectories in hardware experiments do impart a disturbance to the s/c regardless of mathematical attempts to avoid the phenomenon. Previous AFIT students created low-pass filters to diminish the effect of gyro corruption in the inertial measurement unit (IMU) [32]. Therefore, s/c states determined by the hardware simulator's IMU hold the required level of accuracy for characterization of the RWCMG system in the current research. Future external state measurement systems may allow stochastic filtering techniques which are used in the current analytical simulations to be adapted for use in hardware experiments and is a recommended topic for future research in Chapter V.

With s/c states accurately measured through filtering techniques, the next area needed to optimize RWCMG control performance is reorientation of CMG gimbals to preferred gimbal angles. Preferred gimbal angles reduce the likelihood of encountering internal singularities in CMG arrays during the ensuing slew maneuver. The technique was first discussed by Vadali [2]. Preferred gimbal angles were found by starting the optimization at a nearly saturated CMG configuration. Saturation as defined in the Vadali research meant all CMG angular momentum vectors were projected in the same direction. Vadali then backward integrated the CMG steering equation until the desired torque was achieved. Vadali's procedure produced a set of preferred initial gimbal angles which would not encounter an internal singularity during their entire trajectory to meet the desired attitude state. In addition, Vadali discovered a particular set of gimbal angles which provide singularity-free operation for most of the torque demand cases he studied. This set of gimbal angles $[45°, −45°, 45°, −45°]$, is used in this presented RWCMG research as one option for preferred gimbal angles. Another method of generating preferred gimbal angles is through the use of optimization techniques. Current literature suggests use of this technique off-line due to the required computational rigor [10; 22; 33]. Nanamori

11

[22] developed an optimization based on gimbal manipulability (null space), disturbance reduction, and error reduction (desired versus achieved torque), applied to the multiple target mission. Yet this technique still only treats the initial target of a set, and is performed off-line. Nanamori tested his algorithm in numerical simulation only - not in hardware experiments. An offline pseudo-spectral (PS) optimization method is applied in this presented RWCMG research to calculate preferred gimbal angles for the entire set of representative targets. The optimization seeks to find gimbal angles which decrease slew times and increase pointing accuracy. The Vadali angles and the offline optimized angles are also tested in analytical simulations and hardware experiments. A third preferred gimbal angle determination method, near real-time sequential quadratic programming optimization, is also investigated in analytical simulations. This third preferred gimbal angle calculation technique is designed to run during the first few seconds of s/c collect mode to optimize speed and accuracy of the next slew.

As already discussed, optimization techniques can be applied to a number of roles in the RWCMG mission. As mentioned above, calculation of preferred gimbal angles is one application. When designing an agile s/c, the goal is to slew to as many targets as possible in the shortest time possible. Therefore, a large portion of this research is focused on investigating applied optimization techniques. The optimization we discuss here is defined as a minimum time problem where the initial state, final attitude, and final angular rates are all constrained. Hardware limitations such as maximum gimbal rates and s/c slew rates are also added to provide realistic constraints on this challenging optimization problem. Final gimbal angles, gimbal rates, reaction wheel rotor rates, and reaction wheel accelerations are not fixed but are subject to said constraints. Optimal control solutions currently must be calculated off-line - not in real-time on the s/c computer - however they could be, provided robust computational hardware. These optimal control solutions may be fed-forward into open-loop controllers but are then susceptible to disturbance torques

and differences between the modeled and actual dynamics [3; 28; 34]. Adding closed-loop controllers to have the s/c track optimal momentum control solutions is a current area of research in this field. Feedback loops mitigate disturbances, but increase the chance of constraint violations. Wright [28] compared optimized PID controllers with optimal gimbal trajectory solutions found from PS methods in an open-loop controller. Karpenko [3] investigated a technique to combine pre-calculated optimal gimbal angles with a closed-loop feedback controller to decrease state wandering. The subject of using optimal solutions within a closed-loop control system is not the focus of this dissertation research. PS optimization is used in this research as a means to create a benchmark for measuring controller performance and for preferred gimbal angle calculation. Sequential quadratic programming methods are also used for preferred gimbal angle calculation.

The relevant disciplines introduced in this section form the boundaries in the intended area of research and are summarized in Figure 1.5. This presented research applies stochastic estimation, optimization, VSCMG array, and control techniques and pushes the known research boundaries in the areas of singularity avoidance, null motion, and preferred gimbal angles as applied to multiple target collection.

1.4   Research Objectives

This dissertation research investigates the use of a RWCMG attitude control system for agile s/c performing a multiple target mission. Development and analysis of a control scheme which takes advantage of high CMG torque levels and RWA accuracy capabilities is sought. The control strategy is to use a CMG array to perform slews for the agile s/c, then transition to RWA control during imagery collection. With the RWCMG system, additional dimensions of the null space are available with which to maneuver gimbal angles to preferred values during the collect mode, before slewing to each target. Investigation into the RWCMG system is conducted through both analytical simulation and hardware experiments.

13
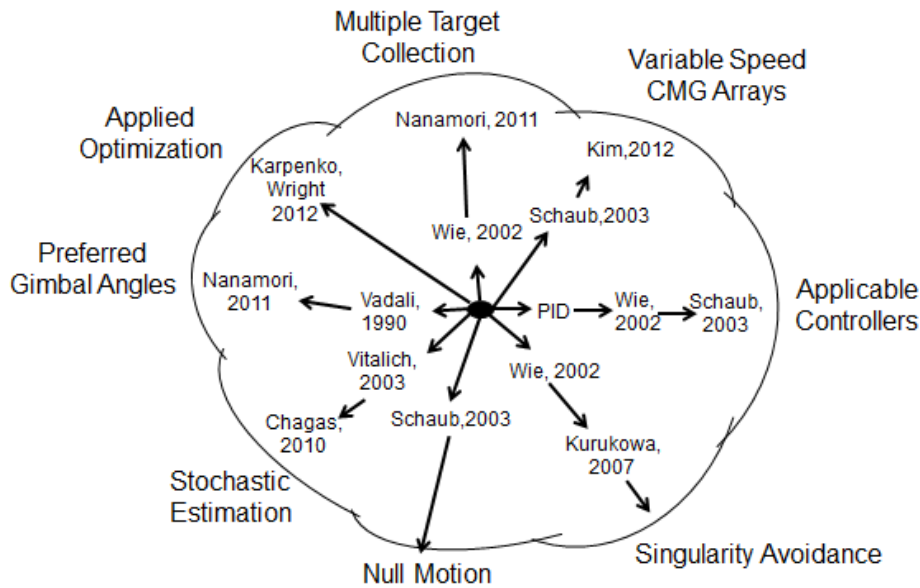
Figure 1.5: Bounds of Current Research for Agile CMG Systems

A RWCMG system was investigated by Verbin [35], however the research did not consider using null motion to adjust CMG gimbal angles and used four SGCMG in scissor pairs instead of a standard pyramid configuration. Verbin's research concluded with numerical simulations but did not include hardware experiments. One aspect included the research herein is characterization of disturbance torque created by CMG gimbal null motion - a phenomenon realized in actual hardware experiments. Since the intended null motion occurs during imagery collection, the RWA must be able to maintain pointing accuracy requirements despite small residual torques created from CMG null motion. The research in this dissertation seeks to determine how rapidly CMG gimbals can rotate along null motion trajectories while minimizing disturbance torque. In addition, the research seeks to determine if the RWCMG system improves agile s/c mission completion times, pointing error, and singularity avoidance as compared to a traditional SGCMG system. After conducting an extensive literature review of more than forty peer-reviewed journal articles, it is the author's opinion that the use of null motion to adjust gimbal angles between

targets in real time for an agile s/c with combined CMG and reaction wheel actuation has not been investigated prior to this research effort.

A closed-loop control scheme system using a selected controller and containing a RWCMG array is tested on a representative targeting mission in analytical simulation and hardware experiments. Targets are placed such that the order of collection is not ambiguous. The research is not focused on optimizing target order of collection. PS optimal solutions are generated to provide a benchmark to assess the closed-loop performance. Accuracy of target pointing, time required to complete the targeting mission, and singularity avoidance parameters are the metrics of interest for the research. Performance of controllers including PID, quaternion feedback, and nonlinear Lyapunov-based are tested for the RWCMG application. An algorithm which imposes representative hardware limitations is also developed for the analytical model to ensure constraints are enforced in the simulation. Investigation of preferred gimbal angles follows three tracks. First, preferred gimbal angles are computed off-line via PS optimization for each target. Second, a computationally feasible algorithm of determining preferred gimbal angles in near real-time, embedded within the closed-loop analytical control algorithm, is investigated. Third, the performance of the RWCMG system is tested using the Vadali universal preferred gimbal angles of $[45°, −45°, 45°, −45°]$ for CMGs one through four respectively [2]. Extended and unscented Kalman filter algorithms are separately used to mitigate noise corruption during the closed-loop control simulations of the analytical model. Performance of the simulation using the two filters is compared to quantify the performance benefit gained from the unscented Kalman filter over the extended Kalman filter.

Numerical simulation predictions are compared to hardware experiments with the Air Force Institute of Technology (AFIT) SimSat simulator. Logic for achieving preferred gimbal angles through the shortest gimbal path is applied to further reduce gimbal slew

15

time and null motion disturbance torque. Characterization of the null motion gain which determines the speed with which gimbals travel null motion trajectories is also enabled with hardware experimentation. Execution of the hardware experiment serves to prove many of the concepts investigated in the numerical simulation including controller performance and the impact of initial gimbal angles on mission metrics.

1.5   Dissertation Overview

Chapter II begins with introducing the relevant equations of motion for agile s/c controlled with RWCMG arrays. It then provides an in-depth review of each research area introduced in Section 1.3. Finally, the AFIT SimSat simulator is introduced to explain the hardware experiment setup.

Chapter III details the methodology of conducting the research. It starts with defining the agile spacecraft mission as interpreted for this research. Next, the closed-loop control scheme for the analytical RWCMG simulation is explained. Each component of the analytical scheme is addressed individually. Conversion of the analytical simulation model to the hardware experiment platform including installation of shortest path logic is addressed subsequently. Finally, means for assessing RWCMG performance are introduced.

Chapter IV first defines the specific metrics used to evaluate simulation and experiment performance. Controller performance for the RWCMG mission follows. Characterization of the algorithm which imposes constraints on the analytical simulation is next. Then null motion and preferred gimbal angle performance is evaluated. Results of tuning the null motion speed to minimize disturbance torque are discussed. Controller performance is revisited with respect to null motion. Preferred gimbal angle calculation methods are compared using performance metrics. Performance of the RWCMG system with less than optimal initial gimbal angles is also evaluated. Comparison of the RWCMG system to a

system with a pyramid of SGCMG actuators only follows. Finally, the stochastic estimation filters are assessed in the analytical simulation.

Chapter V provides a summary of the RWCMG research. Conclusions concerning the RWCMG results are offered and topics for future work in the research field are also recommended.

II.   Background

T his chapter provides a survey of the eight relevant research areas introduced in Section 1.3 which are required when conducting research in the area of multiple target satellite slews using reaction wheels and control moment gyroscopes as shown in Figure 1.5. To provide the technical context for the concepts involved with the areas, the chapter begins with an abbreviated derivation of s/c attitude dynamics equations of motion. The boundaries of current research in each of the eight areas are then covered in devoted sections. The goal of this chapter is to frame the boundaries which this research extends.

2.1   Equations of Motion

The equations of motion for attitude control of a satellite in space begin with Euler's equation

$$\vec{M}_{\hat{b}} = I_{\hat{b}}\dot{\vec{\omega}}_{\hat{b}}^{\hat{b}\hat{i}} + \vec{\omega}_{\hat{b}}^{\hat{b}\hat{i}} \times I_{\hat{b}}\vec{\omega}_{\hat{b}}^{\hat{b}\hat{i}} \tag{2.1}$$

where $\vec{M}_{\hat{b}}$ is a vector of the external torques applied to the s/c, normally limited to relatively small disturbance torques for s/c in orbit. A subscript $\hat{b}$ denotes the vector is represented in the s/c body reference frame. The s/c mass moment of inertia tensor is represented as the matrix $I_{\hat{b}}$ and the angular velocity vector of the body with respect to the inertial frame is $\vec{\omega}_{\hat{b}}^{\hat{b}\hat{i}}$. Note that the term $I_{\hat{b}}\vec{\omega}_{\hat{b}}^{\hat{b}\hat{i}}$ is the entire s/c angular momentum $\vec{h}_{\hat{b}}$. For the remainder of the chapter all s/c dynamics equations will be represented in the s/c body frame, unless otherwise noted, and the subscript $\hat{b}$ will now be dropped. The version of Euler's equation in Eq. (2.1) includes the assumption of a rigid body s/c. To include the effects of the actuators, the angular momentum of the actuators can be separated out as

$$\vec{h}_{tot} = \vec{h}_{s/c} + \vec{h}_{act} = I\vec{\omega}^{\hat{b}\hat{i}} + \vec{h}_{act}. \tag{2.2}$$

Next, substituting the expanded angular momentum term shown in Eq. (2.2) into Eq. (2.1) yields a useful version of Euler's equation

$$\vec{M} = \left[{}^{\hat{i}}\frac{d}{dt}\vec{h}_{tot} \right] = I\dot{\vec{\omega}}^{\hat{b}\hat{i}} + \dot{\vec{h}}_{act} + \vec{\omega}^{\hat{b}\hat{i}} \times (I\vec{\omega}^{\hat{b}\hat{i}} + \vec{h}_{act}). \tag{2.3}$$

To make use of this form, an expression of the actuator angular momentum in the body frame is needed. Referencing the geometry of the SGCMG shown in Fig. 1.2, the angular momentum $\vec{h}_{act}$ of the ith CMG is $I_r \vec{\omega}^{\hat{r}\hat{i}}$. Discussion of rotating gimbals according to β angles and treating CMG clocking follows development of equations for a single CMG below.

The mass moment of inertia of the CMG in the rotor frame is the diagonal matrix shown in Eq. (2.4) where A_r is the inertia about the non-spin axes and C_r is the inertia of the rotor about the spin axis, $\hat{r}_{i3}$.

$$(I_r)_{\hat{r}} = \begin{bmatrix} A_r & 0 & 0 \\ 0 & A_r & 0 \\ 0 & 0 & C_r \end{bmatrix} \tag{2.4}$$

A transformation from the rotor frame to the body frame for use in Euler's equation can be accomplished with the operation

$$(I_r)_{\hat{b}} = R^{\hat{b}\hat{r}}(I_r)_{\hat{r}}R^{\hat{r}\hat{b}} \tag{2.5}$$

where $R^{\hat{b}\hat{r}}$ is the rotation matrix which converts from the rotor frame to the body frame. The rotation matrix $R^{\hat{b}\hat{r}}$ is formed by first rotating from the rotor frame to the gimbal frame through an angle of $-\psi_i$, then rotating from the gimbal frame to the body frame through an angle of $-\delta_i$. However, the rotor angle ψ_i is mathematically eliminated in the matrix multiplications and is not tracked or known.

The s/c angular velocity vector of the rotor with respect to the inertial frame $\vec{\omega}^{\hat{r}\hat{i}}$ is the combination

$$\vec{\omega}^{\hat{r}\hat{i}} = \vec{\omega}^{\hat{r}\hat{b}} + \vec{\omega}^{\hat{b}\hat{i}}. \tag{2.6}$$

19

The angular velocity of the body with respect to the inertial frame $\vec{\omega}^{\hat{b}\hat{i}}$ is defined as $\omega_{i1}\hat{b}_{i1} + \omega_{i2}\hat{b}_{i2} + \omega_{i3}\hat{b}_{i3}$ and the angular velocity of the CMG rotor with respect to the body frame is

$$\vec{\omega}^{\hat{r}\hat{b}} = \dot{\psi}_i \hat{r}_{i3} + \dot{\delta}_i \hat{g}_{i2} = \dot{\psi}_i R^{\hat{b}\hat{g}} \hat{g}_{i3} + \dot{\delta}_i R^{\hat{b}\hat{g}} \hat{g}_{i2}. \tag{2.7}$$

The rotation matrix $R^{\hat{b}\hat{g}}$ is a two-rotation through the angle $-\delta_i$.

Now with the angular momentum defined, some assumptions are in order to keep expressions simple without removing any important terms. First, we assume the rotor is a typical flywheel (oblate) with $C_r \approx 2A_r$. Second, the spin rate of the rotor $\dot{\psi}_i$ is much faster than the spin rates of the gimbal $\dot{\delta}_i$ and s/c slew rates ω_i. Therefore, $\dot{\psi} >> \omega_i$ and $\dot{\psi} >> \dot{\delta}_i$. Typical CMG rotors spin in the tens of thousands of radians per second (rad/s) while gimbal spin rates typically do not exceed one or two rad/s. With these assumptions, the single SGCMG angular momentum equation simplifies to

$$\vec{h}_{act} = R_i^{\hat{b}\hat{g}} \begin{bmatrix} 0 \\ 0 \\ C_{r_i}\dot{\psi}_i \end{bmatrix} \tag{2.8}$$

where the angular momentum of the gimbal assembly is neglected because it is so much smaller than the rotor angular momentum.

To transition from a single SGCMC set of equations to an array of SGCMGs, the $\vec{h}_{act}$ term in Euler's equation must contain the sum of each individual SGCMG: $\vec{h}_{act}$ is $\sum_{i=1}^{N} \left(R_i^{\hat{b}\hat{g}} \begin{bmatrix} 0 & 0 & C_{r_i}\dot{\psi}_i \end{bmatrix}^T \right)$ where there are N CMGs. However, now the rotation matrices $R_i^{\hat{b}\hat{g}}$ must also translate the gimbal clocking within the body frame. Each satellite CMG array will require a unique set of $R^{\hat{b}\hat{g}}$ matrices depending on hardware configuration and how the reference frames are defined. For an example of this clocking, consider a satellite with four SGCMGs in a pyramid configuration as shown in Figure 1.3. A mapping of each gimbal frame to the body frame is desired and each SGCMG must be analyzed separately. A diagram showing the specific geometry of SGCMG Number 4 from Figure 1.3 is shown

20

in Figure 2.1. First, we align $\hat{g}_{43}$ with $+\hat{b}_1$ via a 2-rotation about $\hat{g}_{42}$ over an angle of $-\delta_4$.
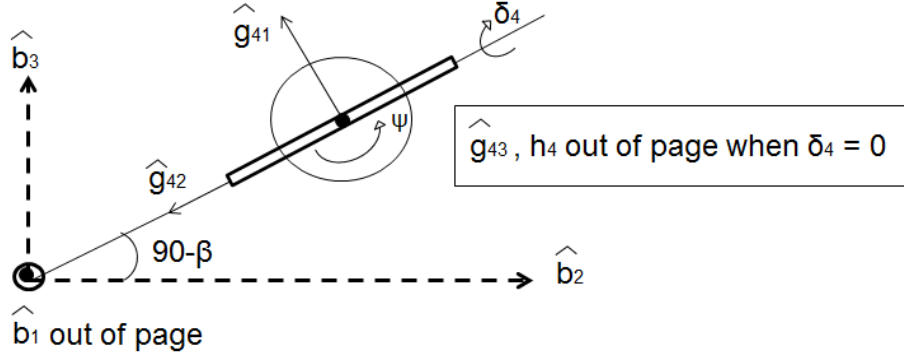
Figure 2.1: SGCMG Number 4 Geometry in Pyramid Array

Next, a 3-rotation about $\hat{g}_{43}$ over an angle of β aligns $\hat{g}_{41}$ with $-\hat{b}_2$ and $\hat{g}_{42}$ with $-\hat{b}_3$. To capture this clocking for the gimbal frame mapped to the body frame for SGCMG 4, a final rotation matrix is needed which places body frame components on the rows and gimbal frame components on columns to match the pairings mentioned above. The full $R^{\hat{b}\hat{g}}$ for SGCMG 4 in the pyramid configuration is

$$
R_4^{\hat{b}\hat{g}} = \begin{bmatrix} 0 & 0 & 1 \\ -1 & 0 & 0 \\ 0 & -1 & 0 \end{bmatrix} R_3(\beta)R_2(-\delta_4). \tag{2.9}
$$

Rotation matrices for each of the other SGCMGs are found using the same technique, which are

$$
R_1^{\hat{b}\hat{g}} = \begin{bmatrix} -1 & 0 & 0 \\ 0 & 0 & -1 \\ 0 & -1 & 0 \end{bmatrix} R_3(\beta)R_2(-\delta_1), \tag{2.10}
$$

$$
R_2^{\hat{b}\hat{g}} = \begin{bmatrix} 0 & 0 & -1 \\ 1 & 0 & 0 \\ 0 & -1 & 0 \end{bmatrix} R_3(\beta)R_2(-\delta_2), \tag{2.11}
$$

21

and

$$R_3^{\hat{b}\hat{g}} = \begin{bmatrix} 1 & 0 & 0 \\ 0 & 0 & 1 \\ 0 & -1 & 0 \end{bmatrix} R_3(\beta)R_2(-\delta_3). \tag{2.12}$$

The angular momentum vector $\vec{h}_{act}$ now has multiple δ_i in each position. An RWCMG array becomes more complicated still with both CMG terms and RWA terms. Therefore a Jacobian matrix is needed to calculate the derivative of angular momentum, or torque vector, $\dot{\vec{h}}_{act}$. The Jacobian matrix components are found from the partial derivatives of the angular momentum vector with respect to each CMG δ_i and RWA $\dot{\psi}_i$. The Jacobian matrix will have dimension 3xN where N is the total number of actuators in the array. For a traditional pyramid of SGCMGs, the Jacobian is a 3x4 matrix, and for the RWCMG system with four CMGs and three reaction wheels, the Jacobian is a 3x7 matrix. The Jacobian can treat the case of traditional SGCMGs combined with reaction wheels. A reaction wheel is represented by holding $\dot{\delta}_i$ as zero - fixing the reaction wheel momentum vector in place with respect to the s/c body - and considering only the $\dot{\psi}$ terms. To display the form of the actuator torque equation via Jacobian matrix for a pyramid of four constant speed CMGs (CSCMG) and three reaction wheels, we start by defining the Jacobian matrix $A(\dot{\vec{\psi}}, \vec{\delta})$

$$A(\dot{\vec{\psi}}, \vec{\delta}) = \begin{bmatrix} \frac{\partial \vec{h}(1)}{\partial \dot{\psi}_{RW_1}} & \frac{\partial \vec{h}(1)}{\partial \dot{\psi}_{RW_2}} & \frac{\partial \vec{h}(1)}{\partial \dot{\psi}_{RW_3}} & \frac{\partial \vec{h}(1)}{\partial \delta_{CMG_1}} & \frac{\partial \vec{h}(1)}{\partial \delta_{CMG_2}} & \frac{\partial \vec{h}(1)}{\partial \delta_{CMG_3}} & \frac{\partial \vec{h}(1)}{\partial \delta_{CMG_4}} \\ \frac{\partial \vec{h}(2)}{\partial \dot{\psi}_1} & \cdots & & & & \cdots & \frac{\partial \vec{h}(2)}{\partial \delta_4} \\ \frac{\partial \vec{h}(3)}{\partial \dot{\psi}_1} & \cdots & & & & \cdots & \frac{\partial \vec{h}(3)}{\partial \delta_4} \end{bmatrix} \tag{2.13}$$

where the actuator subscript on the angular momentum terms is intended but dropped for compactness. The $\dot{\psi}_i$ denominators are with respect to RWA spin rates while the δ_i

denominators are with respect to CMG gimbal angles. The s/c torque equation is then

$$\dot{\vec{h}}_{act} = A(\dot{\vec{\psi}}, \vec{\delta}) \begin{bmatrix} \ddot{\psi}_{RW_1} \\ \ddot{\psi}_{RW_2} \\ \ddot{\psi}_{RW_3} \\ \dot{\delta}_{CMG_1} \\ \dot{\delta}_{CMG_2} \\ \dot{\delta}_{CMG_3} \\ \dot{\delta}_{CMG_4} \end{bmatrix}. \tag{2.14}$$

For ease of notation, the array $[\ddot{\vec{\psi}}_i, \dot{\vec{\delta}}_i]^T$ is defined as $\dot{\vec{Y}}$. Inserting all above definitions of terms back into Eq. (2.3) and assuming no disturbance torques by setting $\vec{M}$ to zero yields

$$\vec{0} = I\dot{\vec{\omega}}^{\hat{b}\hat{i}} + A(\dot{\vec{\psi}}, \vec{\delta})\dot{\vec{Y}} + \vec{\omega} \times \left(I\vec{\omega}^{\hat{b}\hat{i}} + \sum_{i=1}^{N} \left(R_i^{\hat{b}\hat{g}} \begin{bmatrix} 0 & 0 & C_{r_i}\dot{\psi}_i \end{bmatrix}^T \right) \right) \tag{2.15}$$

where $\dot{\vec{\omega}}^{\hat{b}\hat{i}}$ is the s/c angular acceleration. Solving Eq. (2.15) for angular acceleration $\dot{\vec{\omega}}$, dropping the b-frame with respect to inertial frame superscripts, and combining momentum-based terms results in the deceptively simplified version of Euler's equation

$$\dot{\vec{\omega}} = -I^{-1}(\vec{u} + \vec{\omega} \times I\vec{\omega}). \tag{2.16}$$

The control input $\vec{u}$ in Eq. (2.16) is a 3x1 vector of the form

$$\vec{u} = A(\dot{\vec{\psi}}, \vec{\delta})\dot{\vec{Y}} + \vec{\omega} \times \vec{h}_{act} = \dot{\vec{h}}_{act} + \vec{\omega} \times \vec{h}_{act}. \tag{2.17}$$

The actuator torque $\dot{\vec{h}}_{act}$ is specified by the controller as $\vec{u} - \vec{\omega} \times \vec{h}_{act}$.

In order to find rates of change of gimbal angles and reaction wheel rotation rates, we must solve Eq. (2.14) for $\dot{\vec{Y}}$. Since $A(\dot{\vec{\psi}}, \vec{\delta})$ is not a square matrix, computing $\dot{\vec{Y}}$ typically uses some form of a pseudo-inverse. The most basic is the Moore-Penrose pseudo-inverse

$$\dot{\vec{Y}} = A^T(AA^T)^{-1}\dot{\vec{h}}_{act}. \tag{2.18}$$

23

Several papers in the literature treat this problem and show that better forms of the inverse calculation exist with benefits to singularity avoidance [9; 36–40]. Further discussion of the $\dot{\vec{Y}}$ calculation is given in Section 2.5.

The final set of equations needed to study satellite attitude control is a set of kinematic relations. Quaternions are typically used to express s/c body frame orientation with respect to the inertial frame. The quaternion differential equation is

$$
\begin{bmatrix} \dot{q}_1 \\ \dot{q}_2 \\ \dot{q}_3 \\ \dot{q}_4 \end{bmatrix} = \frac{1}{2} \begin{bmatrix} 0 & \omega_3 & -\omega_2 & \omega_1 \\ -\omega_3 & 0 & \omega_1 & \omega_2 \\ \omega_2 & -\omega_1 & 0 & \omega_3 \\ -\omega_1 & -\omega_2 & -\omega_3 & 0 \end{bmatrix} \begin{bmatrix} q_1 \\ q_2 \\ q_3 \\ q_4 \end{bmatrix} = \frac{1}{2} \begin{bmatrix} q_4 & -q_3 & q_2 \\ q_3 & q_4 & -q_1 \\ -q_2 & q_1 & q_4 \\ -q_1 & -q_2 & -q_3 \end{bmatrix} \begin{bmatrix} \omega_1 \\ \omega_2 \\ \omega_3 \end{bmatrix}. \tag{2.19}
$$

Quaternions are defined as:

$$
\begin{aligned}
q_1 &= e_1 \sin(\theta/2) \\
q_2 &= e_2 \sin(\theta/2) \\
q_3 &= e_3 \sin(\theta/2) \\
q_4 &= \cos(\theta/2)
\end{aligned} \tag{2.20}
$$

where $\hat{e}$ is a unit vector along the Euler axis, e_i are the direction cosines of the Euler axis between the body frame and inertial frame, and θ is the rotation angle about the Euler axis [27].

The above development forms a foundation in the equations of motion for RWCMG arrays. The equations presented in this section will form the backbone for the following discussions of relevant areas to the agile s/c control problem. Section 2.2 begins the tour of Figure 1.5 starting at the top with Multiple Target Collection.

2.2 Multiple Target Collection

The first stop on a clockwise tour around the boundaries of relevant technical areas of Figure 1.5 is the multiple target collection spoke. Wie [21] took steps toward developing a control law for agile s/c. He presented a three-axis quaternion feedback controller with

slew rate and control saturation limits. The Wie article included a generalized singularity-robust pseudo-inverse approach that he tested in numerical simulations while executing two successive large angle maneuvers.

Wie's controllers in [21] used a cascade-saturation logic meaning the quaternion states do not appear in the angular rate state equations. Equation (2.21) adapted from [21], with the syntax used in this presented dissertation, demonstrates this technique

$$
\begin{aligned}
\dot{\underline{q}} &= -\tfrac{1}{2}\vec{\omega} \times \underline{q} \pm \tfrac{1}{2}\sqrt{1 - \left\lVert \underline{q} \right\rVert^2}\,\vec{\omega} \\
\dot{q}_4 &= -\tfrac{1}{2}\omega^T \underline{q} \\
\dot{\vec{\omega}} &= I^{-1}(-\vec{\omega} \times I\vec{\omega} + \vec{u})
\end{aligned}
\tag{2.21}
$$

where $\underline{q}$ is a vector consisting of q_1, q_2, and q_3. When defining a control input $\vec{u}$, [21] used a saturation function defined as

$$
\operatorname*{sat}_{L_i}(\vec{x}) =
\begin{bmatrix}
\operatorname*{sat}_{L_1}(x_1) \\[4pt]
\operatorname*{sat}_{L_2}(x_2) \\[4pt]
\vdots \\[4pt]
\operatorname*{sat}_{L_n}(x_n)
\end{bmatrix}
\tag{2.22}
$$

where $\operatorname*{sat}_{L_i}(x_i)$ is defined as

$$
\operatorname*{sat}_{L_i}(x_i) =
\begin{cases}
L_i & \text{if} & x_i > L_i \\
x_i & \text{if} & -L_i \le x_i \le L_i \\
-L_i & \text{if} & x_i < L_i
\end{cases}
\tag{2.23}
$$

The slew rate limit L_i is computed from $(c/2k)\min(\sqrt{4a_i|q_{e_i}|}, |\omega_i|_{\max})$ where a_i is the maximum control acceleration limit. Then, the cascade saturation control logic used by Wie [21] is

$$
\begin{aligned}
\vec{\tau} &= -I^{-1}(2k\operatorname*{sat}_{L_i}(\vec{q}_e + \tfrac{1}{T}\int \vec{q}_e) + c\vec{\omega}) \\
\vec{u} &= \operatorname*{sat}_{U}(\vec{\tau})
\end{aligned}
\tag{2.24}
$$

where k and c are gains to be determined, $\vec{q}_e$ is the quaternion error, U is the saturation limit of each control input, and $\vec{\tau}$ is the control torque input. For SGCMG gimbal rates, Wie [21]

used a generalized SR inverse to solve the torque equation, where Wie's SR method is discussed further in Section 2.5. A numerical simulation of two successive large angle maneuvers was the extent of the work in [21]. The simulation showed that the control logic kept s/c slew rates within the desired slew rate constraints, but the authors did not show tracking accuracy metrics during the slew maneuvers. The paper gave a short discourse on the potential application of this theory to multiple target collection, but did not provide documentation on any simulations.

Following the work of Wie, Nanamori [22] developed a method of optimizing initial SGCMG gimbal angles prior to a multiple target agile s/c trajectory mission. Nanamori recognized that a SR method of solving the torque equation can cause chatter in the gimbals as the algorithm attempts to navigate past a singularity. The goal of Nanamori's optimization was to reduce internal disturbances and increase efficiency of the control solution found in Wie [21]. Thus, Nanamori developed three metrics to quantify this negative behavior as well as the resulting torque error. First was manipulability S_1 defined by

$$S_1(\delta_{0_1}, \delta_{0_2}, \delta_{0_3}, \delta_{0_4}) = \begin{cases} \frac{1}{\text{avg}(m)} & \text{if} \quad \min(m) > m_0 \\ \frac{1}{\text{avg}(m)} \times p & \text{if} \quad \min(m) \leq m_0 \end{cases} \tag{2.25}$$

where m is defined as $\sqrt{\det(AA^T)}$ and p is a penalty factor. The second metric defined in [22] was the inner disturbance S_2 which is described as being due to mechanical and electromagnetic factors by

$$S_2(\delta_{0_1}, \delta_{0_2}, \delta_{0_3}, \delta_{0_4}) = \sum_i^3 \int_{t0}^{tf} |T_{di}| dt \tag{2.26}$$

where T_{di} are the mechanical and electromagnetic disturbances. The third metric was disturbance torque S_3 described as

$$S_3(\delta_{0_1}, \delta_{0_2}, \delta_{0_3}, \delta_{0_4}) = \sum_i^3 \int_{t0}^{tf} |\Delta\tau_{\text{error}_i}| dt \tag{2.27}$$

where $\Delta\tau_{\text{error}_i}$ is the output torque error in the roll, pitch, and yaw axes. Nanamori placed the S_1, S_2, and S_3 metrics into an objective function for an optimization. The goal of the

26

optimization was to calculate the optimal initial gimbal angles δ_i to minimize this objective function for a multiple target satellite slew mission. The optimization included a weighted SR inverse when computing gimbal rates similar to that used in [21]. The design points for the optimization were limited to those gimbal angles which could be achieved through thirty seconds of null motion, starting from each gimbal initially set to zero degrees. The optimization for initial gimbal angles in [22] occurred off-line and only one set of initial gimbal angles was calculated for an entire target deck. Optimal initial gimbal angles were not calculated for each target in a particular multiple target mission. Nanamori concluded that the technique of optimizing initial gimbal angles based on manipulability, inner disturbance, and torque error resulted in almost three times less energy consumption and fifty percent less internal disturbance for agile s/c missions than the Wie method.

A form of the Wie saturation control logic is tested as one controller option for the RWCMG system in the presented research and is detailed further in Sections 2.4 and 3.2.2. Nanamori's concept of using null motion to seek preferred gimbal angles before an agile spacecraft mission starts is expanded in the RWCMG system such that the null motion is performed for every target during the mission. Further discussion of RWCMG null motion and preferred gimbal angles is found in Sections 2.6 and 2.8. Wie [21] and Nanamori [22] both used traditional SGCMGs as actuators in their multiple target collection algorithms and simulations. The following section shifts to the research area of VSCMG arrays and how the concept is adapted for use in the RWCMG system.

2.3 Variable Speed Control Moment Gyroscope Arrays

Now we will discuss past research in the area of VSCMG array use which was used for developing equations for a system with combined CMGs and reaction wheels. As mentioned in Sections 1.2 and 2.1, the equations of motion for VSCMG array actuation are directly applicable to RWCMG actuation. Schaub [8] derived VSCMG array equations of motion as well as equations for control steering, null motion, and singularity avoidance

27

of VSCMGs. By holding the ith CMG rotor rotation rate $\dot{\psi}_i$ constant, the ith VSCMG behaves as a SGCMG. Conversely, holding the ith VSCMG gimbal rate $\dot{\delta}_i$ constant, the ith VSCMG will behave as a reaction wheel. The remainder of this document will reference Schaub's VSCMG equations of motion adapted to a RWCMG, which is the intended topic of this presented research. The equations of motion in [8] were developed based on a slightly different geometric viewpoint than those shown in Section 2.1, but are identical after translating syntaxes. Schaub's control equations will be covered in Section 2.4 and null motion equations in Section 2.6.

In addition to the basic CMG pyramid array equations of motion, [8] provided a weighted Moore-Penrose inverse solution to the torque Eq. (2.14). The weights determine which mode (reaction wheel versus CMG) is active at each time step of operation. The Schaub inverse is

$$\begin{bmatrix} \ddot{\vec{\psi}} \\ \dot{\vec{\delta}} \end{bmatrix} = WA^T(AWA^T)^{-1}\dot{\vec{h}}_{act} \tag{2.28}$$

where W is a square diagonal matrix of weights. The number of terms in the diagonal of W is the same as the number of terms in $\dot{\vec{Y}}$. If the s/c control system consists of three reaction wheels and four SGCMGs, W would be of dimension 7x7. Setting the ith diagonal value to zero essentially turns the ith actuator off by not allowing a torque to be commanded from this actuator. Schaub avoids singularities with this algorithm by holding the weights corresponding to CMG gimbal rates constant and adjusting the reaction wheel weights based on a metric ν which represents a measure of how close the system is to a SGCMG singularity from

$$\nu = \det \frac{1}{h_0^2}(A(\vec{\delta})A(\vec{\delta})^T) \tag{2.29}$$

where h_0 is the nominal CMG angular momentum (assumed the same for all CMGs in the array) and $A(\vec{\delta})$ are the N columns of the A matrix corresponding to the N SGCMGs. This singularity measure indicates the closeness of the CMG gimbal angles to causing a rank deficiency in the A matrix and is similar to Nanamori's manipulability metric [22]. Then,

28

the reaction wheel weights are adjusted based on the equation

$$w_{\psi i} = w_{\psi i}^0 e^{-\mu \nu} \tag{2.30}$$

where $w_{\psi i}^0$ and μ are positive scalars. Equation (2.28) allows the CMGs to avoid a singularity caused by a rank deficiency in the $A(\vec{\delta})$ matrix. Equations (2.28) through (2.30) are used in the RWCMG system to control the s/c during slew modes and calculate singularity metrics. Further discussion of the weighted pseudo-inverse occurs in Section 3.2.3.

Following the derivations provided in [8], Kim [10] developed an adaptive controller for a pyramid VSCMG array. The controller used null motion with the goal of spinning CMG flywheels up from rest to a desired rotation rate without causing disturbance to the satellite. Similar to [8], Kim used flywheel acceleration and gimbal rates as control inputs. The controller developed in [10] proved capable of global asymptotic attitude tracking, avoided singularities, and managed internal momentum during numerical simulations to spin up VSCMG rotors to a desired rate. The presented research with RWCMG systems does not address initial CMG spin-up but makes use of CMG null motion after the rotors are already spinning at their constant nominal rate. The current research also expands the scope of the CMG null motion concept through the validation of performance in hardware experiments.

2.4   Applicable Controllers

Turning now to an examination of controllers applicable to the agile s/c mission, the traditional solution is the Proportional-Integral-Derivative (PID) controller. The PID controller calculates a control value $\vec{u}$ according to

$$\vec{u} = -(K_p \vec{q}_e + K_d \dot{\vec{q}}_e + K_i \int \vec{q}_e \, \mathrm{d}t) \tag{2.31}$$

where $\vec{q}_e$ is the quaternion error, and K_p, K_d, and K_i are the PID gains which affect parameters such as rise time, percent overshoot, and settling time of the response.

29

Quaternion error is defined in terms of the commanded attitude versus the controlled attitude as

$$\vec{q}_e = \begin{bmatrix} q_{c_4} & q_{c_3} & -q_{c_2} & -q_{c_1} \\ -q_{c_3} & q_{c_4} & q_{c_1} & -q_{c_2} \\ q_{c_2} & -q_{c_1} & q_{c_4} & -q_{c_3} \\ q_{c_1} & q_{c_2} & q_{c_3} & q_{c_4} \end{bmatrix} \vec{q}_{measured}. \tag{2.32}$$

Wie [27] provided a method of calculating the three PID gains by specifying desired natural frequency ω_n and damping ratio ζ and is shown in

$$\begin{aligned} K_p &= I_{\hat{b}}(\omega_n^2 + \tfrac{2\zeta\omega_n}{T}) \\ K_i &= I_{\hat{b}}\tfrac{\omega_n^2}{T} \\ K_d &= I_{\hat{b}}(2\zeta\omega_n + \tfrac{1}{T}) \end{aligned} \tag{2.33}$$

where $T = 10/(\zeta\omega_n)$. Expressing controller gains in damping ratio and natural frequency facilitates comparison of the PID to other controllers shown below, which also have gains transformed into the same parameters.

Going a step beyond the linear PID controller, Wie [27] derived saturated quaternion feedback (QF) control as shown in

$$\vec{u} = \text{sat}[K\text{sat}(P\vec{q}_e) + C\vec{\omega}] \tag{2.34}$$

where K, P, and C are gains which can again be defined based on desired natural frequency ω_n and damping ratio ζ of the response. Wie provided the following method of transforming ω_n and ζ into the gains K, P, and C for the quaternion feedback controller:

$$\begin{array}{lll} C = 2\zeta\omega_n I_{\hat{b}} & c = \text{mean}(\text{diag}(\tfrac{C}{I})) & KP = 2\omega_n^2 I \\ k = \text{mean}(\text{diag}(\tfrac{KP}{I})) & k_i = c\tfrac{|q_i(0)|}{\|\vec{q}(0)\|}\omega_{max} & K = \text{diag}(k_1, k_2, k_3)I \\ P = k\tfrac{K}{I} & & \end{array} \tag{2.35}$$

Wie recommended quaternion feedback control for large angle minimum-time eigenaxis maneuvers. Adding slew rate constraints to Eq. (2.34) resulted in the cascade saturation

control logic of Eq. (2.24). In both versions of the Wie quaternion feedback and PID control, the gyroscopic term of Euler's Equation $\vec{\omega} \times I\vec{\omega}$ is neglected as being insignificant. The Wie quaternion feedback controller of Equation 2.34 is implemented in the RWCMG system and is discussed further in Chapter III.

In addition to deriving equations of motion for RWCMG arrays, Schaub [8] developed a nonlinear Lyapunov rate-based equation to calculate a desired s/c torque $\dot{\vec{h}}_{act}$ directly. In other words, the Schaub controller generates $\dot{\vec{h}}_{act}$ instead of $\vec{u}$. Recall from Section 2.1 that $\dot{\vec{h}}_{act}$ is calculated from the traditional controller output, $\vec{u}$ (PID and Quaternion Feedback) via the relation

$$\dot{\vec{h}}_{act} = \vec{u} - \vec{\omega} \times \vec{h}_{act}. \tag{2.36}$$

The Schaub nonlinear Lyapunov-Based (LB) controller, with syntax transformed to match that of this document is

$$
\begin{aligned}
\dot{\vec{h}}_{act} &= Kq_e - P\delta\vec{\omega} - \vec{\omega} \times \vec{h}_{act} - I(\dot{\vec{\omega}}_r - \vec{\omega} \times \vec{\omega}_r) + \\
&\sum_{i=1}^{N} C_r(\dot{\vec{\psi}}_i\vec{\omega}_2 R_{i_1}^{bg} - \dot{\vec{\psi}}_i(c\delta_i\vec{\omega}_1 - s\delta_i\vec{\omega}_3)R_{i_2}^{bg})
\end{aligned}
\tag{2.37}
$$

where K and P are gains, $\vec{\omega}_r$ is a desired angular velocity trajectory, $\delta\vec{\omega}$ is $\vec{\omega} - \vec{\omega}_r$, and the numerical subscripts on the rotation matrices specifies the columns. Schaub derived a method to calculate the gains K and P based on natural frequency and damping ratio for a similar controller as shown in

$$
\begin{aligned}
\omega_n &= \tfrac{1}{2I}\sqrt{KI_{\hat{b}} - 2P^2} \\
\zeta &= \tfrac{P}{\sqrt{KI - 2P^2}}.
\end{aligned}
\tag{2.38}
$$

Solving Eq. (2.38) for K and P in terms of ω_n and ζ is easily accomplished through algebraic manipulations. The nonlinear controller of Eq. (2.37) is directly applicable to the agile s/c mission due to inclusion of gyroscopic terms in the $\vec{\omega}_r$ term for tracking a dynamic angular velocity trajectory.

The PID, QF, and LB controllers are tested with the RWCMG system in the presented dissertation effort. A closed-loop control scheme is developed for analytical simulation

31

using the three controllers and adapted for use on hardware on the AFIT SimSat simulator in Chapter III. Comparisons of metrics such as mission completion time, pointing error, and singularity avoidance are made between the controllers using both simulation and hardware experiments and are discussed in Chapter IV.

2.5 Singularity Avoidance

With a set of potential controllers identified, the discussion of relevant areas now shifts to singularity avoidance. As mentioned in Section 1.2, arrays of CMGs suffer singularities which need to be treated with the control algorithm. Singularities occur numerically as a result of solving Eq. (2.14) for the reaction wheel accelerations and gimbal rates in $\dot{Y}$. A singularity avoidance scheme will be part of the presented research, but as discussed below, adding null space degrees of freedom by combining CMGs with reaction wheels provides a strong singularity avoidance mechanism in and of itself. Before developing the RWCMG approach, a short discussion on other singularity avoidance techniques assists with explaining the technical challenges and limitations of building control arrays. The method of calculating the inverse of the non-square $A(\dot{\psi}, \delta)$ matrix is the subject of numerous singularity avoidance techniques [9; 36–40]. Wie [27] developed a generalized SR inverse for traditional SGCMGs shown in

$$
\begin{aligned}
\dot{\vec{\delta}} &= A^T (AA^T + \lambda E)^{-1} \dot{\vec{H}}_{act} \\
E &= \begin{bmatrix} 1 & \epsilon_3 & \epsilon_2 \\ \epsilon_3 & 1 & \epsilon_1 \\ \epsilon_2 & \epsilon_1 & 1 \end{bmatrix} \\
\epsilon_i &= \epsilon_0 \sin(\omega t + \phi_i).
\end{aligned}
\tag{2.39}
$$

Wie noted that this method of solving the torque equation did not prevent singularities outright. Rather the method approached singularities and then quickly escaped them by varying the ϵ_i parameters via the trigonometric function. Of further note with the Wie SR method, was that it did not necessarily provide strong pointing accuracy during the

reorientation maneuver. Error rates were near zero after each maneuver completed, but the author did not provide detail on tracking performance during the maneuver.

The generalized SR inverse used in [27] is one of several singularity avoidance techniques shown in the comprehensive survey done by Kurukowa [30]. Kurukowa specified four main types of singularity avoidance steering laws for CMG pyramids: exact solution, off-line planning, steering law allowing torque error, and VSCMG arrays. Exact solutions in [30] included the traditional Moore-Penrose inverse as shown in Eq. (2.18), gradient methods, and preferred angle setting. The basic Moore-Penrose inverse contains no mechanism to escape a singularity once reached. Gradient methods, which attempt to avoid singularities through manipulation of an objective function, fell short for pyramid CMG arrays according to Kurukowa because they do not have a means of traversing internal singularities if one was encountered. Preferred angle setting, the third exact solution in [30], fell short in that it relied on using one-dimensional null motion to set initial gimbal angles to pre-calculated angles. A pyramid array of four SGCMGs contains only one degree of freedom for null motion to take place thus the ability to achieve desired initial gimbal angles without imparting unwanted torque on the s/c is very limited.

The second main type of singularity avoidance technique in [30] was off-line planning. Off-line optimization of control inputs using the CMG array equations of motion avoids all singularities by steering the CMGs on paths that avoid singularities. These optimal controls can then be fed open loop to execute the attitude maneuver, however the method is overly expensive computationally and very susceptible to disturbance torques.

Steering laws which allow torque error were the third main type of singularity avoidance technique in [30]. These methods encompass several variations of the SR inverse of [27]. All internal singularities can be avoided with this method but at the cost of increased error in $\vec{h}_{act}$. Kurukowa concluded that the degree of error imparted by the various

SR techniques were most dependent on the singular surface geometry. In other words, there is not a single best SR method for all mission sets.

Finally, Kurukowa examined VSCMG array methods for avoiding singularities. All of the above singularity avoidance techniques have no means of avoiding a saturation singularity. VSCMG systems are no different in that respect. If the CMG rotors for a VSCMG array are spinning at their maximum rate, a commanded torque requesting a further increase will cause a saturation singularity regardless of the algorithm used. Saturation for CMGs is based on gimbal angles. Once the gimbal angles are lined up for momentum exchange in one direction no further momentum can be exchanged between the s/c and the CMG array. But according to [30], saturation is the extent of the singularity limitations on VSCMG systems. However, reaction wheel torque is relatively small when compared to that of CMGs and thus Kurukowa recognized a supplemental means of singularity avoidance such as those mentioned above is still advisable when using a VSCMG array. Ultimately, Kurukowa concluded that no best singularity avoidance technique exists. The technique chosen must be based on mission needs and system architecture.

The research with combined CMG and reaction wheel arrays in this dissertation is inherently singularity robust. Reaction wheels take the place of CMG rotors with varying spin rates to avoid non-saturation singularities. A simple SR inverse based on work in [27] is investigated and discussed Section 3.2.3. The singularity measure v introduced in Section 2.3 is used in the RWCMG research as a metric for assessing mathematical singularity closeness - a singularity occurs when the parameter is zero. A second singularity measure, ς, indicates closeness to a condition in which the required control torque is in the null space of the A matrix and is shown in Eq. (2.40) [8].

$$\varsigma = \frac{1}{\vec{h}_0^2} \frac{\dot{\vec{h}}_{\text{act}}^T A A^T \dot{\vec{h}}_{\text{act}}}{\left\| \dot{\vec{h}}_{\text{act}}^2 \right\|} \tag{2.40}$$

The ν singularity measure of Eq. (2.29) shows closeness to a mathematical singularity, while this ς singularity measure represents closeness to a physical singularity in which the required torque is perpendicular to the span of the g_{i1} axis of the CMG gimbals and is commonly referred to as gimbal lock [8]. Both singularity measures will appear as a plot in Chapter IV, however the ν singularity measure will be the chief singularity metric since ς cannot be near-zero without ν being near-zero first.

2.6   Null Motion

Coupled tightly with singularity avoidance is the area of null motion. Although already introduced, null motion will now be further explained with application to the RWCMG mission. Singularities and null motion of CMG arrays have been studied in the literature as hindrances to successful implementation [9; 37–46]. Null motion applied to the s/c control problem refers to the condition of having more than three actuators in a non-orthogonal configuration, allowing the ability to manipulate gimbal angles along trajectories which impart no theoretical resultant torque on the s/c. The dimension of the null space for CMGs depends on how many extra degrees of freedom (non-orthogonal actuators) beyond three exist on the spacecraft. Typical four-SGCMG pyramids have a null space of dimension one. The focus of this research is to use a pyramid array of four CMGs and an array of three orthogonal reaction wheels, creating a potential null space of four dimensions with which to manipulate CMG gimbal angles to preferred values for singularity avoidance, pointing error reduction, and slew speed optimization.

Schaub [8] developed equations for VSCMG array null motion which are directly related to the case of combined CMGs and reaction wheels. Recall from Section 1.2 that equations treating VSCMG arrays are easily transformed to treat the RWCMG case. Schaub gives the following Lyapunov-based equation for null motion of an NxN VSCMG

35

array

$$\begin{bmatrix} \ddot{\vec{\psi}} \\ \dot{\vec{\delta}} \end{bmatrix} = \dot{\vec{Y}} = k(WA^T(AWA^T)^{-1}A - I_{NxN})T(\Delta Y) \tag{2.41}$$

where k is a positive gain, W is the weighting matrix introduced in Section 2.3, I is an NxN identity matrix, T is a $2Nx2N$ matrix of ones or zeros for preferred value application, and ΔY is the difference between the current states and the preferred states. Rotor accelerations and gimbal rates falling on the trajectory of Eq. (2.41) will theoretically cause no torque to the s/c because they exist in the null space of the weighted pseudo-inverse of Eq. (2.28). However, for a vector to exist in any null space and produce the result that $A\vec{x}$ is $\vec{0}$, the values of $\vec{x}$ must be precise. Due to the requirement to use a pseudo-inverse for RWCMG torque equations and measurement error inherent in any hardware system, the notion of perfectly precise gimbal null motion is impractical. Therefore, steps to characterize and minimize disturbance torque generated from CMG null motion are necessary.

2.7   Stochastic Estimation

When implementing a control solution, especially one which attempts to use null motion, state measurement is of paramount importance because noise signals are present in both dynamics and measurements that can significantly impact accuracy if not treated properly.   The standard linear Kalman filter is the traditional method of filtering measurements and tracking states in stochastic systems [47; 48]. Stochastic estimation begins with stochastic modeling. Where a deterministic system typically attempts to solve the system $\dot{\vec{x}} = A\vec{x} + B\vec{u}$ and $\vec{y} = C\vec{x} + D\vec{u}$, stochastic systems must add terms to insert expressions of the anticipated noise. The standard stochastic model is

$$\begin{aligned} \dot{\vec{x}} &= A\vec{x} + B\vec{u} + G\vec{w} \\ \vec{y} &= C\vec{x} + \vec{v} \end{aligned} \tag{2.42}$$

where G is the noise allocation matrix, $\vec{w}$ is the dynamics noise vector (normally zero-mean white Gaussian), and $\vec{v}$ is the measurement noise vector. The standard Kalman filter tracks

36

the state $\vec{x}$ and a covariance matrix P through a cycle of time propagation and update via measurement. The basic process is shown in Figure 2.2. The matrix Φ in Figure 2.2 is

Truth Model

$$\vec{x}_k = \Phi_{k-1}\vec{x}_{k-1} + B_{k-1}\vec{u}_{k-1} + w_{k-1}$$

$$\vec{y}_k = C_k\vec{x}_k + \vec{v}_k$$

State and Covariance Propagation

$$\vec{x}_k^- = \Phi_{k-1}\vec{x}_{k-1}^+ + B_{k-1}\vec{u}_{k-1}$$

$$P_k^- = \Phi_{k-1}\vec{x}_{k-1}^+\Phi_{k-1}^T + Q_{k-1}$$

State and Covariance Meas. Update

$$K_{k_{opt}} = P_k^-[C_kP_k^-C_k^T + R_k]^{-1}$$

$$\hat{\vec{x}}_k^+ = \hat{\vec{x}}_k^- + K_k(y_k - C_k\hat{\vec{x}}_k^-)$$

$$P_k^+ = (I - K_kC_k)P_k^-$$

Increment Time Counter
$$k = k + 1$$
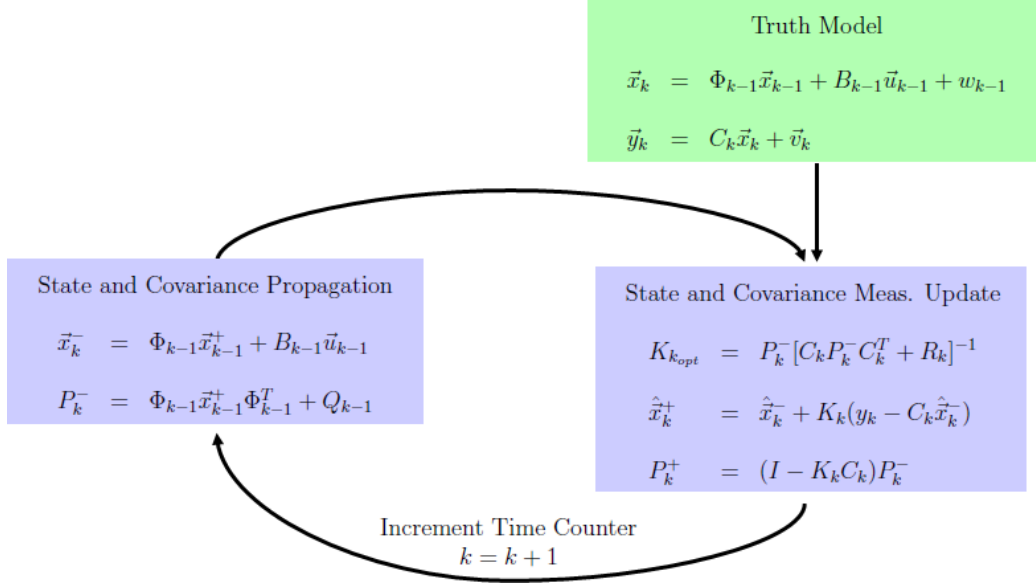
Figure 2.2: Standard Kalman Filter Algorithm

the state transition matrix, Q_d is a discretized dynamics noise allocation matrix defined as $E\left[\vec{w}_k\vec{w}_k^T\right]$, and K is the Kalman gain. While the standard Kalman filter provides stochastic estimation of states, it assumes Gaussian noise states and a linear model, resulting in a linear recursion. For the highly nonlinear problem of satellite control, one can obtain better accuracy by using a nonlinear filtering method.

The extended Kalman filter (EKF) is the most basic expansion of the standard Kalman filter. While the EKF still assumes Gaussian noise and linear models, the dynamics matrix A, and consequently the state transition matrix Φ, are now estimated using first-order Taylor Series expansions at each time step, before the propagation. The matrix Q_d is discretized and recalculated at each time step as well with the EKF. The EKF dynamics model is shown in Eq. (2.43), EKF propagation algorithm is shown in Eq. (2.44), and the EKF update algorithm is shown in Eq. (2.45).

Extended Kalman Filter Stochastic Model

$$\dot{\vec{x}}(t) \;=\; a(\vec{x}(t), \vec{u}(t), t) + G(t)\vec{w}(t)$$

$$y(t_i) \;=\; c(\vec{x}(t_i), t_i) + v(t_i) \tag{2.43}$$

Extended Kalman Filter Propagation

$$\dot{\vec{x}}(t/t_i) \;=\; a(\vec{x}_n(t/t_i), \vec{u}(t))$$

$$P_{i+1}^- \;=\; \Phi_i P_i^+ \Phi_i^T + Q_d \tag{2.44}$$

Extended Kalman Filter Update

$$\hat{\vec{x}}_{i+1}^+ \;=\; \hat{\vec{x}}_{i+1}^- + K_{i+1}(y(t_{i+1}) - c(\hat{\vec{x}}_{i+1}^-, t_{i+1}))$$

$$P_{i+1}^+ \;=\; (I - K_{i+1}C_{i+1})P_{i+1}^- \tag{2.45}$$

$$K_{i+1} \;=\; P_{i+1}^- C_{i+1}^T (R_{i+1} + C_{i+1}P_{i+1}^- C_{i+1}^T)^{-1}$$

Following the EKF, an improved filtering method which models up to second order nonlinearities is the unscented Kalman filter (UKF). As in the EKF, the UKF assumes Gaussian noise and states and uses a linear recursion, but deviates from the EKF in that it treats nonlinear dynamic and measurement noise as well. First developed in [49–51], the UKF process starts with selecting $2n+1$ sigma points χ_i, where n is the number of states via the equations

$$
\begin{aligned}
\chi_0 &= \bar{\mathbf{x}} & W_0^m &= \tfrac{\lambda}{L+\lambda} & W_0^c &= \tfrac{\lambda}{L+\lambda} + (1 - \alpha^2 + \beta) \\
\chi_i &= \bar{\mathbf{x}} + (\sqrt{(L+\lambda)\mathbf{P}_{xx}})_i & W_i^m = W_i^c &= \tfrac{1}{2(L+\lambda)} \\
\chi_{i+n} &= \bar{\mathbf{x}} - (\sqrt{(L+\lambda)\mathbf{P}_{xx}})_i
\end{aligned}
\tag{2.46}
$$

where the superscript m represents the mean weighting factor, c represents the covariance weighting factor, W_i are weighting factors for each point, L is the number of filtered states, and λ, α, and β are tuning parameters [52]. These sigma points are evaluated in the nonlinear function

$$Y_i = a(\chi_i) \tag{2.47}$$

where a is a function of $\vec{x}(t)$, $\vec{u}(t)$, and t to find a transformed set, Y_i. The mean and covariance of the transformed set are then

$$\bar{\mathbf{y}} = \sum_{i=0}^{2n} W_i \mathbf{Y}_i \tag{2.48}$$

$$\mathbf{P}_{yy} = \sum_{i=0}^{2n} W_i (\mathbf{Y}_i - \bar{\mathbf{y}})(\mathbf{Y}_i - \bar{\mathbf{y}})^T. \tag{2.49}$$

According to [52] this technique results in a mean which is more accurate than the EKF and a comparably accurate covariance. The implementation algorithm for the UKF is summarized:

- UKF Propagate:

  1. Calculate sigma points:

     $$\chi_0 = \hat{x}_{k-1}$$

     $$\chi_i = \hat{x}_{k-1}^+ \pm \sqrt[chol]{(\lambda + L)\, P_{x_{k-1}}^+}\Big|_i, \forall i \tag{2.50}$$

     $$\lambda = \alpha^2(L + K) - L, \quad \alpha = 3 - \lambda \quad L = \text{length}(x) \quad K = 0$$

  2. Calculate weighting factors:

     $$W_0^m = \frac{\lambda}{(L+\lambda)}$$

     $$W_0^c = \frac{\lambda}{(L+\lambda)} + (1 - \alpha^2 + \beta), \quad \beta = 1 \tag{2.51}$$

     $$W_i^c = W_i^m = \frac{1}{2(L+\lambda)}, \forall i = 1, \cdots, 2L$$

  3. Calculate propagated states and covariance:

     $$\hat{x}_k^- = \sum_{i=0}^{2L} W_i^m \chi_i^-$$

     $$\tag{2.52}$$

     $$P_{xx}^- = \sum_{i=0}^{2L} W_i^c (\chi_i^- - \hat{x}_k^-)(\chi_i^- - \hat{x}_k^-)^T + Q_{k-1}$$

- UKF Update:

$$Z_i^- = c(\chi_i^-), \forall i = 0, 1, \cdots, 2L$$

$$\hat{z}_k^- = \sum_{i=0}^{2L} W_i^m Z_i^-$$

$$P_{zz_k} = \sum_{i=0}^{2L} W_i^m (Z_i^- - \hat{z}_k^-)(Z_i^- - \hat{z}_k^-)^T + R_k$$

$$P_{xz_k} = \sum_{i=0}^{2L} W_i^m (\chi_i^- - \hat{z}_k^-)(\chi_i^- - \hat{z}_k^-)^T \tag{2.53}$$

$$K_k = P_{xz_k} P_{zz_k}^{-1}$$

$$\hat{x}_k^+ = \hat{x}_k^- + K_k(z_k - \hat{z}_k^-)$$

$$P_{x_k}^+ = P_{x_k}^- - K_k P_{zz_k} K_k^T$$

Examining some representative cases of filtering used in satellite attitude control, Vitalich [53] used a standard Kalman filter to generate attitude control measurements for the Naval Postgraduate School (NPS) simulator NPSAT-1. The standard filter was used as a six-state rate estimator for satellite roll, pitch, and yaw, and angular rates based on a single star sensor measurement. Results plots were shown and the authors concluded that the standard Kalman filter was adequate as a backup to rate gyro trackers. Specific metrics on accuracy were not stated. Chagas [31] used an EKF, UKF, and particle filter (PF) for attitude measurements on a regulator s/c hardware simulator. Two magnetometers and two accelerometers comprised the sensors for a hardware test of the three filters. Deterministic disturbance torques were applied half-way through the experiment to characterize each filter's performance to such an event. Following the tests, Chagas recommended use of the EKF for steady-state and UKF during any unexpected situations. The PF was too numerically cumbersome at the time of the experiment - 2010.

The EKF and UKF are implemented in the presented RWCMG analytical closed-loop control scheme. Measurement and dynamics noise are added to the analytical simulation to represent measurement uncertainty and disturbance torques. Mean error, standard deviation, and root sum square statistics are calculated for each filter based on Monte Carlo runs in which the noise vectors are randomly generated in a normal distribution. Comparisons of the performance of the two filtering methods are made based on these statistics. The existing low-pass filter implemented by McChesney for the AFIT SimSat platform allows the onboard inertial measurement unit to produce adequate measurement accuracy for hardware simulation [32]. No further filtering techniques are applied to the hardware simulation due to a lack of dynamic external measurement sources at the current time. Planned improvements in SimSat measurement devices will allow filtering to be addressed in hardware simulation in the near-future and is a topic recommended in Section 5.3.

2.8 Preferred Gimbal Angles

The next relevant area for improving agile s/c performance is preferred gimbal angles. As discussed in Section 2.5, setting gimbal angles to desired values prior to a maneuver is one method of avoiding singularities in CMGs. The concept of preferred gimbal angles also came into relevance in Section 2.6 as using null motion was a way in which to achieve the desired gimbal angles without imparting torque on the s/c. One often cited reference on the calculation of preferred gimbal angles is Vadali [2]. Vadali developed a method to calculate preferred gimbal angles through a backward integration of Eq. (2.18) with constant-speed CMGs. For various secular s/c torques (torque in one body axis direction only), Vadali started the backward integration at actuator saturation. In other words for a desired torque in the s/c x-direction, the gimbal angles were set so each had the momentum vector, $\vec{h_i}$ projected in the x-direction. But since these saturation gimbal angles caused an external singularity, Vadali arbitrarily perturbed those angles slightly. The backward integration was

run until the s/c angular momentum vector was near zero to find the preferred initial gimbal angles. Of note during this process was that internal singularities did not occur during the entire backward integration. Further, the initial gimbal angles of $[45°, -45°, 45°, -45°]$ were found to avoid internal singularities for all desired torque cases examined in [2] except for a secular z-axis torque (pure yaw). The technique developed by Vadali was performed off-line before the control simulation began and was not optimal. Preferred gimbal angles found in [2] are shown in Figure 2.3.

Table 1   Initial gimbal angles for null momentum

Torque demand	Initial gimbal angles		
[1 0 0]	[− 60 deg 60 deg 120 deg −120 deg]	[45 deg −45 deg 45 deg −45 deg]
[0 1 0]	[−120 deg −60 deg 60 deg 120 deg]	[45 deg −45 deg 45 deg −45 deg]
[0 0 1]	[0 deg 0 deg 0 deg 0 deg]	
[1 1 1]	[0 deg 0 deg 0 deg 0 deg]	[45 deg −45 deg 45 deg −45 deg]
[4 2 0]	[− 60 deg 60 deg 120 deg −120 deg]	[45 deg −45 deg 45 deg −45 deg]
[2 4 0]	[−120 deg −60 deg 60 deg 120 deg]	[45 deg −45 deg 45 deg −45 deg]

Figure 2.3: Preferred Gimbal Angles for Various Secular Torque Demands (Vadali [2])

As discussed in Section 2.2 Nanamori [22] took the work of Vadali further in developing an optimization method of calculating preferred initial gimbal angles. Still the optimization in [22] was done off-line before the simulation started. In addition, the preferred gimbal angles from Nanamori were only calculated once for a whole set of target attitudes. No optimization or gimbal conditioning was done between targets once the simulation started.

The research conducted for this dissertation seeks to use null motion to place gimbal angles in near-optimal positions during target dwell phases of a representative multiple target collection mission. Preferred gimbal angles are calculated with three methods for the analytical simulation: offline pseudo-spectral optimization, near real-time sequential quadratic programming embedded within the closed-loop control scheme, and table look-up of the Vadali universal set of ±45° alternating. Methods for the first two preferred

gimbal angle calculations are found in Section 3.2.8. The first and third preferred gimbal angle calculation techniques: offline pseudo-spectral optimization and Vadali look-up, are used in hardware experiments. Results of null motion simulations and experiments seeking these preferred values are found in Section 4.3.

2.9   Applied Optimization

Beside the optimization of initial gimbal angles discussed in the previous section, the overall problem of steering an agile s/c to multiple targets in the shortest time possible is an optimization problem unto itself. Like the preferred initial gimbal angle optimization, work in the s/c steering optimization field has been done off-line. Optimal gimbal angles to perform an entire maneuver can be calculated using a number of classical numeric methods including finite difference, sequential quadratic programming, and constrained steepest descent [54; 55]. More recently pseudo-spectral (PS) [56] methods have been investigated in performing the optimization. The optimized steering values for the PS controller are used in an open-loop feed-forward manner as shown in Figure 2.4. When steering solutions are fed forward the system is more susceptible to disturbance torques than a closed-loop system. Wright [28] developed a method for comparing a PID controller with a PS controller by tuning PID gains for a specific maneuver. He concluded that even with specifically derived PID gains, the PS solution performed better than the linear PID controller for large angle maneuvers.
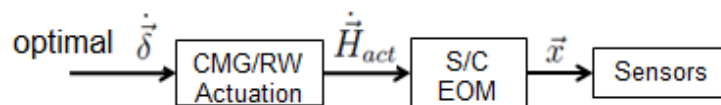
Figure 2.4: Open-loop Implementation of Optimized Gimbal Angles

Karpenko [3] developed a method to use optimized gimbal angles in a closed-loop controller as shown in Figure 2.5. Karpenko's method was to develop a revised CMG

43
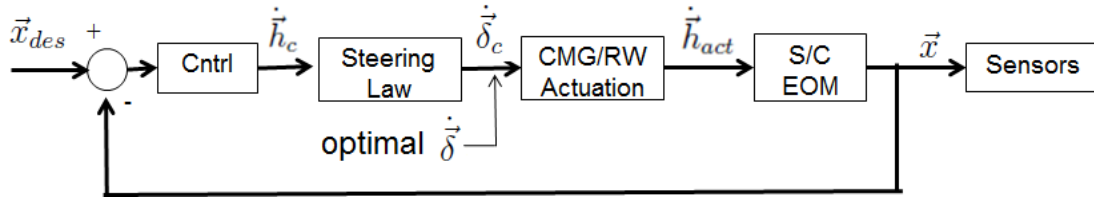
Figure 2.5: Use of Optimal Gimbal Angles in Closed Loop Control [3]

steering law which kept the closed-loop controller from forcing a large deviation from the optimal gimbal angles. This method then avoided singularities through the optimization and reduced disturbance torque error through the closed-loop corrections.

PS optimization is used in this dissertation research as a means to create a benchmark for measuring controller performance and null motion implementation. Discussed further in Chapter III, optimization of multiple target collection is a minimum target pointing error problem. Results of the PS optimizations for the overall mission give a sense of what is possible when all hardware limitations are obeyed in a closed-loop algorithm. If a closed-loop numerical simulation results in completing the multiple target collection mission in less time than the optimized solution, an error in enforcing hardware limits is known to have occurred. The setup of the benchmark pseudo-spectral optimization technique is discussed in Section 3.1.3. The same optimization technique used for creating the benchmark is recycled for calculation of preferred gimbal angles by lifting constraints on the initial gimbal angles for each slew maneuver. Sequential quadratic programming optimization is used for preferred gimbal angle calculation. Further discussion of preferred gimbal angle techniques is found in Section 3.2.8.

2.10 SimSat Spacecraft Experiment Platform

AFIT possesses a satellite simulator called SimSat. The SimSat hardware was designed by students starting in 1999 and has taken many configurations in the years since. In its current configuration, SimSat contains a pyramid of four SGCMG at a beta angle

44

of 54.74°, three orthogonal reaction wheels, and three pairs of fans to simulate thrusters. An automated mass balance system was recently added by Wright but was not used in this dissertation research [57]. The current configuration is shown in Figure 2.6. Directly
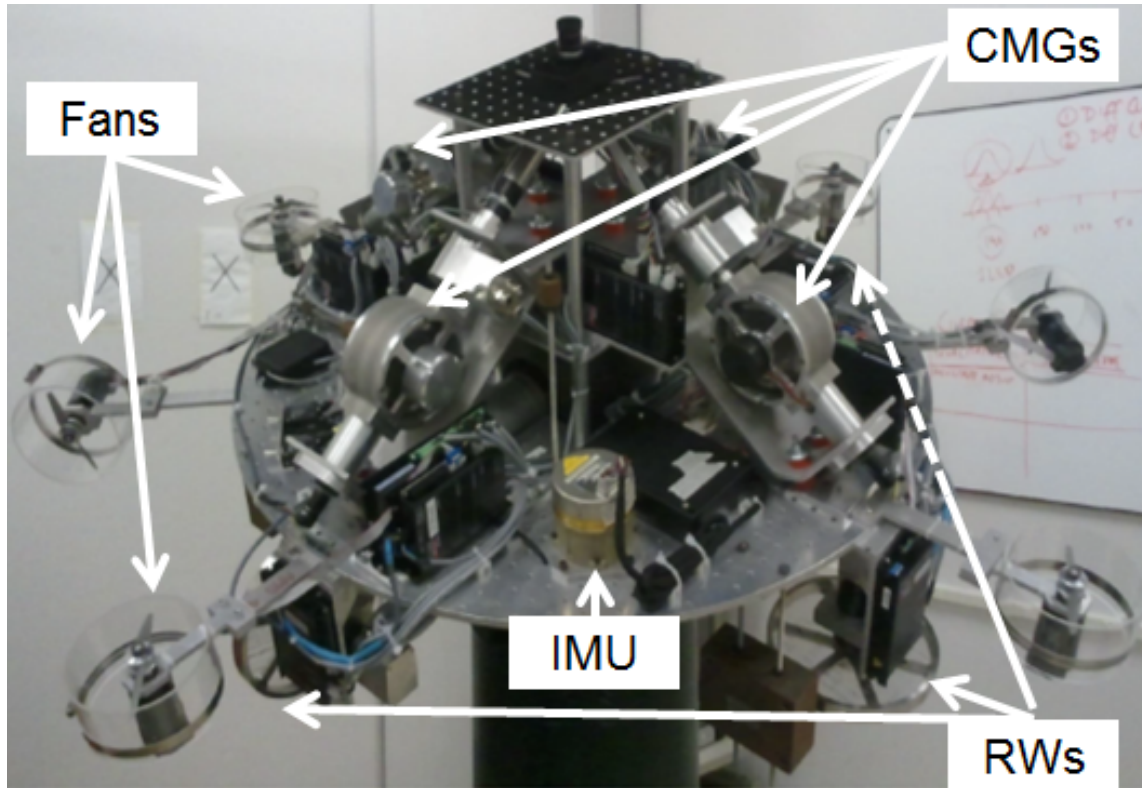
Figure 2.6: AFIT SimSat Hardware with Actuators Labeled

relevant to the scope of this dissertation, the SGCMG pyramid and reaction wheel array were designed and characterized in 2012 by McChesney [32]. The reaction wheels have a diameter of approximately 20 cm and have a nominal torque output of 0.3 N-m. Maximum spin rate of the reaction wheels is approximately 2650 RPM. The SGCMG array consists of 360° unrestricted gimbals and rotors which spin at a constant 2600 rpm for an array maximum torque capability of 0.5 N-m.

The SimSat platform rests atop a Space Electronics SE-9791 air bearing which allows a range of attitude of approximately ±25° about the horizontal axes and unlimited rotation

about the vertical axis. Recent work by Wright with the current configuration of SimSat validated moment of inertia calculation algorithms for the hardware [57]. The moment of inertia Wright calculated is assumed in this dissertation effort. An LN-200 IMU provides s/c rate measurement. A dSPACE MicroAuto Box provides real-time processing and handles command and data handling, while a mini PC is also attached to the platform for communications between the MicroAuto Box and the ground station computer [58]. SimSat users design experiments in the MATLAB® Simulink environment and use an interface card within the mini PC to build the Simulink model into C-code and load the model into the MicroAutoBox.

No hardware modifications have been made to SimSat during this dissertation research. The platform is used in its current configuration to run experiments testing combined SGCMG and reaction wheel actuation. A new Simulink model was developed for SimSat which echoes the analytical scripts used to perform the research. The analytical model and SimSat Simulink experimental version are discussed further in Section 3.3.

With the equations of motion and research areas applicable to the RWCMG system explained, attention now turns to the methods used to conduct the dissertation research. SimSat simulator properties are used as the representative s/c and are explained in Chapter III. A representative agile s/c mission is also explained. Closed-loop control schemes for the RWCMG system in analytical simulation and hardware experiments are developed. Means of assessing RWCMG system performance are also introduced.

III.   Methodology

Application of concepts discussed in the previous chapter to the RWCMG system research begins with generating a representative agile imaging spacecraft and target set. The representative s/c analyzed contains a pyramid of four SGCMG actuators and three reaction wheels. The topic of optimization is explored with the purpose of generating benchmarks with which to compare the more likely to be implemented closed-loop control solutions. Development of the optimization cost function is also discussed here. Next, the topic of controller implementation is discussed with respect to the various types of controllers evaluated: PID, quaternion feedback (QF), and nonlinear Lyapunov-based (LB) methods. Each of these controllers is evaluated in both numerical simulations as well as hardware experiments. Implementation of limits in the numerical control algorithm follows. A procedure for imposing limits such as maximum reaction wheel rotation rate and maximum s/c angular rate is generated. Due to the nonlinear equations of motion and requirement for pseudo-inverses, imposing limits on a RWCMG system in simulations is non-trivial. Application of the limiting procedure is made to each of the three controllers mentioned above. Procedures used to generate preferred gimbal angles are detailed next. The three methods investigated are off-line calculation using PS optimization, near real-time calculation using a sequential quadratic programming method, and Vadali preferred angle lookup [2]. Next, the method used to implement null motion trajectories of gimbal angles in simulation and experimentation is presented. Application of the EKF and UKF to the simulated agile spacecraft mission is then detailed. Finally, consideration is given to the task of applying analytical codes to the SimSat hardware for experimentation.

3.1 The Agile Spacecraft Mission Defined

In order to test the performance of a RWCMG control system for an agile spacecraft, a representative spacecraft and mission must be defined. The following sections describe the parameters of the representative spacecraft and target set devised for the mission. Also discussed are efforts to contain analytical results through study of optimized solutions.

3.1.1 Simulated Spacecraft Parameters.

Properties of the representative agile imaging spacecraft used in this research, modeled after the AFIT SimSat presented in Section 2.10, are shown in Figure 3.1.

Spacecraft Inertia $(kgm^2)^\natural$:

$$\begin{bmatrix} 6.454 & -0.197 & -0.175 \\ -0.197 & 9.716 & -0.142 \\ -0.175 & -0.142 & 12.848 \end{bmatrix}$$

Single CMG Rotor Inertia $(kgm^2)^\natural$:

$$\begin{bmatrix} 9.5E^{-4} & 0 & 0 \\ 0 & 9.5E^{-4} & 0 \\ 0 & 0 & 1.6E^{-3} \end{bmatrix}$$

Spacecraft Initial State:

Quaternions $(\bar{q})$	$[0;0;0;1]^T$
Angular Rate $(\bar{\omega})$	$[0;0;0]^T$ rad/s
RW Rate $(\dot{\Psi}_{RW})$	0 rpm* each
RW Accel $(\ddot{\Psi}_{RW})$	0 rad/s^2 each
Rotor Rate $(\dot{\Psi}_{CMG})$	2600 rpm* each
Rotor Accel $(\ddot{\Psi}_{CMG})$	0 rad/s^2 each
Gimbal Angles $(\bar{\delta})$	varies by experiment
Gimbal Rates $(\dot{\bar{\delta}})$	0 rad/s each

ACS Limitations $(\pm)$:

Max Torque	0.25 Nm
Max Angular Rate	8 deg/s*
Max RW Rate	2650 rpm*
Max RW Accel	10 rad/s^2
Max Gimbal Accel	4.75 rad/s^2
Max Gimbal Angles	unlimited
Max Gimbal Rate	2.5 rad/s

Orbit Parameters/Spacecraft Limits :

Altitude	770 km*
Ground Vel.	6.663 km/s
Max Off-Nadir $\angle$	45 deg*

ACS Geometry

Configuration	4 VSCMG Pymd
CMG Beta Angle	54.74 deg*

$\natural$ From Wright, 2015

* Converted to SI units

Figure 3.1: Simulated Agile Spacecraft Properties

The Max Torque value of 0.25 Nm in Figure 3.1 is a self-imposed maximum torque which the SimSat actuators can impart on the platform without risking a collision of the platform with the air bearing pedestal. A top-down and side view of the geometry of SimSat is shown in Figure 3.2 with gimbal axes shown for CMG 1. Application of the process detailed in Section 2.1 is used to find the rotation matrices R_i^{bg} for this configuration.
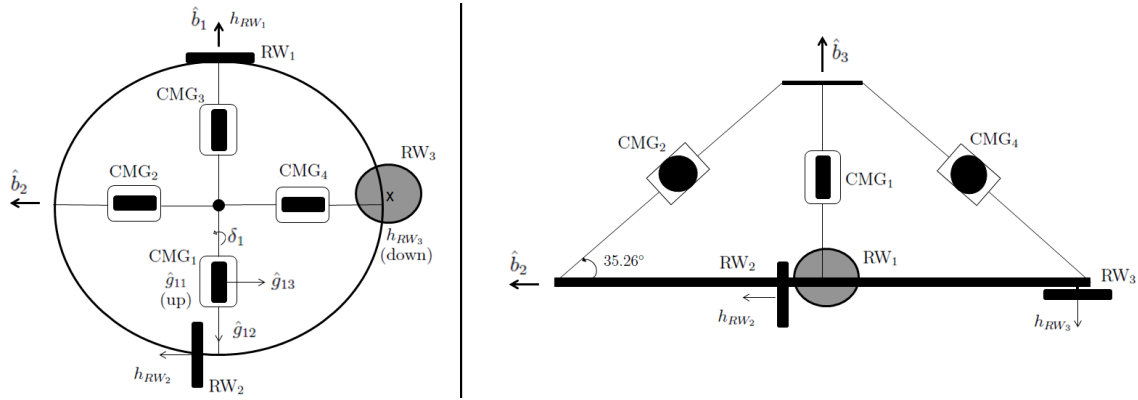
Figure 3.2: Simulated CMG Pyramid Geometry with RWA Layout, Top-View (left), Side-View (right)

Equations of motion (2.16) and (2.19) from Section 2.1 along with the SR inverse shown in Eq. (3.12) to compute $\dot{\vec{Y}}$ are coded into a MATLAB® numerical simulation.

3.1.2 Representative Mission Definition.

A representative flat target field was created for the analytical research as was illustrated in Figure 1.1. Grid locations of the targets are shown in Table 3.1. The order in which the targets are addressed is assumed to be known before the mission starts. Optimization of target order is outside the scope of this research effort. The targets are placed to require the satellite to perform large angle maneuvers between targets in order to stress the RWCMG control system to better assess its performance. With such an arrangement of geometry and targets, rotation about the spacecraft $\hat{b}_1$ axis is commanded to a constant zero degrees for the entire mission. Rotation about the $\hat{b}_2$ axis is dynamic

during slews between targets but remains constant once the proper angle has been reached to image the current target. Rotation about the $\hat{b}_3$ axis occurs at a relatively fast rate when changing targets, then slows down to a rate which compensates for the orbital velocity of the spacecraft as it flies over the target area during collection.

Table 3.1: Representative Target Locations and Required Viewing or Dwell Time

Target	s_1, s_2 Coordinate (km)	Dwell Time (sec)
1	(50,0)	20
2	(300,-250)	30
3	(740,250)	28
4	(1000,-250)	30

For the experimental analysis using SimSat hardware, some modification to the targeting system is needed. Due to the $\pm 25°$ limitation to the spacecraft $\hat{b}_1$ and $\hat{b}_2$ axes, the target field is oriented so that the dynamic axis is the $\hat{b}_3$ instead of the $\hat{b}_2$. This change allows SimSat to perform the representative mission to cover four targets without potential hardware collision. Rotation about the SimSat $\hat{b}_1$ axis is commanded at a constant zero attitude and rotations about the $\hat{b}_2$ axis perform the desired side-to-side slewing of the representative target set. The target field is adjusted so that each target is exactly $15°$ from the zero nadir angle. A constant slewing rate for the dynamic axis is given for the spacecraft axis tracking the target field s_1 direction. In order to compare analytical simulation to hardware experiments these changes are also programmed into the analytical model as an option.

3.1.3 The Optimal Solution - A Benchmark.

Before implementation of a closed-loop controller in simulation or hardware, a look at a PS optimization of a simple SCGMG system yields a benchmark with which to assess performance of the controllers. For a multi-target agile satellite which seeks to image targets for a specified dwell time in the shortest time possible, the formal definition of this problem is shown in Eq. (3.1).

$$
\begin{aligned}
\text{Minimize} \quad & J(\vec{x}, \vec{u}, t) & = \quad & t_f \\
\text{where} \quad & \vec{x} & = \quad & [\vec{q}, \vec{\omega}, \vec{\delta}, \dot{\vec{\delta}}] \\
& \vec{u} & = \quad & \ddot{\vec{\delta}} \\
\text{Subject to} \quad & \dot{\vec{x}} & = \quad & [Eq.\, 2.19,\ Eq.\, 2.16,\ \vec{x}(12-15),\ \vec{u}] \\
& \vec{x}(t_0) & = \quad & [\vec{q}(t_0), \vec{\omega}(t_0), \vec{\delta}(t_0), \dot{\vec{\delta}}(t_0)] \\
& \vec{x}(t_f) & = \quad & [\vec{q}(t_f), \vec{\omega}(t_f), \text{free}, \text{free}] \\
& \left| \dot{\vec{\delta}}(t) \right| & \leq \quad & \text{Max } \dot{\vec{\delta}} \\
& \left| \ddot{\vec{\delta}}(t) \right| & \leq \quad & \text{Max } \ddot{\vec{\delta}} \\
& \left| \vec{\omega}(t) \right| & \leq \quad & \text{Max } \vec{\omega}.
\end{aligned}
\tag{3.1}
$$

The cost function J of this optimization is the final time when collection on all targets has been achieved according to the target dwell times in Table 3.1. Initial spacecraft attitude and angular rates are assumed known fixed values for the optimization. Hardware constraints such as maximum gimbal rates and accelerations, maximum spacecraft slew rate, and maximum spacecraft slew angles must be enforced in the optimization to ensure realism of the results. However, when coding this optimization problem for a four CMG pyramid into a PS solver, it quickly becomes evident that the proposed states: quaternions $\bar{q}$, spacecraft angular rates $\bar{\omega}$, gimbal angles $\bar{\delta}$ and gimbal rates $\dot{\bar{\delta}}$ are insufficient to converge on an answer. In most PS solvers, the user must input boundary conditions for the states which the program must meet while optimizing (usually minimizing) the objective function. For the problem of a spacecraft traveling with orbital velocity over a target field, the time

required for the slew to each target is unknown to the programmer before the optimization starts. Constraints on the states keep the optimized solution within desired bounds, but do not sufficiently address pointing accuracy since the only constraint on quaternions is a maximum off-nadir pointing angle. Some other means of constraining the problem is necessary to converge on a solution. To this end, the problem definition in Eq. (3.1) can be modified by either adding a target tracking state to the equations of motion, or modifying the cost function. The simplest of these options in terms of reduced computation time is to simply add a pointing error term to the cost function. At each time step or collocation point of the optimization we can calculate the desired quaternions and compare to the current quaternions as predicted from the equations of motion. In practice, a conversion from quaternions to Euler angles at each time step allows the error term to be found as shown in

$$
\begin{aligned}
\epsilon_1(k) &= |\theta_{1c} - \theta_{1m}| \\
\epsilon_2(k) &= |\theta_{2c} - \theta_{2m}| \\
\epsilon_3(k) &= |\theta_{3c} - \theta_{3m}| \\
\epsilon_i &= \sum_{k=1}^{N_{ts}} \|[\epsilon_1(k)\; \epsilon_2(k)\; \epsilon_3(k)]\|_2
\end{aligned}
\tag{3.2}
$$

where $\epsilon_i(k)$ are the error of each Euler angle at collocation point k, θ_{ic} are the commanded Euler angles at collocation point k, θ_{im} are the measured Euler angles from the optimization calculation of the equations of motion, N_{ts} is the number of time steps or collocation points, and the overall pointing error $\epsilon(k)$ is calculated via the two-norm. Changing the cost function of Eq. (3.1) to Eq. (3.3) forces the PS optimizer to minimize both the final time of the run and pointing error of the satellite at every time step during the targeting mission including during slew time. The α parameter in the revised cost function

$$
J_1(\vec{x}, \vec{u}, t) = t_f + \alpha \sum_{k=1}^{N_{ts}} \epsilon_i(k)
\tag{3.3}
$$

is a scaling parameter set to adjust the impact of the final time and error terms on the overall cost function value. Scaling the error term down results in a greater dependence

on final time. The α parameter was set to a value of one half to emphasize the final time in the optimization. Further refinement of the off-line optimization scaling is a topic recommended for further research in Section 5.3.

Performing a PS optimization of the stated problem shows the best possible solution to the problem while meeting the physical constraints. The optimization performed for this research provides a benchmark with which to compare the applied analytical closed-loop control scheme solutions. While developing the analytical simulation, initial runs resulted in final times which were faster than the optimal solution. The unfeasible control solution occurred because the actuators and s/c were commanded to change rates at magnitudes that exceeded known limits. Therefore, the optimized benchmark solution spurred the need for the limit enforcement block described below. In Section 3.2.8, the subject of optimization re-emerges as a means of calculating preferred gimbal angles.

3.2   Analytical Model Closed-Loop Control Scheme

Once an optimal solution is computed, attention turns to creating a closed-loop numerical simulation. The closed-loop simulation follows the flow of operations shown in Figure 3.3. The parameters listed on each arrow are output variables created by the block preceding that arrow. Each block of Figure 3.3 is now described in following sections.
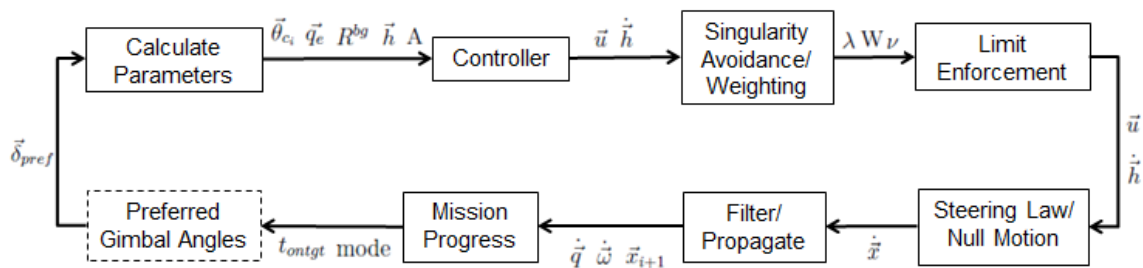
Figure 3.3: Analytical Model Closed-Loop Control Scheme

3.2.1 Calculate Parameters.

The commanded Euler angles $\vec{\theta}_{c_i}$, from the Calculate Parameters block of Figure 3.3 are determined at each time step to point the s/c at each target. Since the s/c relative ground velocity is held as a known constant based on the orbit, for simplicity θ_{c_2} can be found based on a function of simulation time, initial spacecraft attitude, and target coordinates from Table 3.1. These commanded Euler angles are converted to quaternions and compared to the propagated quaternions from the previous time step to generate the quaternion error $\vec{q}_e$. The quaternion error feeds directly into the controller as shown in Figure 3.3.

Rotation matrices R_i^{bg} for each actuator are also calculated at each time step as part of the Calculate Parameters block of Figure 3.3. The method used to calculate rotation matrices for the pyramid of SGCMG actuators was described in Section 2.1. These SGCMG rotation matrix calculations require the current gimbal angles $\vec{\delta}_i$, the constant angle of the CMG as determined from the gimbal support arms β, and knowledge of the clocking order of the gimbals on the spacecraft. Rotation matrices for the three reaction wheels are constant in time since the reaction wheel momentum vectors do not change. These reaction wheel rotation matrices are calculated for the AFIT SimSat geometry of Figure 3.2 using the same method as the SGCMG rotation matrices, holding the $\vec{\delta}$ angle at a constant zero degrees and are

$$R_{RW_1}^{bg} = \begin{bmatrix} 0 & 0 & 1 \\ -1 & 0 & 0 \\ 0 & -1 & 0 \end{bmatrix}, \tag{3.4}$$

$$R_{RW_2}^{bg} = \begin{bmatrix} 1 & 0 & 0 \\ 0 & 0 & 1 \\ 0 & -1 & 0 \end{bmatrix}, \tag{3.5}$$

54

and

$$R_{RW_3}^{bg} = \begin{bmatrix} -1 & 0 & 0 \\ 0 & 1 & 0 \\ 0 & 0 & -1 \end{bmatrix}. \tag{3.6}$$

Once the actuator rotation matrices have been determined, the actuator angular momentum $\vec{h}_{act}$ and A matrix of Eqs. (2.8) and (2.13) can be calculated for the current time step. The angular momentum magnitude for a SGCMG is a constant since the rotor spins at a constant rate. For ease of notation, this SGCMG angular momentum magnitude is denoted

$$h_0 = C_{ri}\dot{\psi} \tag{3.7}$$

where C_{ri} is the rotor inertia about the spin axis and $\dot{\psi}$ is the constant SGCMG rotor spin rate. For a RWCMG system as depicted in Figure 3.2 containing a pyramid of four SGCMG and three reaction wheels, the angular momentum vector is then calculated as

$$
\begin{aligned}
\vec{h}_{act} = R_{RW_1}^{bg}\begin{bmatrix} 0 \\ 0 \\ C_{r_{RW1}}\dot{\psi}_{RW1} \end{bmatrix} + R_{RW_2}^{bg}\begin{bmatrix} 0 \\ 0 \\ C_{r_{RW2}}\dot{\psi}_{RW2} \end{bmatrix} + R_{RW_3}^{bg}\begin{bmatrix} 0 \\ 0 \\ C_{r_{RW3}}\dot{\psi}_{RW3} \end{bmatrix} \\
+ R_{CMG_1}^{bg}\begin{bmatrix} 0 \\ 0 \\ h_0 \end{bmatrix} + R_{CMG_2}^{bg}\begin{bmatrix} 0 \\ 0 \\ h_0 \end{bmatrix} + R_{CMG_3}^{bg}\begin{bmatrix} 0 \\ 0 \\ h_0 \end{bmatrix} + R_{CMG_4}^{bg}\begin{bmatrix} 0 \\ 0 \\ h_0 \end{bmatrix}.
\end{aligned}
\tag{3.8}
$$

Computing the Jacobian of Eq. (3.8), and assuming all reaction wheels have the same spin axis inertia C_{RW} the $A(\dot{\vec{\psi}}, \vec{\delta})$ matrix for the subject RWCMG system is

$$A(\dot{\vec{\psi}}, \vec{\delta}) = \begin{bmatrix} C_{RW} & 0 & 0 & -h_0 c\beta c\delta_1 & h_0 s\delta_2 & h_0 c\beta c\delta_3 & -h_0 s\delta_4 \\ 0 & C_{RW} & 0 & h_0 s\delta_1 & h_0 c\beta c\delta_2 & -h_0 s\delta_3 & -h_0 c\beta c\delta_4 \\ 0 & 0 & -C_{RW} & h_0 s\beta c\delta_1 & h_0 s\beta c\delta_2 & h_0 s\beta c\delta_3 & h_0 s\beta c\delta_4 \end{bmatrix} \tag{3.9}$$

where $c\beta$ and $s\beta$ are the cosine and sine functions of the β angle respectively, and c and s preceding a δ_i is the cosine or sine function of the respective gimbal angle. Once all the

55

stated parameters are calculated for the time step, the next event in the closed-loop control scheme is to determine the desired control value $\vec{u}$ and associated torque value $\dot{\vec{h}}$.

3.2.2 Controller Implementation.

The purpose of the Controller block in Figure 3.3 is to generate the control signal $\vec{u}$ or $\dot{\vec{h}}$. Recall from Eq. (2.17) that $\vec{u}$ and $\dot{\vec{h}}$ are related by the nonlinear term $\vec{\omega} \times \vec{h}_{act}$ - meaning, if the Controller outputs $\vec{u}$, then $\dot{\vec{h}}$ is immediately known and vice versa. Section 2.4 described the three controllers being evaluated for the RWCMG system: proportional-integral-derivative (PID), quaternion feedback (QF), and nonlinear Lyapunov-based (LB) controllers. We will now discuss each one in the order listed.

As discussed in Section 2.4 the PID controller used for this research has three gains: K_p, K_d, and K_i. PID gains are selected based on desired natural frequency and damping ratio values of $\omega_n = 0.7$ and $\zeta = 0.707$ using Eq. (2.33). The PID controller as presented in Section 2.4 has no built-in method of enforcing constraints as does other controllers. Spacecraft states such as reaction wheel, gimbal, and s/c angular slew rates have limitations imposed in hardware experiments. Motors have maximum spin rates or torque levels. Measurement devices, such as the inertial measurement unit, have internal gyro saturation limits. Analytical simulations, and more specifically their controllers, do not possess an inherent ability to rigorously enforce constraints of this nature.

Though a later step in the analytical closed-loop control scheme, Limit Enforcement, imposes the bulk of the desired constraints on the simulation, a modification to the standard PID forces the output of a control signal which has been pre-conditioned. As the first step to correct the deficiency in constraint capability, a saturation function is wrapped around the basic PID controller. This saturation function takes the form

$$\vec{u} = \text{sat}\left[(K_p \vec{q}_e + K_d \dot{\vec{q}}_e + K_i \int \vec{q}_e \, \mathrm{d}t), umax, -umax\right] \tag{3.10}$$

where *umax* is the maximum desired controller output. Similar to the QF controller, the saturation function serves to limit controller output based on a maximum desired value

56

for the overall controller output. Use of Eq. (2.17) translates *umax* into a maximum torque value $\dot{\vec{h}}_{\max}$. For a hardware simulator such as SimSat, previous experiments have determined a maximum s/c torque level to observe in order to avoid collision of the simulator frame with the air bearing pedestal [32; 57]. This maximum torque value is applicable to all three axes and is 0.25 Nm as mentioned before. However, for actual spacecraft, we recognize this air bearing limitation is nonexistent. Barring any payload sensitivities, the maximum torque value to impose on the controller may be limited only by the physical limitations of the actuators such as maximum CMG gimbal rate or RW acceleration. To address controller torque output limit, assuming no prior knowledge other than actuator limits, a preliminary algorithm called the $\dot{\vec{h}}_{\max}$ routine is developed and is now briefly outlined.

The $\dot{\vec{h}}_{\max}$ routine runs one time only per RWCMG mission simulation, prior to the start of the closed-loop control scheme. A sequential quadratic programming optimization routine is used to minimize $\dot{\vec{h}}$ (absolute value of the output provides the maximum). The dynamic involved is Eq. (2.14). Thus, the controls are CMG gimbal rates $\dot{\vec{\delta}}$ and RW accelerations $\ddot{\vec{\psi}}$. Maximum and minimum gimbal rates and reaction wheel accelerations are imposed as upper and lower bound limits. Note however that the $A(\dot{\vec{\psi}}, \vec{\delta})$ matrix in this optimization depends on specific gimbal angles $\vec{\delta}$ and reaction wheel rates $\dot{\vec{\psi}}$. To verify that the $\dot{\vec{h}}_{\max}$ routine only needs to be performed once before the closed-loop scheme starts, a test was performed in which the $\dot{\vec{h}}_{\max}$ optimization was performed at every time step in simulation. Results of this test showed that the maximum torque value differed by no greater than 0.025% over the whole mission. Due to the nonlinear equations involved in satellite control, the $\dot{\vec{h}}_{\max}$ value is further checked and limited if necessary in the Limit Enforcement block as discussed in Section 3.2.4. The $\dot{\vec{h}}_{\max}$ computed in this preliminary optimization routine is used for all three controllers.

The QF controller, Eq. (2.34), also has three gains: K, C, and P, which are determined based on the same natural frequency and damping ratio values as the PID controller per the algorithm detailed in Section 2.4. Note that the QF controller has two built-in limiters via saturation functions. The outer saturation function uses the $\vec{\dot{h}}_{\max}$ value determined above. The inner saturation function sat($P\vec{q}_e$) limits spacecraft slew rate with limits of ± 1 [27]. Wie developed the QF controller based on assumptions of a rest-to-rest maneuver consisting of the following phases: acceleration, coast, and deceleration. In other words, the controller works best on non-moving targets for which the s/c attitude at the destination is held constant. Though the representative mission depicted in Figure 1.1 requires the spacecraft to track targets as it progresses along the orbital vector, the QF controller is selected for evaluation for this mission due to its large-angle performance benefits over the PID. Logically, the next controller is implemented to address the moving target shortfall of the previous two controllers.

The LB controller, Eq. (2.37), has two gains: K and P. They too are computed using the same natural frequency and damping ratio values of $\omega_n = 0.7$ and $\zeta = 0.707$ as the other controllers. Like the PID controller, the LB controller does not have any embedded rate limiters. Thus a saturation function is wrapped around the LB controller as

$$
\begin{aligned}
\vec{\dot{h}}_{act} = & \ \mathrm{sat}\Big[Kq_e - P\delta\vec{\omega} - \vec{\omega}\times\vec{h}_{act} - I(\vec{\dot{\omega}}_r - \vec{\omega}\times\vec{\omega}_r) + \\
& \sum_{i=1}^{N} C_r(\dot{\vec{\psi}}_i\vec{\omega}_2 R_{i_1}^{bg} - \dot{\vec{\psi}}_i(c\delta_i\vec{\omega}_1 - s\delta_i\vec{\omega}_3)R_{i_2}^{bg}), \vec{\dot{h}}_{\max}, -\vec{\dot{h}}_{\max}\Big].
\end{aligned}
\tag{3.11}
$$

Note that since the LB controller computes $\vec{\dot{h}}$ directly, the $\vec{\dot{h}}_{\max}$ value from the preliminary max torque optimization routine described above can be directly inserted into the controller saturation function without conditioning through Eq. (2.17). Also of unique interest for implementing the LB controller is calculation of the summation term. The N of the summation term is the number of actuators. For the RWCMG system, care must be taken to delineate between CMG and RW actuators for the C_r, $\dot{\psi}_i$, and R_i^{bg} elements. The desired angular velocity and acceleration are calculated based on the difference of commanded

Euler angles $\vec{\theta}_{c_i}$ between the current and previous time steps. Unlike the QF controller, the LB controller requires no assumptions about the maneuver to which it is applied.

The performance of each controller with respect to the representative RWCMG mission is presented in Chapter IV (Section 4.1). Though a preliminary control limit value is imposed on each controller via the outer saturation function, more hardware limits are desirable in a realistic simulation. However, to impose more hardware limits, the analytical simulation must evaluate equations of motion such as the weighted pseudo-inverse of Eq. (2.28). In order to calculate the equations of motion, the singularity avoidance parameter λ and weighting matrix W are needed. The next section details the calculation of the λ parameter for the SGCMG system and the W matrix for the RWCMG system which in-turn enable the hardware limit algorithm.

3.2.3 *Singularity Avoidance and Weighting.*

A goal of the presented research is to assess the benefits of a RWCMG system as compared to the SGCMG system. Therefore, a SGCMG steering law is needed for the baseline system. The SGCMG law used in both the numerical simulation and hardware experiment is a generalized SR CMG steering law from [27] and is

$$
\begin{aligned}
\dot{\vec{\delta}} &= A^T (AA^T + \lambda\Theta)^{-1} \dot{\vec{h}}_{act} \\
\lambda &= \begin{cases} \lambda_0 (1 - m_i/m_0)^2, & \text{for } m_i < m_0 \\ 0, & \text{for } m_i \geq m_0 \end{cases} \\
m_i &= \sqrt{\det(AA^T)}
\end{aligned}
\tag{3.12}
$$

where Θ is a 3x3 identity matrix. The constants λ_0 and m_0 are left to be determined. The quantity $\sqrt{\det(AA^T)}$ approaches zero as singularies are encountered. The λ parameter becomes non-zero when the m_i drops below the desired m_0 threshold and forces the gimbal rate to steer around the singularity. Avoiding a singularity in this manner results in a torque error that creates an undesired deviation from the intended control path. However, the amount of unwanted deviation can be controlled through adjustment of the λ_0

parameter. Away from singularities, the SGCMG steering law computes $\dot{\vec{Y}}$ from the Moore-Penrose pseudo-inverse of Eq. (2.18). Calculation of the λ parameter in this Singularity Avoidance/Weighting block of the closed-loop control scheme enables the CMG steering law to be exercised in the Limit Enforcement step of the next section.

The second parameter calculated in the Singularity Avoidance/Weighting step of Figure 3.3 is the weighting matrix W. Equation (3.12) yields gimbal rates for the SGCMG system. Gimbal rates $\dot{\vec{\delta}}$ and reaction wheel accelerations $\ddot{\vec{\psi}}$ for the RWCMG system are computed from the Schaub weighted pseudo-inverse of Eq. (2.28). The weighting matrix in Eq. (2.28) is used as a switch to select which actuators are steering the spacecraft at any given time. For a RWCMG system with four SGCMG and three reaction wheels, the weighting matrix W is a 7x7 diagonal matrix. The weighting matrix W is also used in the null motion scheme and is discussed further in Section 3.2.5. However, the weighting matrix W also plays a role in singularity avoidance for the RWCMG system. During slew phases of the representative mission - when the spacecraft has finished imaging the current target for the specified dwell time and now must slew over a relatively large angle to the next target - the CMG pyramid is the desired actuator system due to higher torque capability compared to the reaction wheels. When performing the slew, the CMG pyramid of the RWCMG system is susceptible to singularities just as the CMG pyramid of the SGCMG system is. When a singularity is encountered by the CMG pyramid, the RWA can be used to provide the desired torque without resorting to an undesirable detour in the control path. Adjusting the weighting matrix W is the mechanism for performing this scheme. Recalling the output of Eq. (2.28) is a 7x1 vector of three reaction wheel accelerations and four CMG gimbal rates, the first three diagonal values of the W matrix turn on/off the reaction wheels and the final four diagonal values turn on/off the CMG actuators. When a slew phase starts, the CMG actuators should be on and the reaction wheels should be on standby awaiting singularity avoidance duty. The reaction wheels only apply a torque if the CMG pyramid

encounters a singularity. The W matrix, which is used to control these behaviors, is

$$W = \begin{bmatrix} W_{RW_1} & 0 & 0 & 0 & 0 & 0 & 0 \\ 0 & W_{RW_2} & 0 & 0 & 0 & 0 & 0 \\ 0 & 0 & W_{RW_3} & 0 & 0 & 0 & 0 \\ 0 & 0 & 0 & 1 & 0 & 0 & 0 \\ 0 & 0 & 0 & 0 & 1 & 0 & 0 \\ 0 & 0 & 0 & 0 & 0 & 1 & 0 \\ 0 & 0 & 0 & 0 & 0 & 0 & 1 \end{bmatrix}. \tag{3.13}$$

As in Section 2.3, the reaction wheel weighting values W_{RW_i} are adjusted by the parameter v at each time step from

$$W_{RW_i} = W^0_{RW_i} e^{-\mu v} \tag{3.14}$$

where v is the singularity nearness metric shown in Eq. (2.29) and $W^0_{RW_i}$ and μ are positive scalars. Schaub developed these equations for an analytical study of a VSCMG but here they are adapted for use in the RWCMG system [8]. If the RWCMG CMG system encounters a singularity during the slew phase, the W_{RW_i} values increase in magnitude, allowing the desired control path to be actuated by the reaction wheels. Calculation of the λ and W parameters in the Singularity Avoidance and Weighting step of the closed-loop control scheme allows Eq. (3.12) for the SGCMG system, and Eq. (2.28) for the RWCMG system, to calculate actuator derivatives. These derivatives are needed in the next step of the closed-loop control scheme, Limit Enforcement.

3.2.4 *Limit Enforcement.*

When creating the analytical model, a major consideration for each controller discussed in Section 3.2.2 is its ability to enforce limits based on actual hardware constraints. Hardware constraint limits can be broken into two major categories: control and spacecraft kinematic. Control limits include such physical phenomena as overall control system torque, reaction wheel maximum rotation rates and accelerations, and

CMG maximum gimbal rates and accelerations. Spacecraft kinematic limits include such constraints as maximum slew rate (usually due to rate gyro saturation of an inertial navigation system) and maximum off-nadir angle. As the Controller step of the closed-loop control scheme finishes, only maximum spacecraft torque has been addressed by the PID and LB controllers and torque and slew rate by the QF controller. Thus, a separate algorithm is necessary to check and enforce other hardware limits that may be violated as a result of control torques $\vec{u}$ or $\dot{\vec{h}}$ that may exceed limits.

Since the purpose of the Limit Enforcement block of the closed-loop control scheme is to condition the controller values, the method starts with checking for violation of max controller torque $\dot{\vec{h}}_{act}$. Recall from Eq. (2.17) that the value $\dot{\vec{h}}_{act}$ and $\vec{u}$ are related by the known nonlinear term $\vec{\omega} \times \vec{h}_{act}$. Therefore, a check against positive and negative maximum torque values ensures that the controller specified torque $\dot{\vec{h}}_{act}$ are within desired limits:

$$- \dot{\vec{h}}_{max} \leq \dot{\vec{h}}_{act} \leq \dot{\vec{h}}_{max}. \tag{3.15}$$

Equation (3.15) limits both $\dot{\vec{h}}_{act}$ and $\vec{u}$. Once the $\dot{\vec{h}}_{act}$ value has been enforced, the corresponding $\vec{u}$ value is computed. A saturation function is used in the controller block to limit the torque value, however this procedure, called $\dot{\vec{h}}_{LIM}$, is repeated at later stages of the algorithm to ensure other enforced hardware limits do not cause the maximum torque to be violated.

The next parameter checked in the Limit Enforcement block of the closed-loop control scheme is the spacecraft maximum slew rate $\vec{\omega}_{max}$. First, Euler's equation (Eq. (2.16)) is used to calculate the anticipated spacecraft slew acceleration given the current controller-derived $\vec{u}$. A simple integration using the program's fixed time step then yields the spacecraft anticipated slew rate at the next time step $\vec{\omega}_{i+1}$. Next, $\vec{\omega}_{i+1}$ is limited by intended spacecraft slew rate values according to

$$- \vec{\omega}_{max} \leq \vec{\omega}_{i+1} \leq \vec{\omega}_{max}. \tag{3.16}$$

If a violation of the spacecraft slew rate is detected and enforced, the derivative $\dot{\vec{\omega}}_{i+1}$ is computed. A manipulated version of Euler's equation shown in Eq. (3.17) then adjusts the controller value $\vec{u}$ for the limited slew rate

$$\vec{u} = -I\dot{\vec{\omega}}_{i+1} - \vec{\omega} \times I\vec{\omega}. \tag{3.17}$$

With the adjusted $\vec{u}$ parameter, the associated $\dot{\vec{h}}_{act}$ is calculated. Finally, the $\dot{\vec{h}}_{LIM}$ procedure is run again to ensure the changes to the control values due to spacecraft limit enforcement did not cause a new violation of control torque limits. All of these checks are necessary because without them the analytical closed-loop control scheme produces near-optimal slew times via actuation that vastly exceeds known hardware constraints.

The next parameters treated in the Limit Enforcement block algorithm are CMG gimbal rates $\dot{\vec{\delta}}$ and reaction wheel accelerations $\ddot{\vec{\psi}}$. First the anticipated gimbal rates and reaction wheel accelerations required to generate the current $\dot{\vec{h}}_{act}$ are pre-calculated with pseudo-inverse equations of motion described in Section 3.2.5. Next, desired hardware limits are enforced on $\dot{\vec{\delta}}$ and $\ddot{\vec{\psi}}$

$$
\begin{aligned}
-\dot{\vec{\delta}}_{max} &\leq \dot{\vec{\delta}} \leq \dot{\vec{\delta}}_{max} \\
-\ddot{\vec{\psi}}_{max} &\leq \ddot{\vec{\psi}} \leq \ddot{\vec{\psi}}_{max}.
\end{aligned}
\tag{3.18}
$$

If a violation of gimbal rates or reaction wheel accelerations is detected and enforced, the pseudo-inverse equations of motion used to determine $\dot{\vec{\delta}}$ and $\ddot{\vec{\psi}}$ are manipulated to calculate the required control system torque $\dot{\vec{h}}_{act}$ that results from the new anticipated actuator values. Finally, the $\dot{\vec{h}}_{LIM}$ procedure is again run to ensure torque limits are not violated with the new actuator values.

Control moment gyroscope acceleration limits $\ddot{\vec{\delta}}$ are also constrained in the Limit Enforcement block in the same manner as the above parameters. Reaction wheel rotation rates are not limited by the algorithm since the basic representative mission does not stress the reaction wheel rates given the spacecraft parameters of Figure 3.1. Thus the reaction

wheels did not come close to saturating, or reaching their maximum spin rate, during the analytical model runs. Similarly, maximum spacecraft off-nadir angle is not actively limited in the Limit Enforcement block of the closed-loop control scheme. Rather, targets are selected to intentionally not stress this hardware limit.

The iterative method of enforcing hardware limits in the analytical RWCMG model does require the equations of motion to be calculated twice - once in the Limit Enforcement block and again in the Steering/Null Motion block. However, since the purpose of the analytical model is to predict results from a hardware experiment, less emphasis is placed on efficient computation speed of the algorithms than on obtaining results representative of real-world experiments. The required use of pseudo-inverses for the equations of motion does introduce an error into the Limit Enforcement algorithm. Performance results of the Limit Enforcement algorithm are discussed in Section 4.2. With conditioned $\vec{u}$ and $\dot{\vec{h}}_{act}$ values from this block, the equations of motion can now be run for the final time to produce state parameters. The specific equations of motion for the Steering/Null Motion block of the closed-loop control scheme are discussed in the following section.

3.2.5   *Steering Law/Null Motion.*

With the control parameters $\vec{u}$ and $\dot{\vec{h}}_{act}$ conditioned based on expected hardware limits in the previous step, the next step in the closed-loop control scheme of Figure 3.3 is applying the equations of motion to the states in the block called Steering Law/Null Motion. The states of the RWCMG closed-loop control scheme are: quaternions $\vec{q}$, spacecraft angular rates $\vec{\omega}$, gimbal angles $\vec{\delta}$, gimbal rates $\dot{\vec{\delta}}$, reaction wheel rates $\dot{\vec{\psi}}$, and reaction wheel accelerations $\ddot{\vec{\psi}}$. The equations of motion provide the derivative values of the states so that the states can be propagated to the next time step in the Filter/Propagate block. Since CMG gimbal angles are included in the states of the closed-loop control scheme, the null motion of those gimbal angles must also be addressed in this block.

64

First the quaternion state derivatives are calculated through the quaternion differential, Eq. (2.19). The spacecraft angular rate state derivatives are calculated with Euler's equation of Eq. (2.16). Next, a determination is made as to the current mode the spacecraft is in. The two modes of the modeled RWCMG mission are slew and collect. Further discussion of how the two modes are determined can be found in Section 3.2.7.

During slew mode, the desired steering law is for the CMG pyramid to provide the required actuator torque while the reaction wheel array is held in stand-by in the event of an internal singularity in the CMG pyramid. As discussed in Section 3.2.3, the mechanism for selecting the contribution of each actuator for providing the desired torque $\dot{\vec{h}}_{act}$ is adjusting the W matrix. The derivatives of reaction wheel rates and gimbal angles are then calculated with Schaub's weighted pseudo-inverse of Eq. (2.28).

During collect mode, the desired steering law is for the reaction wheel array to provide the required actuator torque to continue tracking the target while the CMG array uses null motion to adjust gimbal angles to preferred values. When the transition from slew mode to collect mode occurs, the equations of motion do not immediately switch from Eq. (2.28) to the null motion equations. Though controller gains are adjusted for minimal overshoot and settling time through careful selection of damping ratio and natural frequency, a period of transition in which the CMG pyramid remains as the source of $\dot{\vec{h}}_{act}$ after collection starts helps prevent saturation of reaction wheels. During this transition time the CMG pyramid contribution to the desired torque is linearly decreased and the contribution from the reaction wheels is linearly increased. This transition is accomplished via the W matrix of Eq. (2.28). During slew mode, the diagonal elements of W corresponding with the CMG pyramid are held at a constant value of one as shown in Eq. (3.13). During the transition period from slew to collect mode, the weighting matrix values are set according

to Eq. (3.19)

$$W = \begin{bmatrix} W_{RW_1} & 0 & 0 & 0 & 0 & 0 & 0 \\ 0 & W_{RW_2} & 0 & 0 & 0 & 0 & 0 \\ 0 & 0 & W_{RW_3} & 0 & 0 & 0 & 0 \\ 0 & 0 & 0 & W_{CMG_1} & 0 & 0 & 0 \\ 0 & 0 & 0 & 0 & W_{CMG_2} & 0 & 0 \\ 0 & 0 & 0 & 0 & 0 & W_{CMG_3} & 0 \\ 0 & 0 & 0 & 0 & 0 & 0 & W_{CMG_4} \end{bmatrix}$$

$$W_{RW_i} = \frac{t_{ontgt}}{t_{trans}} \qquad W_{CMG_i} = 1 - \frac{t_{ontgt}}{t_{trans}} \tag{3.19}$$

where t_{trans} is the selected transition time and t_{ontgt} is the amount of dwell time the satellite

has been collecting on the current target. The t_{trans} value is a hard-coded constant for the

purposes of this research and is selected to allow sufficient time for oscillations to dampen

while leaving enough dwell time on target to allow null motion to take place. Further

investigation into the determination of the transition time is a recommended subject for

further investigation in Chapter V. The t_{ontgt} is determined in the Mission Progress block

of the closed-loop control scheme and is discussed further in Section 3.2.7. When t_{ontgt} is

equal to t_{trans}, the W matrix is

$$W = \begin{bmatrix} 1 & 0 & 0 & 0 & 0 & 0 & 0 \\ 0 & 1 & 0 & 0 & 0 & 0 & 0 \\ 0 & 0 & 1 & 0 & 0 & 0 & 0 \\ 0 & 0 & 0 & 0 & 0 & 0 & 0 \\ 0 & 0 & 0 & 0 & 0 & 0 & 0 \\ 0 & 0 & 0 & 0 & 0 & 0 & 0 \\ 0 & 0 & 0 & 0 & 0 & 0 & 0 \end{bmatrix} \tag{3.20}$$

which means the reaction wheels are providing the full desired torque $\dot{\vec{h}}_{act}$ through

continued use of Eq. (2.28). The CMG pyramid is no longer participating in control of

the spacecraft. At this point, the CMG gimbal rates calculated in Eq. (2.28) are zero and are ignored for the duration of collect mode. CMG gimbal rates are instead commanded with null motion equations during the collect mode.

At the point when t_{ontgt} is equal to t_{trans}, the null motion of CMG gimbal angles begins. The reaction wheels provide $\dot{\vec{h}}_{act}$ to track the current target as the spacecraft travels along its orbital trajectory. The steering law, which determines gimbal rates, now changes to a modified version of Eq. (2.41). Since the reaction wheels are tasked with three-axis control of the spacecraft, they are removed from the null motion steering law and only the CMG pyramid is considered. In addition, the weighting matrix W is no longer needed to delineate actuator roles. Therefore, the pseudo-inverse involved with the null motion is a simple non-weighted Moore-Penrose inverse. The T matrix from Eq. (2.41) is also omitted since it is an identity matrix for this application - null motion is desired for all four CMG actuators. The null motion steering law used in this research is

$$
\begin{bmatrix} \dot{\delta}_1 \\ \dot{\delta}_2 \\ \dot{\delta}_3 \\ \dot{\delta}_4 \end{bmatrix} = k(A_c^T (A_c A_c^T)^{-1} A_c - I_{4x4})(\vec{\delta} - \vec{\delta}_{pd}). \tag{3.21}
$$

The A_c matrix is the 3x4 matrix consisting of the four right-most columns of the full 3x7 $A(\dot{\vec{\psi}}, \vec{\delta})$ matrix from Eq. (3.9) - the portion of the $A(\dot{\vec{\psi}}, \vec{\delta})$ matrix pertaining to the CMG pyramid. Preferred gimbal angles $\vec{\delta}_{pd}$ are calculated in the Preferred Gimbal Angles block of the closed-loop control scheme and are discussed further in Section 3.2.8. Through use of Eq. (3.21), the gimbal angles travel along null motion paths until they are least-squares close to the preferred values. Since the internal momentum vector of the satellite must be maintained, the null motion algorithm does not allow the gimbal angles to travel exactly to the preferred values. A recommendation for further study of the accuracy of null motion trajectories as the number of actuators is increased is made in Chapter V.

When the desired dwell time on the current target has been completed, the satellite then re-enters slew mode for the next target if it has not reached the end of the representative mission shown in Figure 1.1. Unlike the transition from slew to collect mode, the transition from collect to slew mode is made immediately with no transition time. CMG gimbal angle rate calculations are changed from Eq. (3.21) back to Eq. (2.28) and the weighting matrix is reset to that shown in Eq. (3.13). During the slew phase, the reaction wheel rates remain constant at the rate they are spinning when the collect phase ends unless they are needed to overcome a singularity during the slew. This concludes discussion of calculation of the CMG gimbal angle and reaction wheel rate derivatives. With all state derivative values calculated, the next step in the closed-loop control scheme is to apply filtering and propagate the states to the next time step.

3.2.6 *Filter/Propagate.*

With the derivative values of the model states calculated in the previous step, the closed-loop control scheme now enters the Filter/Propagate block. For calculation of the closed-loop control scheme without noise or filtering, the Filter/Propagate block performs a propagation of the states based on the derivative values from the previous block and a constant simulation time step. In fact, for the analytical model of this research, this noise-free run of the code is used as the truth signal for filter assessment. Prior to running the closed-loop control scheme with the noise and filter turned on, the complete closed-loop algorithm is run through the entire representative mission one time to generate a truth signal that is based solely on the equations of motion from Section 3.2.5. The remainder of this section highlights the methods of implementing the Extended Kalman Filter (EKF) and Unscented Kalman Filter (UKF) introduced in Section 2.7 in the analytical RWCMG model.

Though the basic steps of the EKF and UKF are described in Chapter II, a discussion of the basic setup of the stochastic filtering algorithms is in order. First, consideration must

be given to which states are going to be filtered. While the filtering techniques described thus far can apply to any states for which a measurement source and equations of motion are available, attitude in the form of quaternions $\vec{q}$ and spacecraft angular rates $\vec{\omega}$ are chosen to demonstrate the algorithms. Spacecraft quaternions can feasibly be estimated from measurements from real-world hardware systems through use of attitude determination systems like star sensors, sun sensors, and inertial measurement units. Spacecraft angular rate measurement similarly has a number of sensor options in real-world systems.

For this research, direct quaternion estimates generated from spacecraft angular velocity measurements are assumed to be available. These measurements, corresponding to $\vec{y}$ of Eq. (2.42), are generated by first deterministically propagating the quaternions and angular rates to the next time step using the equations of motion from Section 2.1. Then, a representation of sensor measurement noise is added to each of the seven propagated filter states by adding a normally distributed random variable multiplied by an associated noise strength parameter, on the order of 1×10^{-5} for quaternions and 1×10^{-3} for s/c angular rate, which represents $\vec{v}(t_i)$ of Eq. (2.42).

Once measurements are generated, attention turns to calculation of the state transition matrix Φ for use in the EKF algorithm. Since the analytical simulation is run in discrete time and the equations of motion are used to generate discrete derivatives of the states, the state transition matrix for this research is the Jacobian of the quaternion and angular rate state equations of motion - Eqs. (2.19) and (2.16), respectively. These equations of motion for the RWCMG system, which are the $\vec{a}(\vec{x}(t), \vec{u}(t), t)$ of Eq. (2.43), are shown in full form as

$$
\begin{aligned}
\dot{q}_1 &= \tfrac{1}{2}(q_2\omega_3 - q_3\omega_2 + q_4\omega_1) \\
\dot{q}_2 &= \tfrac{1}{2}(-q_1\omega_3 + q_3\omega_1 + q_4\omega_2) \\
\dot{q}_3 &= \tfrac{1}{2}(q_1\omega_2 - q_2\omega_1 + q_4\omega_3) \\
\dot{q}_4 &= \tfrac{1}{2}(-q_1\omega_1 - q_2\omega_2 - q_3\omega_3)
\end{aligned}
\tag{3.22}
$$

and

$$\dot{\omega}_1 = \begin{cases} -\dfrac{h_0}{A}(-c\beta c\delta_1\dot{\delta}_1 + s\delta_2\dot{\delta}_2 + c\beta c\delta_3\dot{\delta}_3 - s\delta_4\dot{\delta}_4) - \dfrac{1}{A}(C_r\ddot{\psi}_1 + (C - B)\omega_2\omega_3) \\[2mm] +\dfrac{\omega_3}{A}(-h_0c\delta_1 + h_0c\beta s\delta_2 + h_0c\beta c\delta_3 - h_0c\beta s\delta_4 + C_r\dot{\psi}_2) \\[2mm] -\dfrac{\omega_2}{A}(h_0s\beta s\delta_1 + h_0s\beta s\delta_2 + h_0s\beta s\delta_3 + h_0s\beta s\delta_4 - C_r\dot{\psi}_3) \end{cases}$$

$$\dot{\omega}_2 = \begin{cases} -\dfrac{h_0}{B}(s\delta_1\dot{\delta}_1 + c\beta c\delta_2\dot{\delta}_2 - s\delta_3\dot{\delta}_3 - c\beta c\delta_4\dot{\delta}_4) - \dfrac{1}{B}(C_r\ddot{\psi}_2 + (A - C)\omega_1\omega_3) \\[2mm] -\dfrac{\omega_3}{B}(-h_0c\beta s\delta_1 - h_0c\delta_2 + h_0c\beta s\delta_3 + h_0c\delta_4 + C_r\dot{\psi}_1) \\[2mm] -\dfrac{\omega_1}{B}(h_0s\beta s\delta_1 + h_0s\beta s\delta_2 + h_0s\beta s\delta_3 + h_0s\beta s\delta_4 - C_r\dot{\psi}_2) \end{cases} \qquad .$$

$$\dot{\omega}_3 = \begin{cases} -\dfrac{h_0}{C}(s\beta c\delta_1\dot{\delta}_1 + s\beta c\delta_2\dot{\delta}_2 + s\beta c\delta_3\dot{\delta}_3 + s\beta c\delta_4\dot{\delta}_4) - \dfrac{1}{C}(C_r\ddot{\psi}_3 - (B - A)\omega_1\omega_2) \\[2mm] +\dfrac{\omega_2}{C}(-h_0c\beta s\delta_1 - h_0c\delta_2 + h_0c\beta s\delta_3 + h_0c\delta_4 + C_r\dot{\psi}_1) \\[2mm] -\dfrac{\omega_1}{C}(-h_0c\delta_1 + h_0c\beta s\delta_2 + h_0s\delta_3 - h_0c\beta s\delta_4 + C_r\dot{\psi}_2) \end{cases}$$

$$(3.23)$$

The $\dot{\psi}_i$ terms of Eq. (3.23) refer to reaction wheel rates and the C_r terms to reaction wheel spin axis inertia. Spacecraft principal axis frame moment of inertia terms are represented by the A, B, and C terms. The terms cβ and sβ are the cosine and sine functions of the β angle respectively, and c and s preceding a δ_i is the cosine or sine function of the respective gimbal angle. CMG momentum h_0 was defined in Eq. (3.7). The form of the state transition matrix Φ is $e^{\Lambda\Delta t}$ where Δt is the time step and Λ is the Jacobian

$$\Lambda = \frac{\partial \vec{a}}{\partial \vec{x}} = \begin{vmatrix} \dfrac{\partial a_1}{\partial x_1} & \dfrac{\partial a_1}{\partial x_2} & \cdots & \dfrac{\partial a_1}{\partial x_7} \\[2mm] \dfrac{\partial a_2}{\partial x_1} & \dfrac{\partial a_2}{\partial x_2} & \cdots & \dfrac{\partial a_2}{\partial x_7} \\[2mm] \vdots & & \ddots & \vdots \\[2mm] \dfrac{\partial a_7}{\partial x_1} & \cdots & & \dfrac{\partial a_7}{\partial x_7} \end{vmatrix} . \qquad (3.24)$$

where $\vec{a}$ is a 7x1 vector of the equations of motion of Eqs. (3.22) and (3.23) and $\vec{x}$ is the 7x1 vector of filtered states (quaternions and angular rates). The full state Λ matrix for the

RWCMG system is

$$\Lambda = \begin{bmatrix} 0 & \frac{1}{2}\omega_3 & -\frac{1}{2}\omega_2 & \frac{1}{2}\omega_1 & & \frac{1}{2}q_4 & \cdots \\ -\frac{1}{2}\omega_3 & 0 & \frac{1}{2}\omega_1 & \frac{1}{2}\omega_2 & & \frac{1}{2}q_3 & \cdots \\ \frac{1}{2}\omega_2 & -\frac{1}{2}\omega_1 & 0 & \frac{1}{2}\omega_3 & & -\frac{1}{2}q_2 & \cdots \\ -\frac{1}{2}\omega_1 & -\frac{1}{2}\omega_2 & -\frac{1}{2}\omega_3 & 0 & & -\frac{1}{2}q_1 & \cdots \\ 0 & 0 & 0 & 0 & & 0 & \cdots \\ 0 & 0 & 0 & 0 & & (\frac{1}{B})(h_0s\beta s\delta_1 + h_0s\beta s\delta_2 + h_0s\beta s\delta_3 + h_0s\beta s\delta_4 - C_r\dot\psi_3 - (A-C)\omega_3) & \cdots \\ 0 & 0 & 0 & 0 & & -(\frac{1}{C})(-h_0c\beta s\delta_1 + h_0c\beta s\delta_2 + h_0c\beta s\delta_3 - h_0c\beta s\delta_4 + C_r\dot\psi_2 + (B-A)\omega_2) & \cdots \\ \cdots & & -\frac{1}{2}q_3 & & & \frac{1}{2}q_2 & \\ \cdots & & \frac{1}{2}q_4 & & & -\frac{1}{2}q_1 & \\ \cdots & & \frac{1}{2}q_1 & & & \frac{1}{2}q_4 & \\ \cdots & & -\frac{1}{2}q_2 & & & -\frac{1}{2}q_3 & \\ \cdots & & -(\frac{1}{A})(h_0s\beta s\delta_1 + h_0s\beta s\delta_2 + h_0s\beta s\delta_3 + h_0s\beta s\delta_4 - C_r\dot\psi_3 + (C-B)\omega_3) & & & (\frac{1}{A})(-h_0c\delta_1 + h_0c\beta s\delta_2 + h_0c\delta_3 - h_0c\beta s\delta_4 + C_r\dot\psi_2 - (C-B)\omega_2) & \\ \cdots & & 0 & & & -(\frac{1}{B})(-h_0c\beta s\delta_1 - h_0c\delta_2 + h_0c\beta s\delta_3 + h_0c\delta_4 + C_r\dot\psi_1 + (A-C)\omega_1) & \\ \cdots & & (\frac{1}{C})(-h_0c\beta s\delta_1 - h_0c\delta_2 + h_0c\beta s\delta_3 + h_0c\delta_4 + C_r\dot\psi_1 + (B-A)\omega_1) & & & 0 & \end{bmatrix}. \tag{3.25}$$

With the state transition matrix Φ calculated at every time step, the second-order approximation of the dynamics noise distribution matrix Q_{d_i} of Eq. (2.44) can be found using Maybeck's equation [59]

$$Q_{d_i} \approx \frac{1}{2}(\Phi Q_t \Phi^T + Q_t)\Delta t \tag{3.26}$$

where Q_t is the continuous time matrix of dynamics noise and Δt is the time step length. The matrix Q_t, in the case of this research, is a diagonal matrix of values on the order of 1×10^{-2} to model disturbance torques.

Since the filtered states are assumed to be measured directly, the function $c(\vec{x}(t_i), t_i)$ of Eq. (2.43) is a vector of the filtered states. If the measurements consist of quaternions and spacecraft angular acceleration, for example, then the function $c(\vec{x}(t_i), t_i)$ is a vector with quaternions as the first four values, and Euler's equations as the final three values. The matrix C_i in the EKF Update Eq. (2.45) is formed by taking the Jacobian of the $c(\vec{x}(t_i), t_i)$ function. In the case of this research where the filtered states are measured directly, the matrix C_i is a 7x7 identity.

The EKF used in RWCMG analytical simulations follows the steps of Eqs. (2.44) and (2.45) to filter the applied measurement and dynamics noise. A Monte Carlo analysis is performed with 100 runs of the representative mission to assess the performance of the

EKF. Results for the EKF stochastic estimation application on the RWCMG mission are presented in Section 4.4.

Transitioning now to the UKF implementation, the same quaternion and spacecraft angular rate states and measurements are used to assess performance of the UKF. Parameters that needed to be defined for this filter include the tuning values of λ, α, and β (different from the CMG pyramid angle) from Eq. (2.46). For a Gaussian distribution, 2 is an optimal β value. The α and λ parameters are determined by following the procedure in [52]. This procedure seeks to solve the equation $L + \lambda = 3$ where λ is defined

$$\lambda = \alpha^2(L + \kappa) - L \tag{3.27}$$

and κ is simply set to zero. For the case of seven filtered states, L is seven and the resulting α parameter is 0.6547. With these tuning parameters calculated, the UKF propagate and update algorithms from Section 2.7 are followed without modification. The same Monte Carlo analysis of 100 runs of the representative mission is performed with the UKF and a comparison of performance to the EKF is given in Section 4.4. With the closed-loop control scheme state filtered and propagated to the next time step, the next step in the process is to assess progress on imaging the current target.

3.2.7 Mission Progress.

Once the full state has been propagated to the next time step, evaluation of progress in the mission is needed. As mentioned in Section 3.2.5, the two basic modes in the RWCMG model are slew and collect. If the simulation is currently in collect mode, the Mission Progress block of the closed-loop control scheme does the following

- Verify attitude is still within pointing constraints

- Update time on current target t_{ontgt}

- Check whether dwell time is satisfied

To determine whether the satellite attitude is within pointing constraints, a pointing error term is used. The propagated quaternions are first converted to Euler angles then are compared to the commanded Euler angles using a 2-norm as in Eq. (3.2). If the propagated attitude is within the desired tolerance, collection continues. If the attitude drifts out of the tolerance range, then the simulation switches back to slew mode. When the dwell time for the current target is achieved, the simulation changes to slew mode for the next target. During slew mode, the Mission Progress block of the closed-loop control scheme checks whether the propagated state achieves the pointing tolerance for the current target. If the pointing error is within tolerance, the simulation switches back to collect mode.

The t_{ontgt} and mode tracking parameters are key to tracking multiple targets. In addition, the Mission Progress block maintains bookkeeping for the start and finish times of each target. At the start of each collect mode during the closed-loop control scheme, a flag is thrown which triggers the final block of the scheme, Preferred Gimbal Angles.

3.2.8   Calculation of Preferred Gimbal Angles.

The final step in the closed-loop control scheme is Preferred Gimbal Angles. This step is shown with a dashed line in Figure 3.3 because it does not get called at every time step. Preferred gimbal angles are only calculated once per target. The algorithm is called to calculate the desired gimbal angles for the next target when collect mode first begins for the current target. Three algorithms for calculation of preferred gimbal angles are tested in the analytical simulation and two are tested in the hardware simulation.

The first method of calculating preferred gimbal angles is an off-line optimization using a pseudo-spectral method. Like the algorithm in Section 3.1.3, a separate optimization is run for each target of the representative mission using only CMG actuation. This method uses the exact same algorithm as Eqs. (3.1) and (3.3) with one exception. In the benchmark application of Section 3.1.3, the initial states for the first target are constrained to prescribed values and the initial states for targets two through four are set

73

as the final states for the previous target. For the calculation of preferred gimbal angles, the constraints on initial gimbal angle are set as ±360° which means the optimization routine is allowed to find the initial gimbal angles which minimize the cost function. When the optimization solutions for each target are stitched together to form the entire mission this method creates a set of gimbal angles with a discontinuity as the gimbal angles shift abruptly from one value to another at the start of each slew. However, the desired product of this method is the preferred gimbal angles and not a benchmark for the overall mission. The formal optimization statement for off-line calculation of preferred gimbal angles is the modified version of Eq.

$$
\begin{aligned}
\text{Minimize} \quad J_{PS}(\vec{x}, \vec{u}, t) &= t_f + \alpha \sum_{k=1}^{N} \epsilon_i(k) \\
\text{where} \quad \vec{x} &= [\vec{q}, \vec{\omega}, \vec{\delta}, \dot{\vec{\delta}}] \\
\vec{u} &= \ddot{\vec{\delta}} \\
\text{Subject to} \quad \dot{\vec{x}} &= [Eq.\ 2.19,\ Eq.\ 2.16,\ \dot{\vec{\delta}},\ \vec{u}] \\
\vec{x}(t_0) &= [\vec{q}(t_0), \vec{\omega}(t_0), \text{free}, \dot{\vec{\delta}}(t_0)] \\
\vec{x}(t_f) &= [\vec{q}(t_f), \vec{\omega}(t_f), \text{free}, \text{free}] \\
\left| \dot{\vec{\delta}}(t) \right| &\leq \text{Max } \dot{\vec{\delta}} \\
\left| \ddot{\vec{\delta}}(t) \right| &\leq \text{Max } \ddot{\vec{\delta}} \\
\left| \vec{\omega}(t) \right| &\leq \text{Max } \vec{\omega}
\end{aligned}
\tag{3.28}
$$

The preferred gimbal angles calculated from the off-line pseudo-spectral optimization are captured in a look-up table. The Preferred Gimbal Angles block of the closed-loop control scheme then pulls the set of gimbal angles corresponding to the next target from the table when the current target starts collecting.

The second method for calculating preferred gimbal angles is a near-real-time sequential quadratic programming (SQP) optimization. Motivation for this method stems from the desire to calculate preferred gimbal angles for impromptu targets. The pseudo-spectral method above requires knowledge of target coordinates and order well ahead of

mission time so that preferred gimbal angles can be calculated off-line. A method is sought to run a coarse optimization on-board the spacecraft during the first few real-world seconds of collect mode which yields near-optimal gimbal angles for the next target. The remainder of the collect mode, until the dwell time is reached can then be used for null motion to rotate gimbals toward those preferred angles. Since the gains for each controller are carefully chosen to minimize overshoot, a feature of the RWCMG closed-loop control scheme is that when slewing to a new target, the pointing error remains within the desired 2-norm error tolerance after it first enters that desired range. In other words, the imager locks on to the target and stays on the target, within tolerances, for the duration of the dwell time. This feature allows the algorithm to predict spacecraft attitude and angular rate states at the end of the current collection as soon as the target is first acquired - when slew mode changes to collect mode. Predictions of attitude and angular rate at the start of the next slew are then used as the initial condition for the SQP optimization. The controls for the SQP optimization are the gimbal angles and length of time step. By hard-coding a desired number of optimization time steps N_{pd} the optimization is constrained to complete in the desired real-world time span of a few seconds using current CPU processing speeds. The formal SQP problem statement is

$$
\begin{aligned}
\text{Minimize} \quad J_{\mathrm{SQP}}(\vec{x}, \vec{u}, t) \quad &= \quad t_f + \alpha_1 \sum_{k=1}^{N_{pd}} Ea\Delta + \alpha_2 \sum_{k=1}^{N_{pd}} \omega\Delta \\
\text{where} \quad \vec{x} \quad &= \quad [\vec{q}, \vec{\omega}] \\
\vec{u} \quad &= \quad [\vec{\delta}, ts_{\mathrm{opt}}] \\
\text{Subject to} \quad \dot{\vec{x}} \quad &= \quad \text{EOM} \\
\vec{x}(t_0) \quad &= \quad [\vec{q}(t_{\mathrm{slew}}), \vec{\omega}(t_{\mathrm{slew}})] \\
\vec{x}(t_f) \quad &= \quad [\text{free}, \text{free}]
\end{aligned}
\tag{3.29}
$$

The t_f aspect of J_{sqp} is calculated as the product of the optimization time step duration ts_{opt} and number of time steps N_{pd}. Similar to the previous optimizations, the Euler angle error term is needed to ensure the state trajectory tracks the target. The angular rate error term

75

is added to the SQP optimization to increase accuracy. Euler angle and angular rate error term definitions are

$$
\mathrm{Ea}\Delta = \sum_{1}^{N_{pd}} \left\| Ea_{opt} - Ea_{com} \right\|_2
$$

$$
\omega\Delta = \sum_{1}^{N_{pd}} \left\| \omega_{opt} - \omega_{com} \right\|_2
$$

(3.30)

where Ea_{opt} are the Euler angles found by the optimizer (converted from quaternion states), Ea_{com} are the commanded Euler angles found from trigonometry based on the current s/c state, ω_{opt} are the s/c angular rates found by the optimizer, and ω_{com} are the commanded s/c angular rates.

The third method of determining preferred gimbal angles is to set the preferred angles as the Vadali angles discussed in Section 2.8. Vadali determined that the gimbal angles $[45°, -45°, 45°, -45°]^T$ provided singularity-free torque for any simple command except a pure z-axis torque [2]. When the Vadali preferred gimbal angle option is chosen for the RWCMG closed-loop control scheme, the Preferred Gimbal Angles block outputs $\pm 45°$ alternating as the preferred gimbal angles.

On the occasions when the Preferred Gimbal Angles block is called, it is the last step in the closed-loop control scheme. Otherwise, the Mission Progress block is the final block before the next time step starts. The simulation then starts back at the Calculate Parameters block for the next time step. The simulation continues until all targets have been imaged for their respective dwell times then commands the satellite to return to a zero attitude for the remainder of the total simulation time. This completes the Closed-Loop Control Scheme section. Attention is now given to converting the analytical simulation to a hardware experiment.

3.3 Hardware Model Closed-Loop Control Scheme

In Section 3.2 the closed-loop control scheme is presented as implemented in the analytical model. When implementing the RWCMG system on the AFIT SimSat hardware

platform some modifications to the analytical closed-loop control scheme are necessary. In addition, a discovery with regards to CMG null motion spurred a modification to the null motion equation which improves performance.

3.3.1 Conversion of Analytical Code to SimSat Platform.

As discussed earlier, the first step taken was to implement the analytical closed-loop control scheme of Figure 3.1 in numerical simulation. When transferring the model to the AFIT SimSat hardware, some fundamental changes to the closed-loop control scheme are necessary and are discussed next. The first change is to remove the Limit Enforcement block because it is no longer necessary. The SimSat hardware including air bearing, actuators, and sensors have limits due to the real physical constraints. The simulated properties of Figure 3.1 are all constrained by physical limitations of SimSat. If a gimbal rate command greater than 2.5 rad/s is sent to a CMG driver, the gimbal is only allowed to spin at 2.5 rad/s.

The next difference between the analytical and experimental closed-loop control scheme is that the Steering Law/Null Motion block no longer is responsible for calculating attitude rate, spacecraft angular rate, CMG acceleration, reaction wheel acceleration, and reaction wheel jerk. The hardware drivers for the CMG pyramid require gimbal rates, and the hardware drivers for the reaction wheel array require a torque vector. CMG gimbal rates are already calculated by the Steering Law/Null Motion block in the analytical closed-loop control scheme. However the analytical dynamics calculate reaction wheel acceleration instead of torque. A modification to the Steering Law/Null Motion block of the hardware model compensates for this difference by using the upper left 3x3 portion of the weighting matrix W by the controller-generated $\vec{\dot{h}}_{\mathrm{act}}$. The upper left portion of W corresponds to the reaction wheel actuators and ensures that the correct proportion of the total control torque goes to the reaction wheels during the transition period from slew mode to collect mode. After the transition period, when the reaction wheels have complete control of the

spacecraft, all of the control torque $\dot{\vec{h}}_{\text{act}}$ goes to the reaction wheel drivers as the CMG pyramid is controlled by the null motion steering equations.

Instead of the Steering Law/Null Motion block calculating quaternion differentials for attitude rates and Euler's equations for spacecraft accelerations, spacecraft body rates are estimated from onboard IMU measurements at a user-specified rate. Quaternions are calculated from these body rate estimates. Gimbal angles and reaction wheel rates are also measured with onboard sensors. Thus a standalone measurement block is inserted into the hardware closed-loop control scheme which provides the state updates instead of that set of parameters being generated analytically.

Though planned for the future, the current SimSat hardware does not contain a means for external dynamic capture of attitude or rate measurements. Therefore, the filtering algorithms explored in the analytical model are left as future work for the hardware experiment. McChesney previously installed a low-pass filter on SimSat which reduces IMU error [32]. This low-pass filter is used for the current RWCMG research and is discussed further in Section 4.4.

The final difference between the analytical and experimental closed-loop control scheme is the absence of the SQP method from the experimental Preferred Gimbal Angles block. Simultaneous real-time spacecraft control and on-board processing of the SQP algorithm is not implemented in hardware experiments but is listed in Chapter V as a topic for future work. The closed-loop control scheme as modified for hardware experimentation is shown in Figure 3.4

3.3.2 *Shortest-Path CMG Gimbal Null Motion.*

When using the hardware version of the closed-loop control scheme, an observation is made concerning CMG gimbal null motion. Eq. (3.21) contains the term $(\vec{\delta} - \vec{\delta}_{\text{pd}})$ which provides the vector direction for the gimbals to travel in their respective null motion trajectories. The observation discovered through hardware experimentation is that this
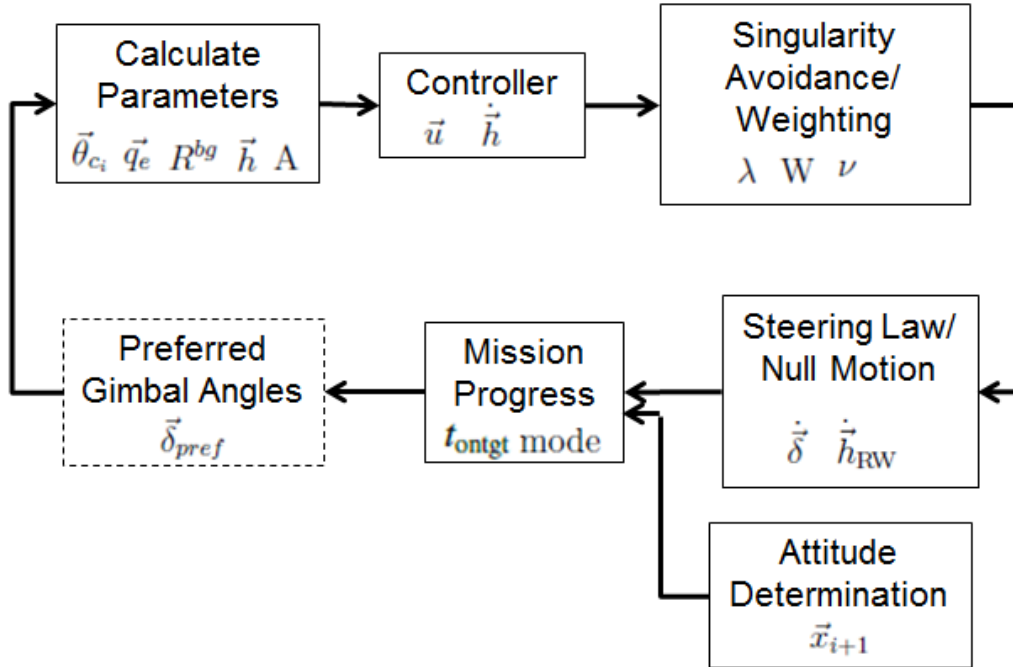
Figure 3.4: Hardware Model Closed-Loop Control Scheme

direction term of the null motion equation did not always send the gimbals along the shortest path to the preferred gimbal angles. As demonstrated in Figure 3.5, a gimbal currently located at 45° and seeking a preferred gimbal angle of 315° travels in a positive direction (red arrow) across a span of 270°, while a path in the opposite direction (blue arrow) only requires a 90° shift. To ensure gimbal null motion takes the most expedient path toward preferred gimbal angles, logic is added to the hardware version of the Steering Law/Null motion block to compare the current orientation of each gimbal to the respective preferred value and determine the shortest path $\vec{\delta}_{sp}$. First, the current gimbal angles and preferred gimbal angles are conditioned to values between 0° and 360° so all calculations are made with consistent relations. Next, a series of logic assessments determines the shortest path from each gimbal's current position d_i to the preferred gimbal angles pd_i and is represented in the following statements:

- If $d_i > pd_i$

- If $d_i - pd_i > 180°$

$$\delta_{sp_i} = d_i + pd_i$$

- Else

$$\delta_{sp_i} = d_i - pd_i$$

- Else

  - If $pd_i > 180°$

$$\delta_{sp_i} = d_i + pd_i - 360°$$

  - Else

$$\delta_{sp_i} = pd_i - d_i$$

The logic as implemented in MATLAB® Simulink is shown in Figure 3.6. Null motion steering law, Eq. (3.21), is now modified with the shortest path directional vector $\vec{\delta}_{sp}$

$$
\begin{bmatrix} \dot{\delta}_1 \\ \dot{\delta}_2 \\ \dot{\delta}_3 \\ \dot{\delta}_4 \end{bmatrix} = k(A_c^T (A_c A_c^T)^{-1} A_c - I_{4x4})(\vec{\delta}_{sp}). \tag{3.31}
$$

Use of the shortest path directional vectors results in calculation of gimbal rates $\vec{\delta}$ which still reside in the torque null space and ensures gimbals travel a minimum distance to get least-squares-close to preferred values. The discovery and development of the shortest path algorithm for CMG gimbal null motion is the final step in conversion of the analytical model to the hardware experiment. The next section introduces the methods used in assessing simulation and experiment performance. Specific metrics used in model assessments are introduced at the beginning of Chapter IV.

3.4   Means of Assessing Simulation Performance

With the analytical and experimental closed-loop control schemes explained, attention now turns to assessment of the RWCMG system performance. The first aspect of the RWCMG system to evaluate is controller selection. The three controllers (PID, QF, and LB) of Sections 2.4 and 3.2.2 are modeled both in numerical and experimental simulation. One means of assessing controller performance is to study each controller's capability for tracking targets. Figure 1.1, the representative target field, shows the first target is a simple slew in one axis, and the remaining targets require alternating slews of one axis while countering the orbital velocity with a second axis. A plot of spacecraft Euler angles versus time while performing this representative mission affords valuable insight into controller performance. An example Euler angle versus time plot of the RWCMG simulation using the PID controller is shown in Figure 3.7 in order to introduce the reader to this means of assessment. Figure 3.7 shows the performance of the PID controller through the motion of the three spacecraft axes. Commanded Euler angles are shown in a dashed line and actual motion of the spacecraft is a solid line. Spacecraft axis one, in black, is commanded to a constant zero degrees for the representative mission. The spacecraft does not need to rotate in the yaw axis to image the targets. Axis two, in red, can be thought of as the roll axis and is shown to sweep side-to-side as the representative target field dictates. Spacecraft axis three, in blue, can be thought of as the pitch axis as the spacecraft flies over the target field. Due to the assumed constant orbital velocity magnitude of the spacecraft as it passes over the target field, the targets are dynamic in the spacecraft 3-axis. The PID controller is used to introduce the Euler Angle vs Time plot because the pointing error level allows the reader to see the dashed lines representing the desired angles. Another feature of the attitude plot of Figure 3.7 is the background shading to show the mode. In terms of evaluating controllers, specific parameters such as overshoot, settling time, and pointing error can be

discerned from study of Euler angle plots. Plots of Euler angles versus time are used in Chapter IV. Specific metrics pulled from the plot will be discussed in Section 3.5.

Associated with the Euler angle versus time plot of Figure 3.7, a plot of pointing angle error versus time helps visualize the slew and collect phases of the RWCMG mission. A sample pointing error plot is shown in Figure 3.8 for the same PID controlled hardware experiment which created the Euler angle plot above. The value of the pointing angle in Figure 3.8 is the 2-norm of commanded Euler angles versus achieved Euler angles at each time step and is shown in Eq. (3.2). The dashed line in Figure 3.8 is the desired pointing error requirement for the model to switch from slew mode to collect mode. When the pointing error is less than the pointing requirement - two degrees for the RWCMG application - then collection on the current target proceeds. Shading on the pointing error plot also delineates slew mode from collect mode and corresponds to the same shading on the Euler angle plot. The focus of the RWCMG research conducted for this dissertation is on implementation of the analytical and hardware closed-loop control scheme. A rigorous evaluation of controller accuracy is not a focus area, thus the two degree pointing tolerance is deemed adequate to evaluate the RWCMG performance.

The evaluation of the Limit Enforcement block of the analytical closed-loop control scheme is also a subject of discussion in Chapter IV. Plots of each parameter which is limited by the algorithm show how well the Limit Enforcement block performs. Comparison of parameter plots to output of the hardware simulator will also reveal insights.

The third means of assessing simulation performance is to examine how well the null motion performed - both in the analytical simulation and in the hardware experiment. Plots of gimbal angles versus time as the models perform the representative mission will show how close each gimbal came to achieving the preferred value. Simulation metrics such as overall mission time, singularity avoidance parameters, and disturbance torque assessments will quantify the performance of the null motion toward preferred gimbal

angles. Comparison of the RWCMG system to the traditional CSCMG system will be made in order to relate the benefits of adding extra actuators to the spacecraft.

The fourth means of evaluating the simulation performance is to study results of the analytical application of the EKF and UKF. A Monte Carlo analysis of each filter will allow a statistical ranking of metrics such as mean ensemble error, root sum square error, and standard deviation. Each of these metrics will be explained further in Section 3.5.

Finally, RWCMG simulations will be evaluated based on the ability to avoid singularities. Runs of the representative mission starting at gimbal angles which are poor in terms of avoiding singularities will show how well the RWCMG system performs as compared to the traditional CSCMG system. Each of the preferred gimbal angle calculation methods will be compared in terms of singularity analysis, as well as each controller. Experiments with differing initial gimbal angles are used to compare RWCMG performance to SGCMG performance when starting the mission in conditions near a singularity.

3.5   Evaluation Metrics Defined

Section 3.4 explains the means of assessing performance for the RWCMG models. Specific metrics derived from these means are now explained.   When conducting an agile spacecraft imaging mission, one of the most important aspects of operation is accomplishing mission sets in the fastest time possible and meeting all constraints. Shorter slews and collection phases mean more collections can occur over the lifetime of the spacecraft.   Therefore, the first metric used to evaluate performance of the RWCMG mission is the completion time for the representative mission.   Completion time can be seen in Euler angle plots such as Figure 3.7 where the background shading changes from gray to white - when the dwell time for target four has been met at time 141.1 seconds.

In addition to completion time, pointing error needs to be addressed when evaluating performance of the RWCMG system. Pointing error plots, such as Figure 3.8, provide a

visual means for assessing mission progress but do not quantify pointing error in a way to make numerical assessment. Thus the next metrics used in assessing RWCMG performance are total root sum square (RSS) error and total root mean square (RMS) error. Total RSS error is

$$\text{RSS}_{\text{Ttl Err}} = \sqrt{\sum_{i=1}^{N_{\text{ts}_c}} \epsilon_i^2} \tag{3.32}$$

and total RMS error is

$$\text{RMS}_{\text{Ttl Err}} = \sqrt{\frac{\sum_{i=1}^{N_{\text{ts}_c}} \epsilon_i^2}{N_{\text{ts}_c}}}. \tag{3.33}$$

The term N_{ts_c} is the number of time steps during collect mode and ϵ_i is the pointing error of Eq. (3.2). Total RSS and RMS errors are closely related but differ in that total RMS divides by the number of samples. Thus RMS focuses more on the accuracy of pointing versus the RSS which gives a measure of the length of settling time for a collection. Total RSS and RMS are limited in application to the collect phase because pointing accuracy during the slew mode is not an emphasis of an imagery mission.

The next set of metrics used in evaluating RWCMG performance pertain to singularity analysis. Sections 2.3 and 2.5 introduced the reader to ν and ς singularity parameters, respectively. These normalized metrics indicate the CMG array is at singularity when they have a value of zero. An example singularity plot for the PID RWCMG analytical simulation with no null motion (the same case as shown in Figures 3.7 and 3.8) is shown in Figure 3.9. The horizontal dashed line drawn on Figure 3.9 at the value 0.03 is a selected threshold for determining a near-singularity. The black dashed line of Figure 3.9 is the ν singularity measure of Eq. (2.29), and the red dashed line is the ς measure of Eq. (2.40). Note in the example singularity measure plot of Figure 3.9 the ν measure drops below the established threshold for two time steps at approximately 112 seconds. The number of times the ν parameter drops below this threshold for a given simulation is the fourth metric for evaluating RWCMG performance. This fourth metric is useful for RWCMG research

84

because one simulation revealed an instance where the system was run without null motion and the gimbals happened to stop in a near-singular condition during one collection phase. At the end of the transition period, the RWA had taken full control of the s/c, and the CMG gimbals were stopped at their current angles - which happened to be near a singularity. In this case, the fourth metric recorded the number of time steps in a near singularity to be in the hundreds. Observing this outlier value compared to typical numbers of near singularities in range of 1 to 20, gave an indication that that particular run required further examination. The average value of ν across the entire simulation is a second singularity-related metric and the fifth overall metric used in Chapter IV. This fifth metric gives an indication of the overall stability of the run. The lower the average ν, the closer the mission is operating to singularities. One goal of the RWCMG system is increase the average ν. The five metrics explained in this section are shown in Table 3.2 for clarity.

Table 3.2: Metrics Used for RWCMG Performance Evaluations

Completion Time (sec)
Total RSS Error (deg)
Total RMS Error (deg)
Number of Near-Singularities
Average Singularity Measure

This concludes Chapter III. The next chapter uses the means and metrics explained in this section to evaluate RWCMG performance with respect to controller selection, preferred gimbal angle calculation method, initial s/c gimbal angle, and overall actuator systems. An evaluation of the limit enforcement algorithm and stochastic estimation methods is also given for the analytical simulation.
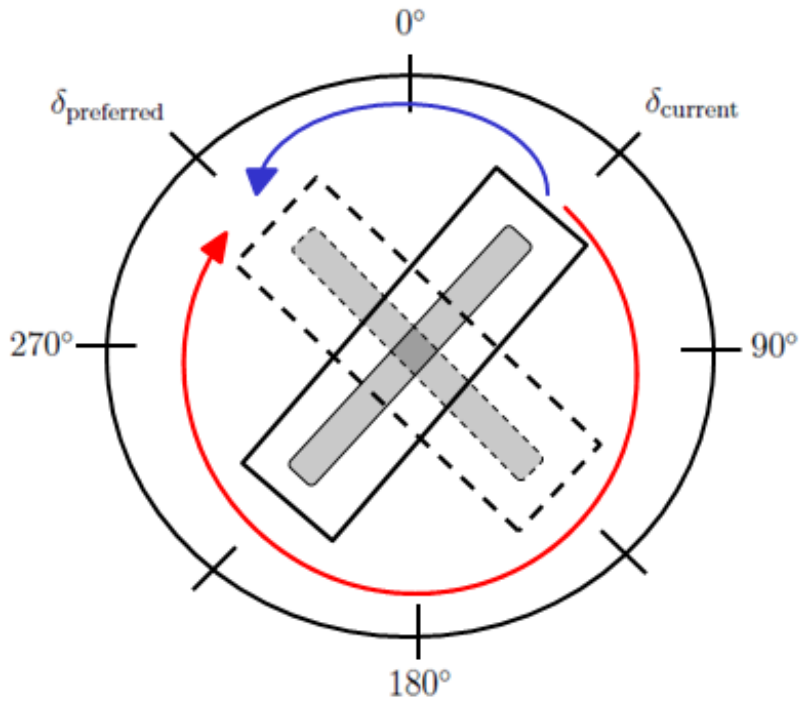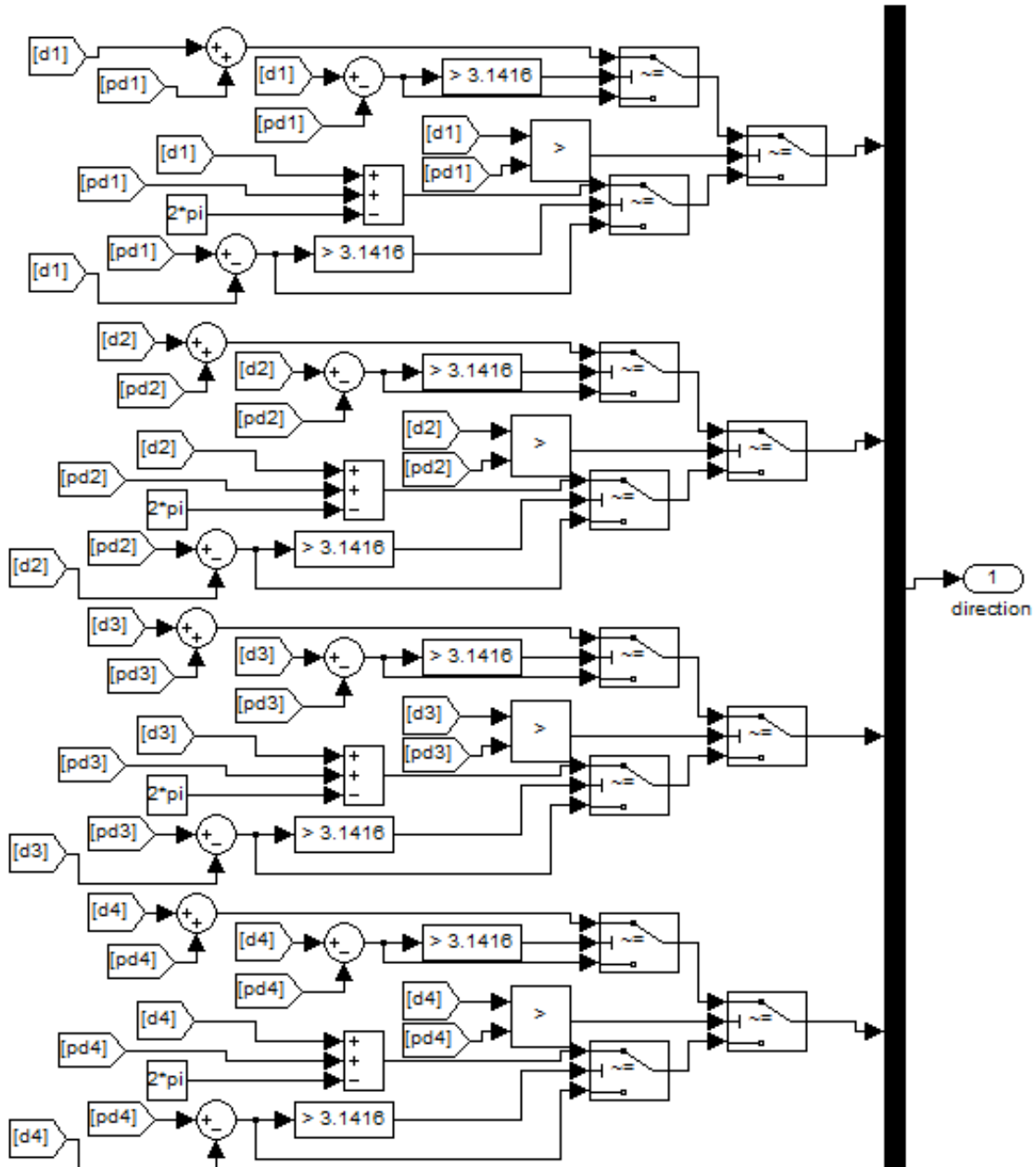
Figure 3.5: Gimbal Angle Shortest Path Illustration
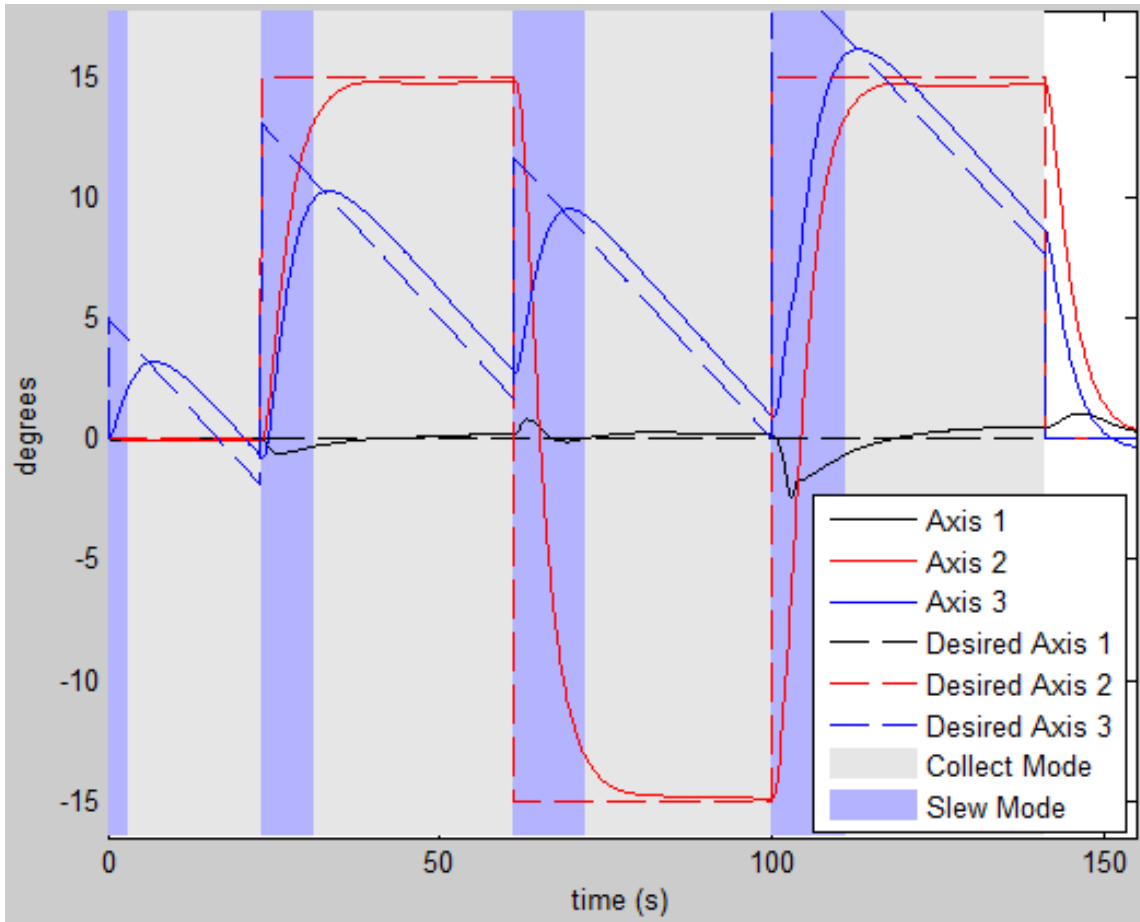
Figure 3.6: CMG Gimbal Shortest Path Logic

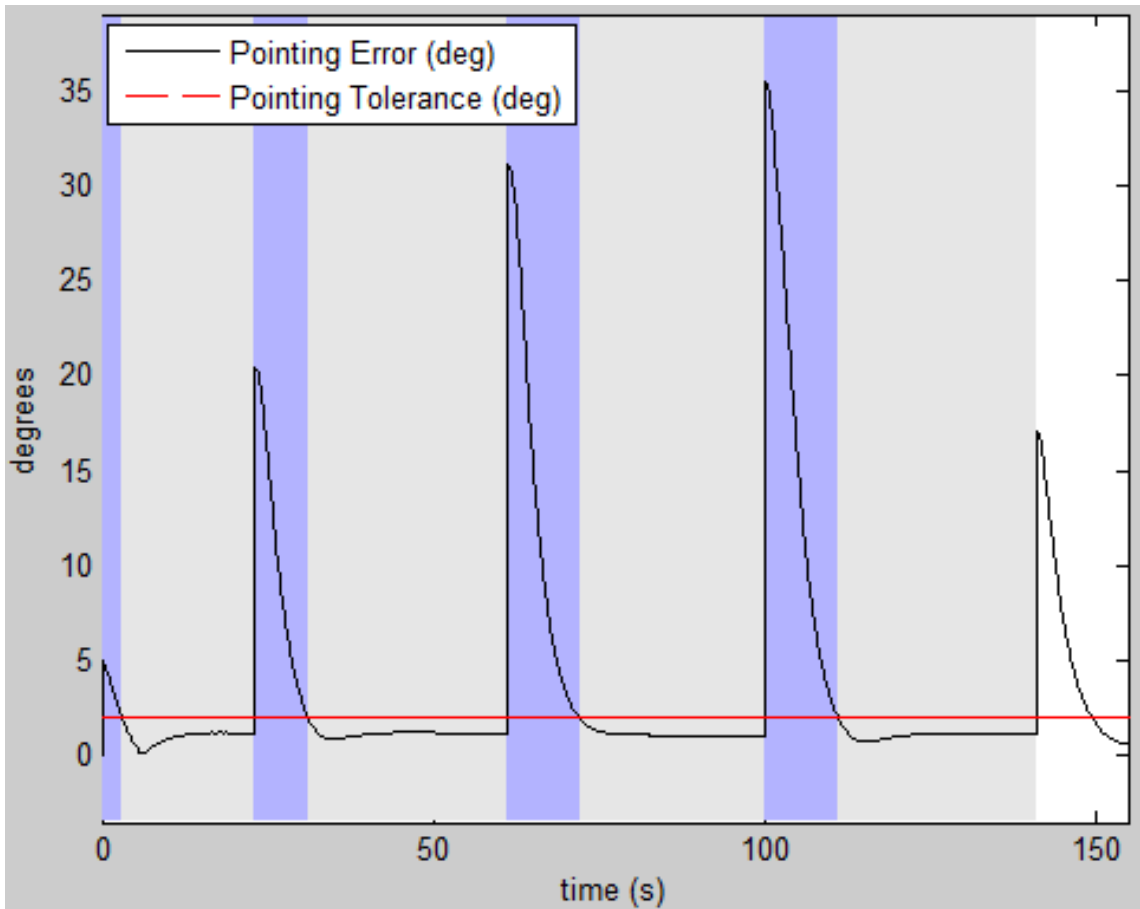Figure 3.7: Sample Euler Angle vs. Time Plot for RWCMG Mission Using PID Controller

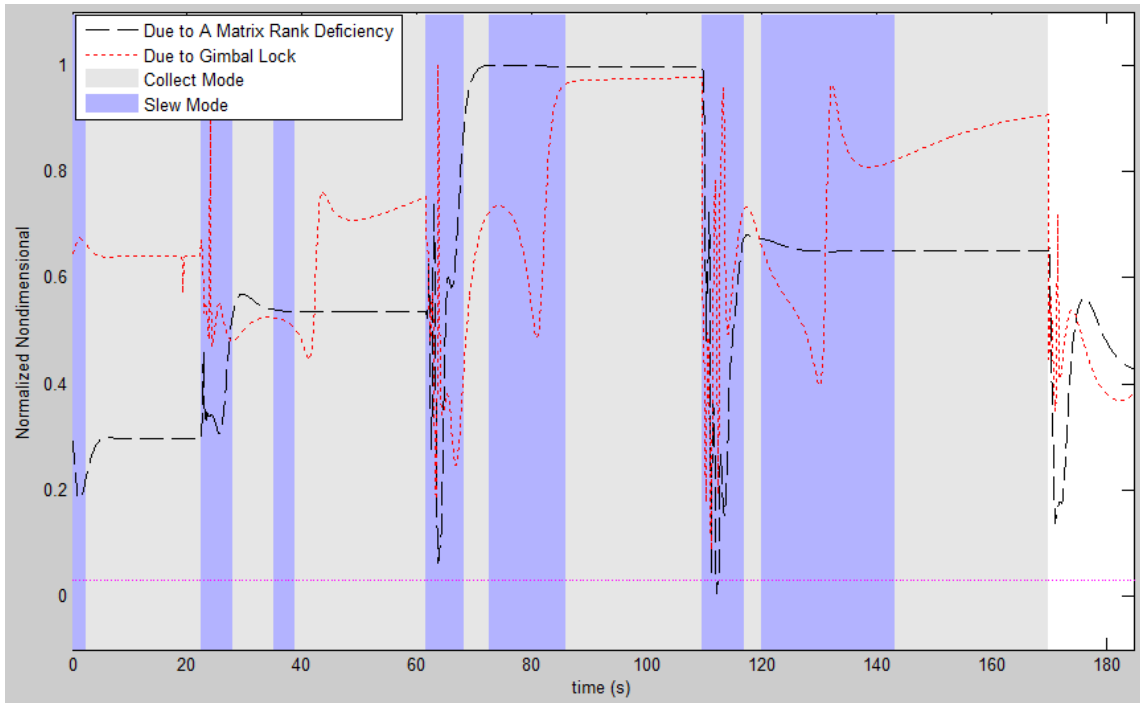Figure 3.8: Sample Pointing Accuracy vs. Time Plot for RWCMG Mission Using PID Controller

Figure 3.9: PID Singularity Metrics vs. Time

IV. Results and Discussion

Chapters I and III described the RWCMG representative mission and closed-loop control schemes for analytical and experimental simulation models. Chapter III explained the means and metrics for assessing simulation performance. In Chapter IV, the results of implementing the RWCMG methods of Chapter III are presented and analyzed. This chapter starts with an evaluation of the controllers introduced in Chapters II and III for the analytical and experimental simulations. The performance of the Limit Enforcement block of the analytical closed-loop control scheme is discussed next. Evaluation of the RWCMG system to perform null motion of the gimbals toward preferred angles follows. Consideration for the off-line pseudo-spectral, near-real-time SQP, and Vadali [2] preferred gimbal angle methods is given for analytical model null motion. Offline pseudo-spectral and Vadali methods are applied and are evaluated for the experimental simulation. Finally, the EKF and UKF stochastic estimation techniques are evaluated using the analytical model. Discussions of the results are contained within each section. Final research conclusions are presented in Chapter V.

4.1   Controller Evaluation

Evaluation metrics explained in Section 3.5 are now used to evaluate the controllers introduced in Chapters II and III: the proportional integral derivative (PID), the quaternion feedback (QF), and the nonlinear Lyapunov-based (LB) controllers. All three controllers are tested for the RWCMG mission on the analytical model and on the hardware experiment. A combination of the QF and LB controllers is also explored in both environments. Since the QF controller was designed for rest-to-rest maneuvers, and the LB controller was designed with a nonlinear term for dynamic target performance, the

combined QF and LB (CB) controller is tested in an attempt to exploit the strengths of each controller.

4.1.1 Analytical Results.

In order to evaluate performance of the three controllers for the analytical closed-loop control scheme of the RWCMG system, the problem setup needs to first be addressed. The initial state of the spacecraft for the controller evaluation is a near-zero Euler angle set (converted to quaternions) and near zero angular velocity. Near zero, in this instance, means numbers on the order of 1×10^{-9}. The attitude and spacecraft angular rate are meant to be at zero degrees and radians per second, respectively; however, the near zero numbers avoid mathematical difficulties in the software. An example of the mathematical difficulties is found by recalling the calculations for the QF controller gain in Eq. (2.35). The computations for the parameter k_i involve dividing by the initial quaternion states. If the initial attitude is exactly $[0°, 0°, 0°]$ then the initial quaternion is $[0, 0, 0, 1]$ and the k_i equations result in divide by zero errors. CMG rotor rates are set to a constant rate of 2600 rpm. Initial gimbal angles are set to the Vadali [2] values: $[45°, -45°, 45°, -45°]$. Reaction wheels are at near zero angular velocity and acceleration rates at the start of the simulations.

The three controllers are used to conduct the representative RWCMG mission of Fig. 1.1. Since null motion is not conducted for the controller evaluation, no preferred gimbal angles are sought. All controller gains are adjusted for damping ratio and natural frequency parameters as described in Section 2.4. The limit enforcement algorithm as described in Section 3.2.4 is active for the analytical controller evaluation in order to produce results closer to values observed during hardware experiments. Further discussion of the limit enforcement algorithm is found in Section 4.2 below. Euler angle versus time plots placed next to their corresponding pointing error plots for each of the three controllers performing the RWCMG mission are shown in Figures 4.1 through 4.3 to motivate the discussion that follows.
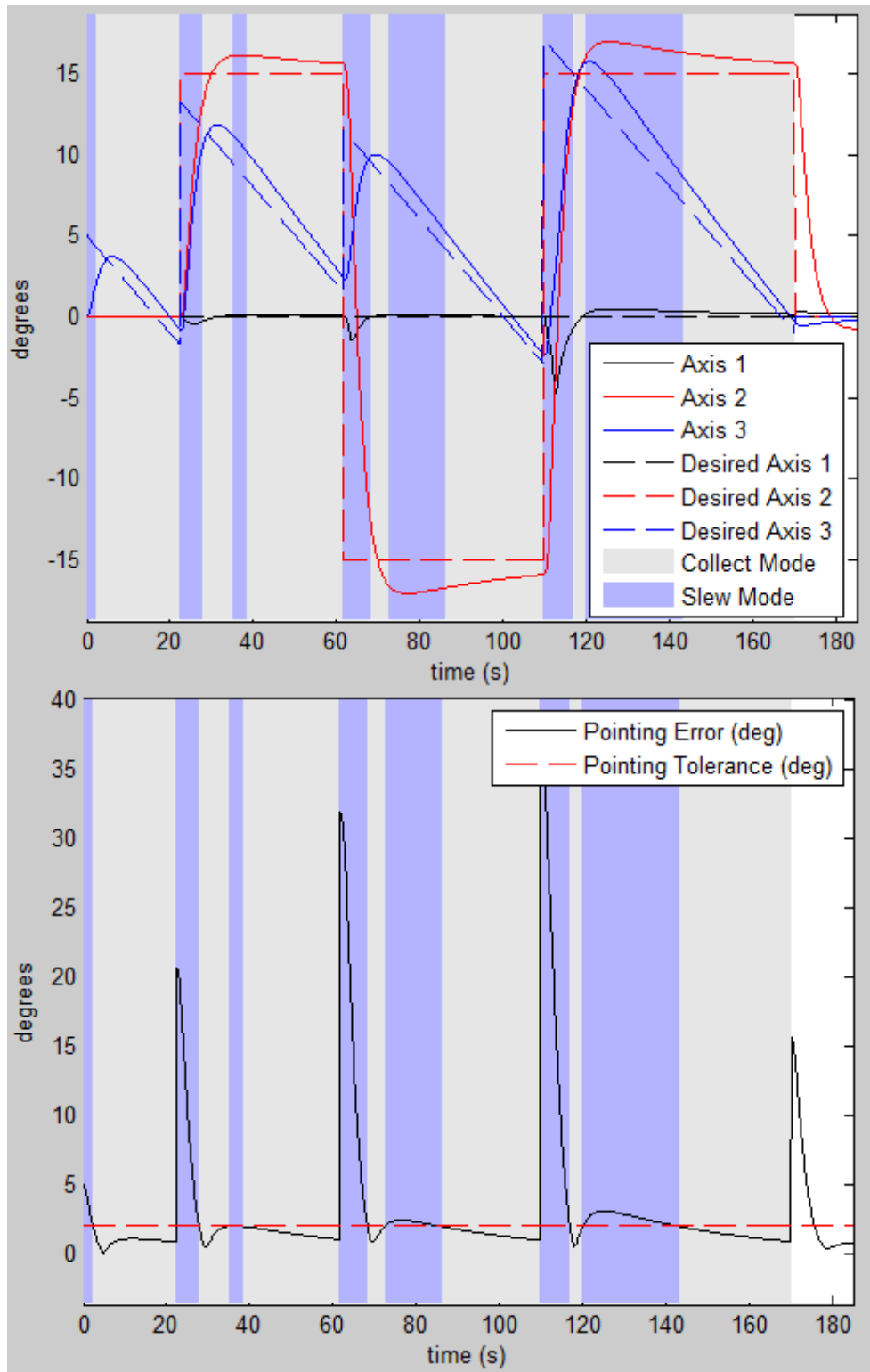
Figure 4.1: PID Euler Angles vs. Time (top) and Pointing Error vs. Time (bottom) - Analytical Simulation
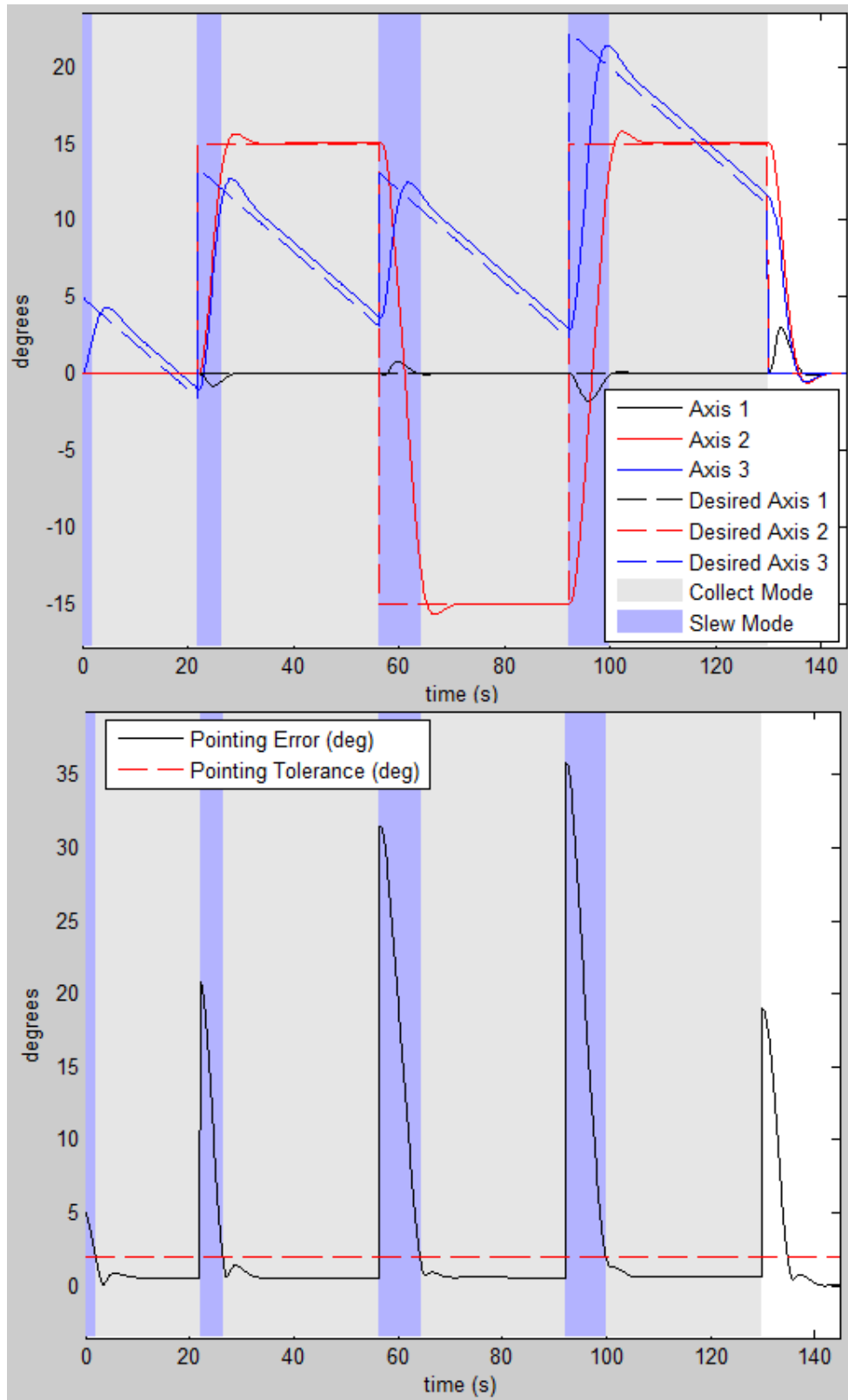
Figure 4.2: QF Euler Angles vs. Time (top) and Pointing Error vs. Time (bottom) - Analytical Simulation
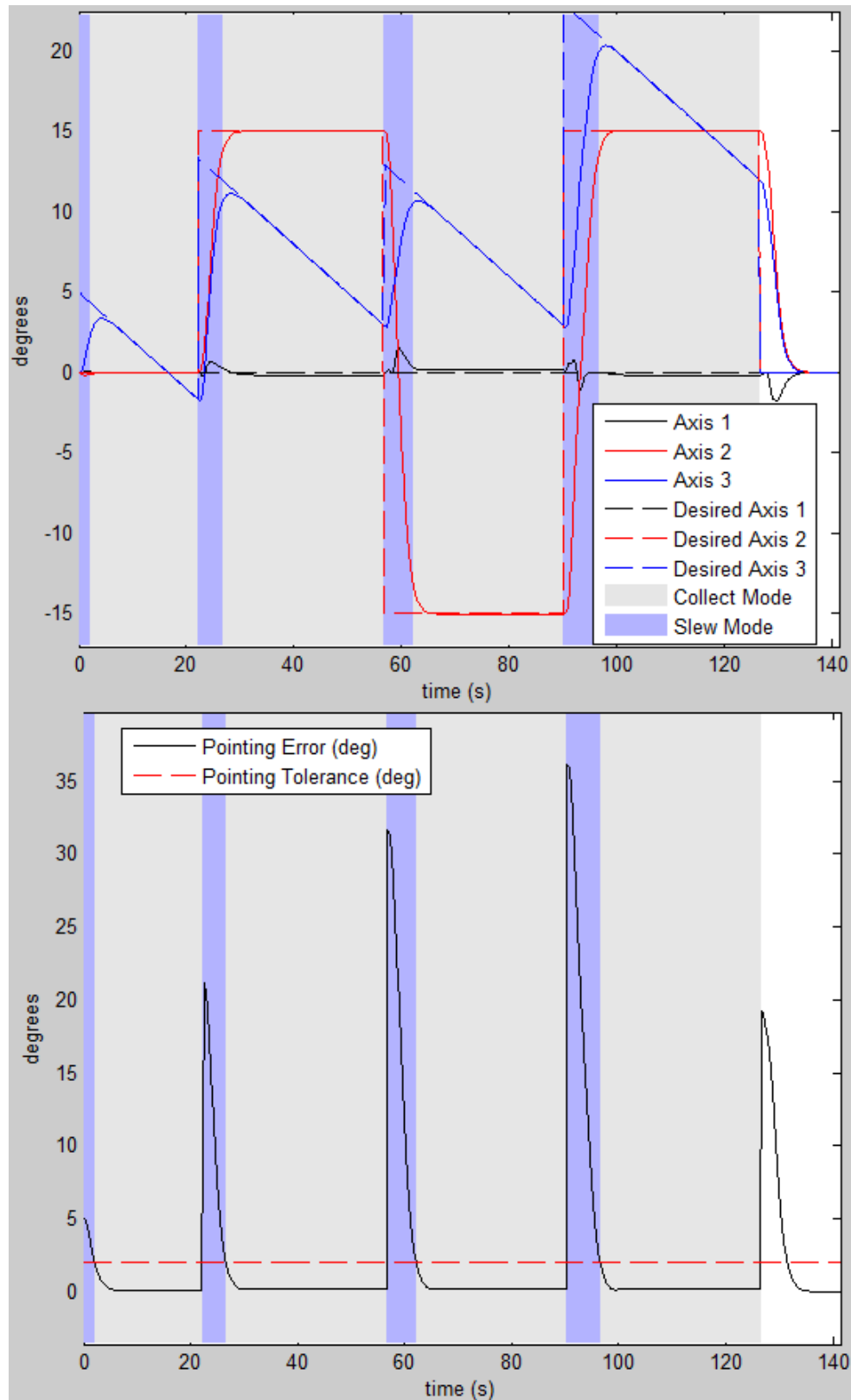
Figure 4.3: LB Euler Angles vs. Time (top) and Pointing Error vs. Time (bottom) - Analytical Simulation

95

Table 4.1: Comparison of Controllers for the RWCMG Mission - Analytical Simulation (with Limits Enforced)

	PID	QF	LB	CB
Completion Time (sec)	169.8	129.9	126.5	131.3
Total RSS Error (deg)	47.33	23.26	10.79	11.72
Total RMS Error (deg)	1.04	0.467	0.215	0.236
Number of Near-Singularities	2	1	18	4
Average Singularity Measure	0.625	0.619	0.518	0.556

Overall, the PID controller struggles to settle on the commanded Euler angles after the relatively large angle slews of the RWCMG representative mission. As seen in Figure 4.1, the PID-controlled satellite enters slew mode for target two at approximately 28 seconds. But due to a large overshoot, temporarily exits the two degree pointing accuracy requirement and re-enters slew mode. This behavior repeats when slewing to targets three and four. The associated PID pointing accuracy plot adjacent to the Euler angle plot shows the violations of the accuracy requirement over time. Recall from Section 3.2.8 that the SQP method of calculating preferred gimbal angles requires the satellite to maintain pointing accuracy standards once first achieved in order to predict initial conditions for the optimization. Therefore the PID controller is insufficient for the RWCMG mission with SQP gimbal angle optimization. Another observation evident from Figure 4.1 is the amount of time required to complete the mission: 169.8 seconds. The other controllers complete the mission at least 23% faster. Due to the high overshoot violations of pointing accuracy the collection phases of the PID RWCMG mission are interrupted and thus required longer to complete. Collection on each target proceeds during any portions of the mission in which the pointing tolerance requirement is met, even if later interrupted. In other words,

the simulation does not require dwell times to be accomplished uninterrupted. Had the requirement been for continuous collection without interruption the PID RWCMG mission would have a much larger final time. While pointing error meets the stated two degree 2-norm error tolerance during collection phases the relatively long settling time of the PID controller results in higher pointing error statistics than the other controllers. Error statistics for the PID controller are included in Table 4.1. The PID-controlled RWCMG mission only encountered a near-singular condition during two time steps in the simulation. Singularity statistics are also included in Table 4.1, but are fairly benign since the gimbal angles are started at the Vadali [2] angles for the controller evaluation. Singularity statistics will become more important in the evaluation of null motion and preferred gimbal angles in Section 4.3.

Transitioning now to the QF controller simulation of Figure 4.2, a measurable improvement is noticed when comparing to the PID simulation. Recall from Section 2.4 that the QF controller was designed for large angle, minimum time eigenaxis maneuvers [27]. Despite a small overshoot, the QF controller maintains pointing accuracy requirements for the entire dwell time for each target after first entering collect mode. Therefore, the QF controller is viable for all preferred gimbal angle calculation methods. The final time for collection of all four targets with the QF controller in this simulation set is 129.9 seconds, 40 seconds faster than the PID-controlled simulation. Total RSS error is 50% lower during the QF-controlled simulation compared to the PID controller simulation; however a constant steady-state error is notable in the dynamic s/c axis three. Recall from Section 2.4 that the QF controller is designed for rest-to-rest maneuvers since Wie did not treat the case of moving targets [27]. The dynamic term in the equations of motion is neglected with the QF controller. Thus the QF controller performs better for spacecraft axes one and two which remain static during collection, but suffers a steady state lag when tracking the dynamic axis three. The QF controller only encountered a near-singularity on

97

one time step of the simulation. Error and singularity statistics for the QF controller are included in Table 4.1 and are in the same general range as the PID-controlled simulation.

Moving on now to the LB controller simulation of Figure 4.3, another incremental improvement is noticeable. Recall from Section 2.4 that the LB controller contains terms which treat the nonlinear equations of motion and a summation term which allows the engineer to specify a desired s/c angular rate trajectory. Looking at times 30 seconds, 65 seconds, and 100 seconds, virtually zero overshoot is observed with this application of the LB controller. Like the QF controller, the LB controller does not exit collect mode, once started, until the dwell time for each target is met. The final time for the LB controller simulation is 126.5 seconds, 3.4 seconds faster than the QF controller. Since both QF and LB controllers maintained continuous dwell times, the 3.4 second improvement of the LB controller is due to faster slew times. Also improved with the LB controller is tracking of the dynamic spacecraft axis three. Total RSS error for the LB-controlled simulation is 53% lower than that of the QF-controlled simulation and 77% lower than the PID-controlled simulation. A relatively large number of near-singularities are encountered in the LB controller run compared to the other controllers, however. The cause for the higher number of near-singularities with the LB-controlled simulation is the fact that the gimbal angles are being commanded to change at a higher rate than for the QF-controlled simulation. Since the CMG gimbal angles change at a faster rate for the LB-controlled simulation than the QF-controlled simulation, the probability of encountering singularities also increases. Figure 4.4 shows the gimbal rate versus time for the QF and LB-controlled simulations run to generate the results in Figs. 4.2 and 4.3 respectively.

Since the QF controller is designed for rest-to-rest maneuvers between static axes and the LB controller is designed for dynamic axes, a fourth controller which uses the QF controller for spacecraft axes one and two and the LB controller for axis three is also implemented in the RWCMG simulation for assessment. The goal with the combined QF
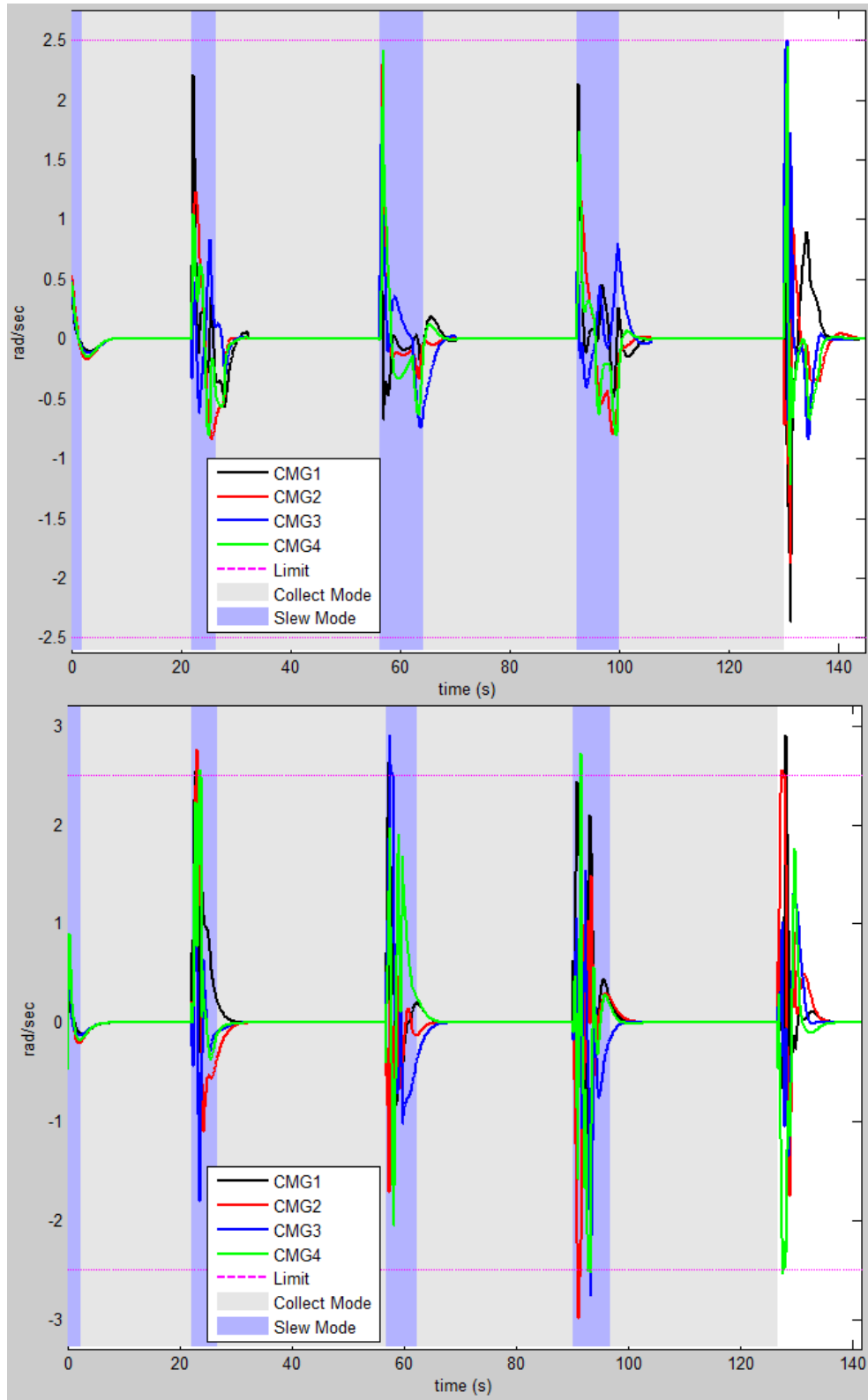
Figure 4.4: CMG Gimbal Rates vs. Time for QF Controlled Simulation (top) and LB Controlled Simulation (bottom) - Analytical Simulation

and LB (CB) controller is to use the best components of the QF and LB controllers to improve evaluation metrics. To the knowledge of the author, the CB controller has not been tested previously in the literature and the evaluation of which is considered a contribution of the current research. A simulation of the same RWCMG mission using the CB controller is depicted in Figure 4.5. While the CB-controlled simulation closely resembles the QF for axes one and two and the LB-controlled simulation for axis three, the final time using the CB controller is 131.3 seconds - 4.8 seconds slower than the LB mission. Total RSS error for the CB-controlled simulation is 49% lower than the QF-controlled simulation but 9% worse than the LB controller. The number of near singularities for the CB-controlled simulation is 4, compared to 18 with the LB controller. Metrics for the CB-controlled simulation are included in Table 4.1.

While the LB does experience a larger number of near-singular conditions than the other controllers while performing the RWCMG mission, it also completes the mission with the fastest final time. The LB controller also produces the smallest pointing error statistics. Results of all four controller evaluations for the hardware closed-loop control scheme now follow.

4.1.2 Experimental Results.

The hardware closed-loop control scheme controller evaluation experiments mirrors that of the analytical simulation with one exception. As stated in Section 3.1.2, the SimSat hardware configuration limits slew in the X and Y axes to ±25°. Therefore the 'downward-looking' b_1 axis of Figure 1.1 is the SimSat X axis. The dynamic b_3 axis corresponds to the SimSat Z axis and the 'side-to-side' slewing b_2 axis is the SimSat Y axis. This configuration results in plots with the same axis configuration as the analytical simulations, but SimSat is essentially imaging the wall instead of the floor in order to avoid hardware collisions of the air bearing and frame. All state initial conditions are exactly the same
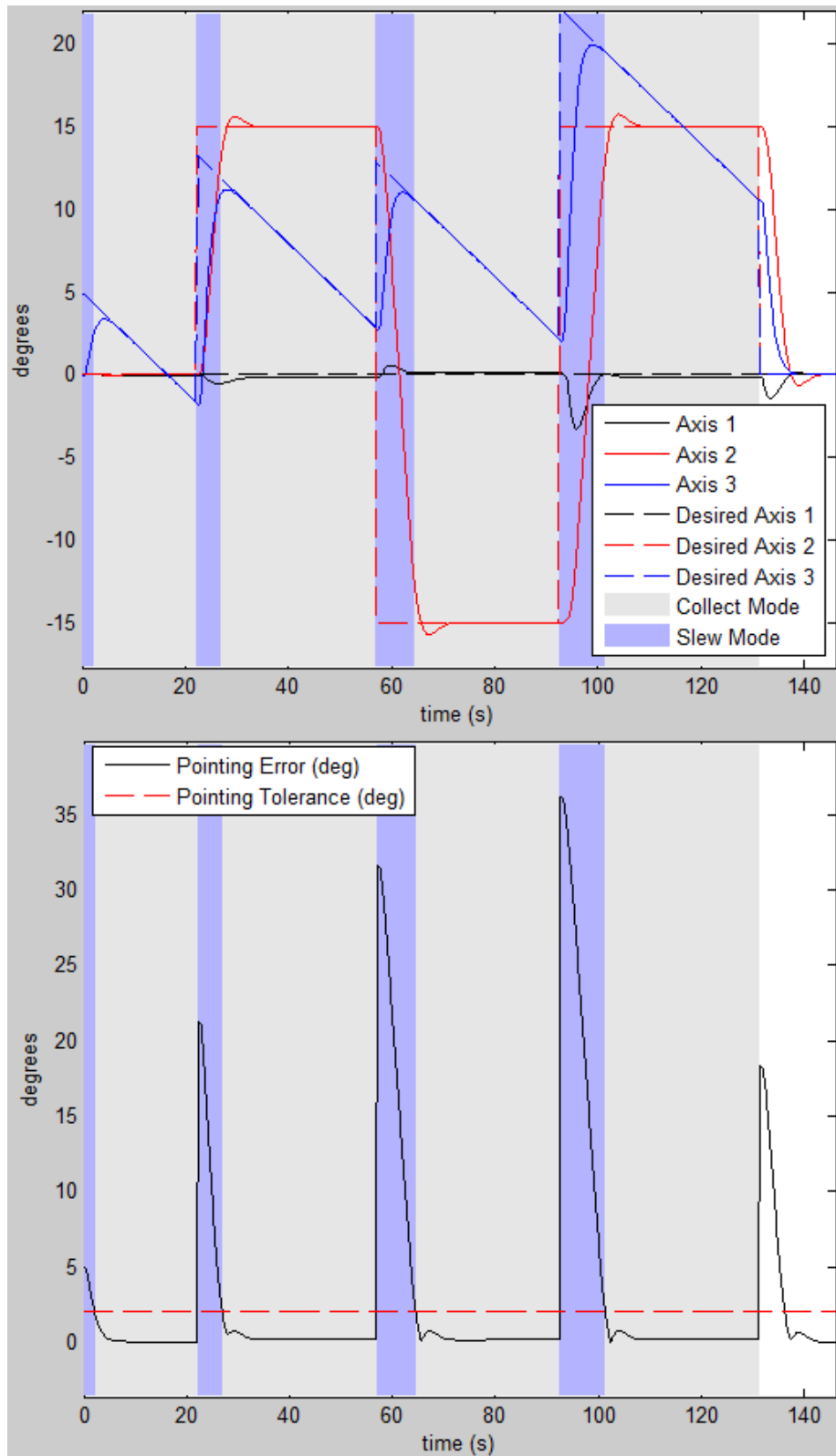
Figure 4.5: CB Euler Angles vs. Time (left) and Pointing Error vs. Time (right) - Analytical Simulation

as the analytical simulation. No mathematical difficulties are observed in the RWCMG hardware experiments with these initial conditions.

The same controller experiment settings are also used in the analytical and hardware versions. No null motion is used during collect phases. All controller gains are adjusted for damping ratio and natural frequency parameters as described in Section 2.4. Euler angle versus time plots beside their corresponding pointing error plots for each of the three controllers performing the RWCMG mission on SimSat are shown in Figures 4.6 through 4.9 to motivate the discussion that follows.

As with the analytical simulation, the PID controller struggles to achieve the pointing accuracy levels of the other two controllers, although with SimSat the PID-controlled experiment does not deviate from the required tolerance level once first achieved for any target. Without the collection interruptions experienced by the analytical simulation, the hardware PID experiment finishes the representative mission in 141.8 seconds - 28 seconds faster than the analytical simulation. The total RSS error statistic for the PID-controlled hardware experiment is 24% lower than the analytical simulation. This fact is due in large part to the lower overshoot achieved in the hardware experiment. Gain adjustment for the analytical version may improve performance to diminish the collection interruptions and bring results closer to those achieved in the hardware experiment. Further investigation of gain adjustment is a recommended topic for further study in Chapter V. The hardware PID experiment suffered only one near-singularity compared to two in the analytical simulation. The average singularity measure for the hardware PID experiment was 0.459 compared to 0.625 for the analytical simulation.

The QF-controlled hardware experiment yields results very similar to the analytical simulation in terms of singularity metrics. Total RSS error for the experimental QF-controlled mission is 36% higher than the QF analytical simulation. Completion time for the hardware QF mission is 1% slower than the analytical simulation. Comparing the

102

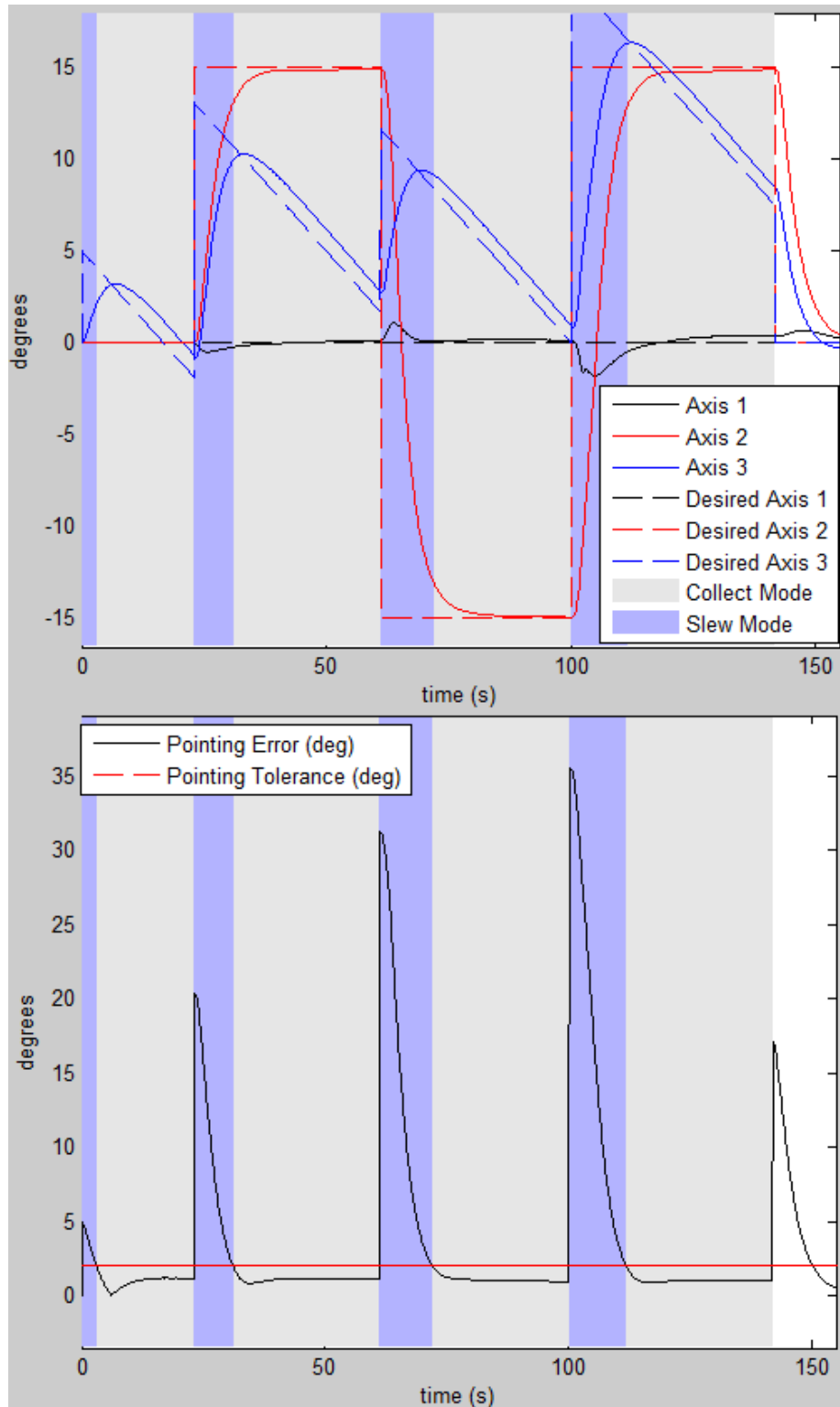Figure 4.6: PID Euler Angles vs. Time (top) and Pointing Error vs. Time (bottom) - Hardware Experiment
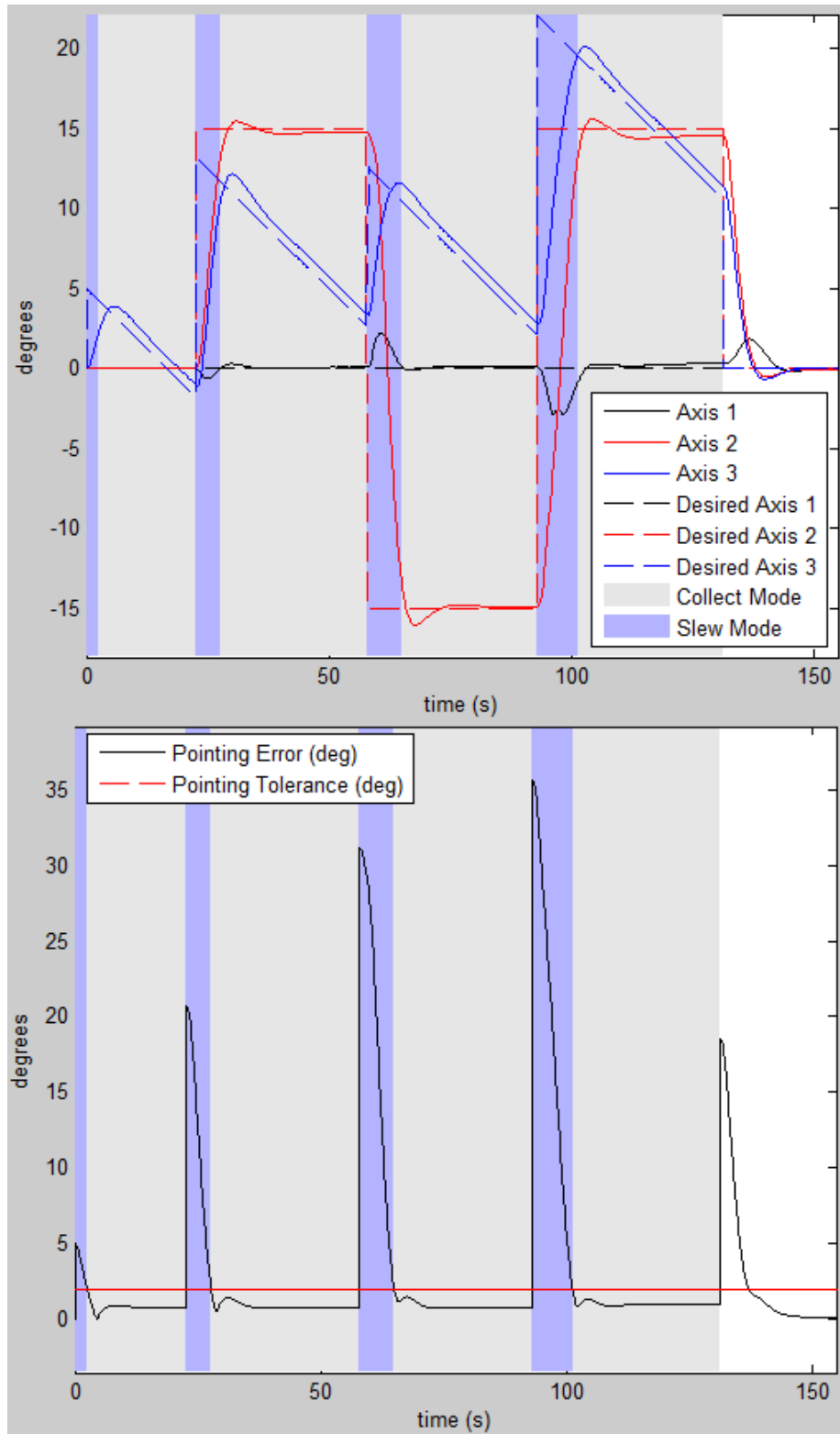
103

Figure 4.7: QF Euler Angles vs. Time (top) and Pointing Error vs. Time (bottom) - Hardware Experiment
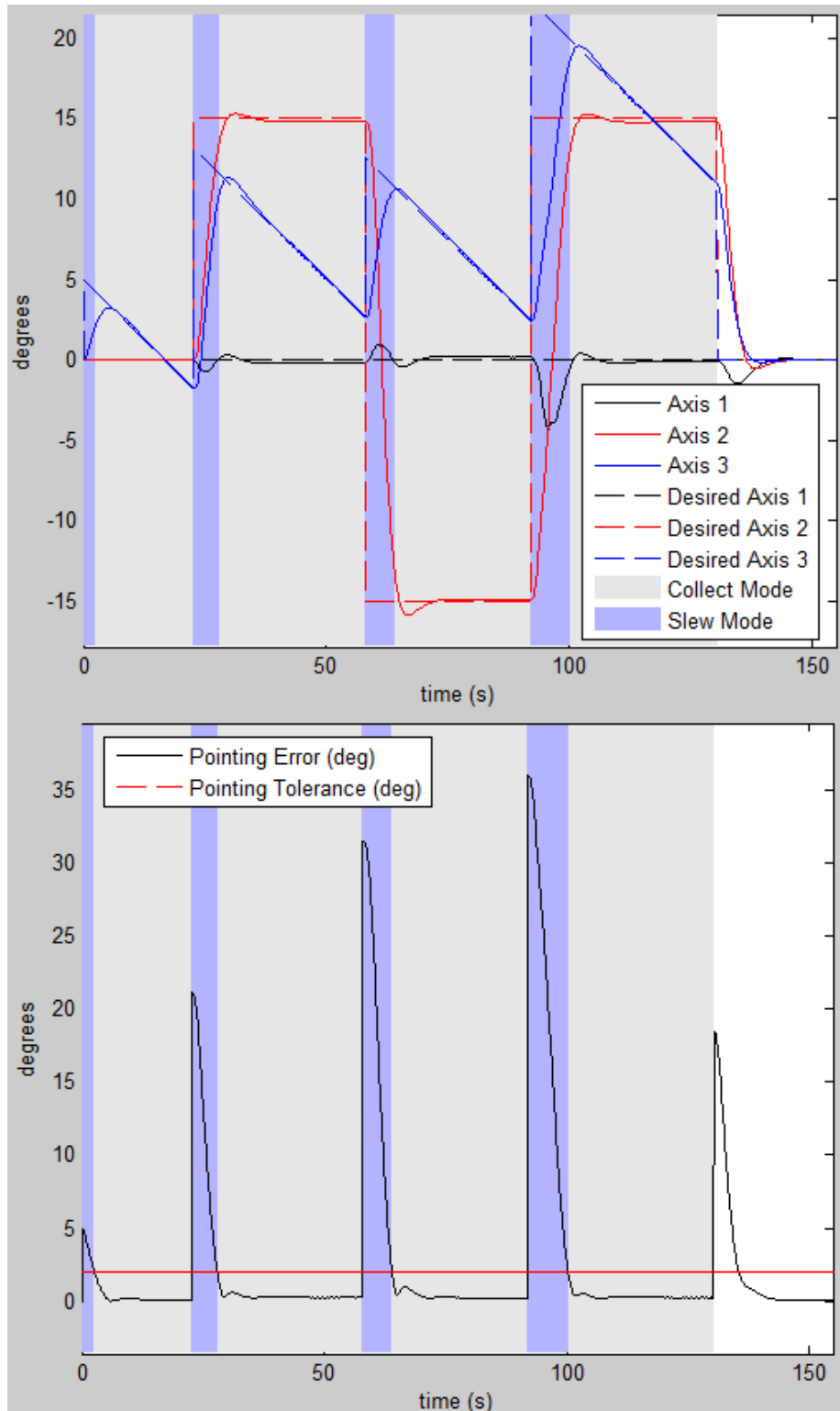
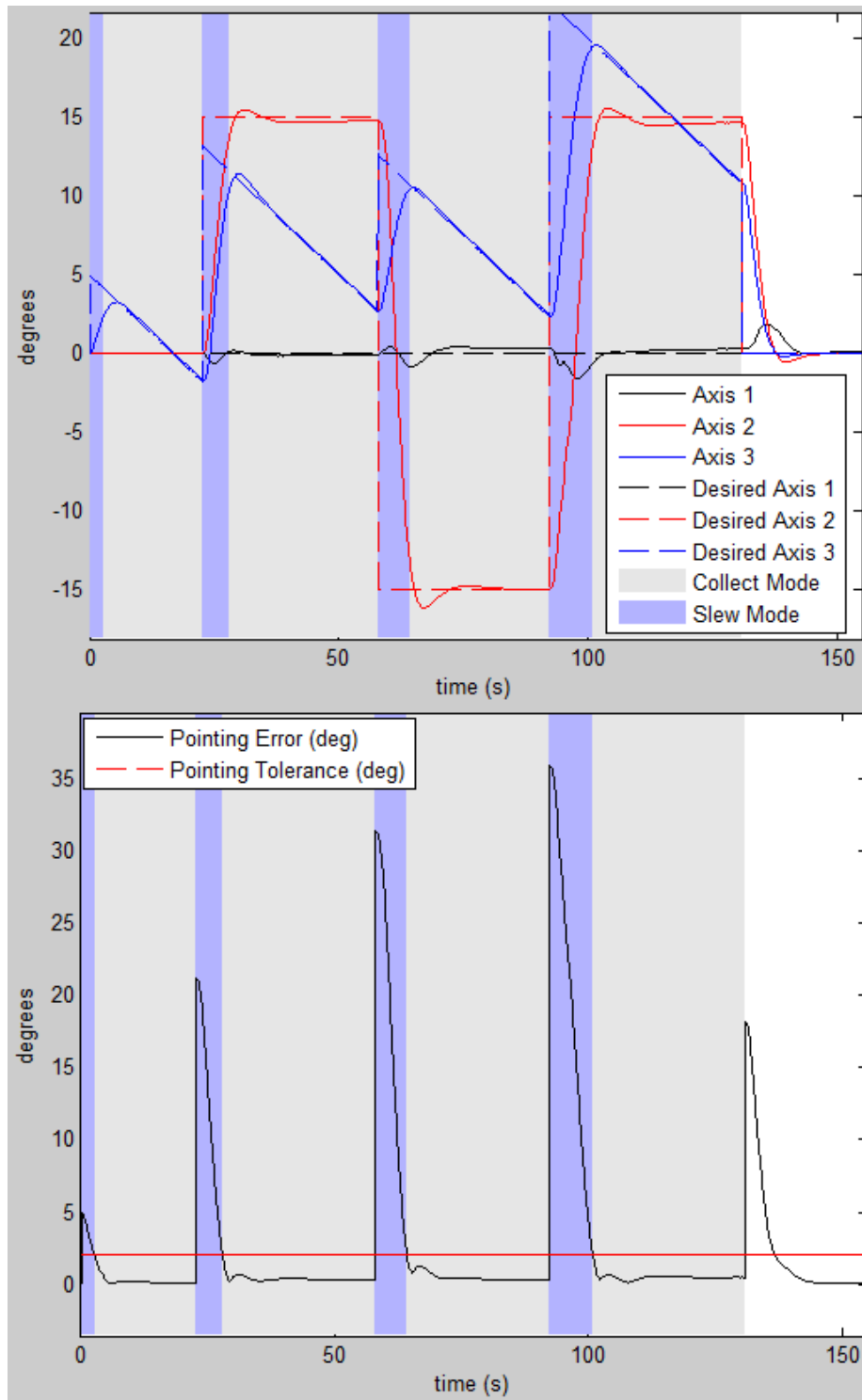Figure 4.8: LB Euler Angles vs. Time (top) and Pointing Error vs. Time (bottom) - Hardware Experiment

Figure 4.9: CB Euler Angles vs. Time (top) and Pointing Error vs. Time (bottom) - Hardware Experiment

Table 4.2: Comparison of Controllers for the RWCMG Mission - Hardware Experiment

	PID	QF	LB	CB
Completion Time (sec)	141.8	131.2	130.3	130.9
Total RSS Error (deg)	37.21	31.75	14.88	18.37
Total RMS Error (deg)	1.108	0.895	0.417	0.517
Number of Near-Singularities	1	2	1	1
Average Singularity Measure	0.459	0.630	0.542	0.489

experimental QF-controlled mission to the experimental PID-controlled mission however, reveals that the QF results in a 14% improvement over the PID in terms of pointing accuracy. A final mission time of 131.2 seconds is achieved with the QF controller compared to 141.8 seconds for the PID experiment. However, the experimental QF-controlled experiment suffers from a steady-state error on the dynamic axis. Pointing error for the static axes one and two is relatively low compared to the dynamic axis. The QF controller results in only two instances of near singularities. Error and singularity statistics for the QF controller are included in Table 4.2.

Moving on to the LB-controlled hardware experiment of Figure 4.8, the steady-state error in tracking the dynamic axis is greatly diminished compared to the QF-controlled experiment. The LB-controlled experiment results in a 53% reduction in total RSS error compared to the experimental QF-controlled experiment. As in the analytical case, the nonlinear term in the LB controller is better equipped to track the moving target than the other controllers. The hardware experiment LB-controlled mission finishes in 130.3 seconds compared to 131.2 seconds for the QF experiment. Error and singularity statistics for the LB controller are included in Table 4.2.

A combined QF and LB controller is also implemented on the SimSat hardware platform. As with the analytical simulation, the hardware CB experiment results in metrics slightly better than the QF but slightly worse than the LB with the exception of average singularity measure, which is worse than both individual controllers. Error and singularity statistics for the CB controller are included in Table 4.2.

Similar to the analytical simulation, the hardware experiment LB controller produces the fastest mission completion time. The LB controller also produces the lowest error statistics. The larger number of near-singularities for the LB controller in the analytical simulation is not witnessed in the hardware experiment. A possible explanation for this observation is that the LB-controlled analytical simulation caused some violations of desired state limits which will be discussed in the next section. With CMG gimbals rotating at faster rates in the analytical simulation compared to the hardware experiment, the probability of encountering singularities increases. The QF controller produces the best average singularity metric value. Overall, the LB controller is deemed the best controller for the RWCMG hardware experiments based on overall metric consideration.

A comparison of analytical simulation controller performance from Table 4.1 and hardware experiment results of Table 4.2 shows that with the exception of the PID controller, the analytical simulation achieves better completion times than the hardware experiments. The analytical simulation LB-controlled mission finished almost 3% faster than the LB-controlled hardware experiment. Even though the limit enforcement algorithm is active for the analytical simulation, slight violations of desired state constraints discussed in the next section are the likely cause of the discrepancy. The PID-controlled analytical simulation achieved a completion time almost 20% slower than the corresponding hardware experiment due to the fact that the analytical simulation PID mission failed to maintain pointing accuracy requirements continuously during the collect phase as discussed above. Gains were adjusted for each controller based on natural frequency and damping ratio

values to create a consistent comparison, however further adjustment of the PID gain for the analytical model could potentially improve pointing accuracy to levels closer to those observed in the hardware experiments. Pointing accuracy for the other three controllers is better in analytical simulation than the values achieved through hardware experiments. Singularity avoidance metric comparisons between analytical simulation and hardware experiments are varied with the controller selection. Performing additional hardware runs to gain statistical significance may provide a better means of comparing analytical simulation and hardware experiments in terms of singularity avoidance for each controller and is a recommended topic for future research in Section 5.3.4. With controllers evaluated for both analytical simulation and hardware experimentation, attention now turns to evaluation of the hardware limit enforcement algorithm in the analytical simulation.

4.2   Limit Enforcement Accuracy

The Limit Enforcement block of the analytical closed-loop control scheme plays an important role in keeping simulation results reasonable with respect to constraints derived from hardware limits. In the discussion on analytical simulation controller performance the LB controller gimbal rate plot of Figure 4.4 showed a slight violation of the desired constraints. Section 3.2.4 explains the iterative approach of enforcing constraints on the analytical simulation. The following discussion assesses the Limit Enforcement algorithm with regard to each state on which it acts. Discussion of the accuracy of this method follows.

The first state affected by the Limit Enforcement block of the closed-loop control scheme is s/c angular rate $|\vec{\omega}|$. The absolute value notation is in place to denote that the magnitude of the s/c angular rate is constrained, but not the direction. A RWCMG mission run with the same setup as the control experiment above, using the LB controller, allows analysis of Limit Enforcement with regard to $|\vec{\omega}|$. The RWCMG mission run with the Limit Enforcement block active results in the spacecraft angular rate history shown in Figure

4.10.   The hardware-derived limit of 8° per second as listed in Figure 3.1 is denoted with
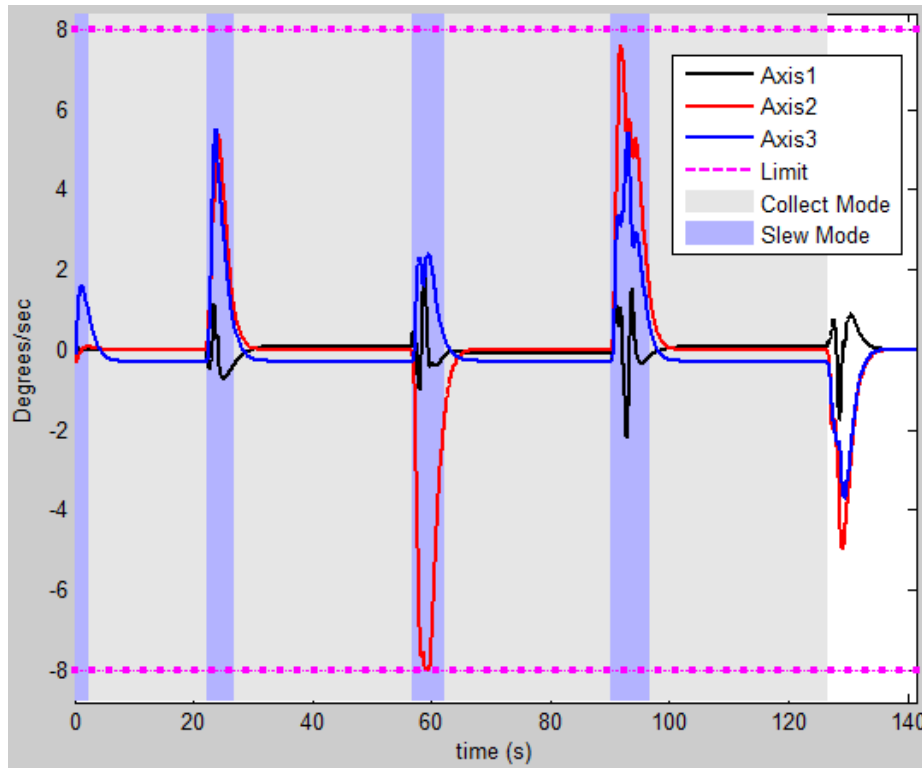
Figure 4.10: Spacecraft Angular Rate vs. Time - Analytical Simulation with Limits On

a dashed magenta line at ±8° on the plot. Large spikes in angular rate are evident during slew phases, but those spikes in angular rate are within the constraints. The same RWCMG mission run with the Limit Enforcement algorithm block turned off results in the spacecraft angular velocity plot of Figure 4.11.

   Note in Figure 4.11 that spacecraft axis two violates the 8° per second limit when slewing to targets three and four. Without the Limit Enforcement block active the RWCMG analytical simulation produces results which cannot be achieved in hardware. Thus for the $|\vec{\omega}|$ state, the Limit Enforcement block reduces 100% of the limit violation and is deemed effective. The limit enforcement block was active during all simulations in the RWCMG research.
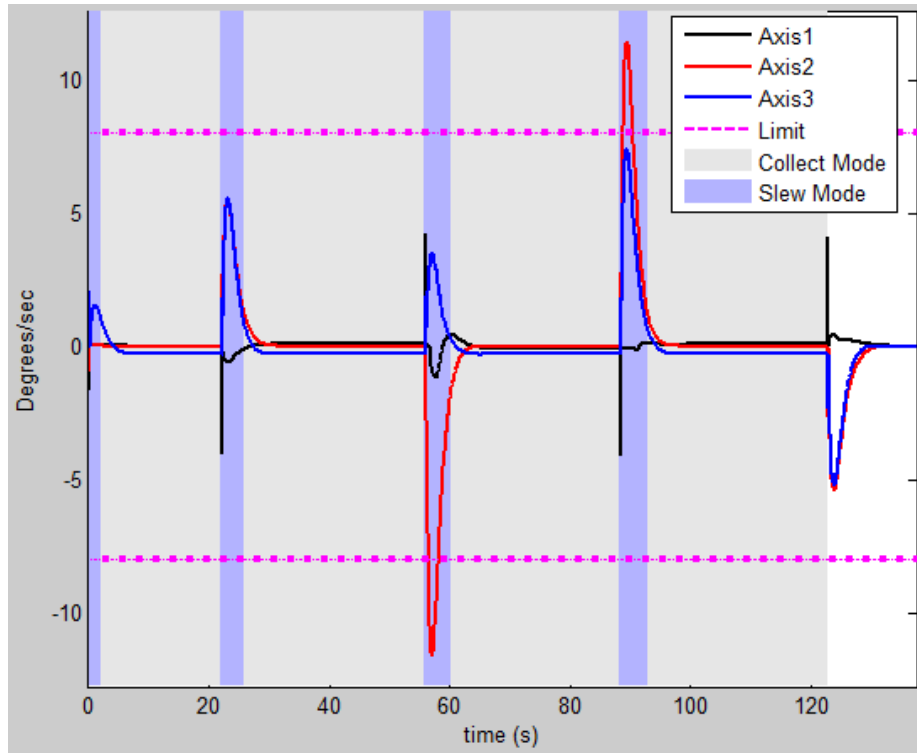
Figure 4.11: Spacecraft Angular Rate vs. Time - Analytical Simulation with Limits Off

Next we will discuss rate limits on CMG gimbal rate state $\left|\vec{\dot{\delta}}\right|$. Figures 4.12 and 4.13 show the gimbal rate histories for RWCMG simulations with the Limit Enforcement block on and off respectively. Note in Figure 4.12 that although the Limit Enforcement algorithm is turned on, there are still several violations of the desired 2.5 radian per second limit. When compared to the magnitude of the limit violation shown in Figure 4.13 however, the relatively small violations with the Limit Enforcement block on are preferable. Notice in the unlimited CMG gimbal rate plot CMG four reaches a peak rate over 55 radians per second slewing to target four. One possible cause for the small violations of CMG gimbal rates with the limit algorithm active is the necessary use of the pseudo-inverse in the equations of motion. Calculation of gimbal rates for the RWCMG system uses the weighted pseudo-inverse of Eq. (2.28). Pseudo-inverse calculations introduce some error into the equations of motion. When operating backward as happens frequently in the Limit

111

Enforcement block, the revised control torque $\dot{\vec{h}}_{act}$ is recalculated based on limited CMG gimbal angle rates, thus introducing the pseudo-inverse error into the system. Further study of applying limits to the RWCMG analytical simulation is a recommended topic for future study in Chapter V. Based on the highest absolute rate limit violations of Figures 4.12 and 4.13, the Limit Enforcement algorithm reduces 94% of the limit violation. Since the Limit Enforcement block is 94% effective in achieving the desired limits on CMG gimbal rate but does not fully constrain the value, the algorithm is deemed marginal with respect to $|\dot{\vec{\delta}}|$.
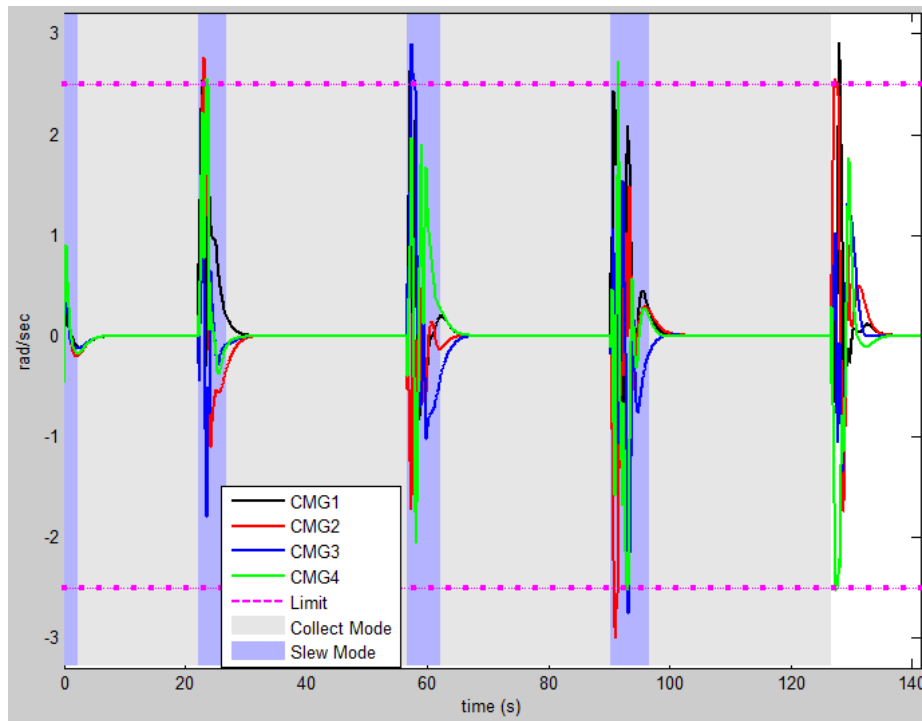
Figure 4.12: CMG Gimbal Rate vs. Time - Analytical Simulation with Limits On

Similar to CMG gimbal rate, the Limit Enforcement block significantly limits CMG gimbal acceleration, however falls short of maintaining the standard aggressively. Pseudo-inverse error is again a likely culprit for the slight violations in the limited version. The Limit Enforcement block is again given a marginal rating for enforcing $|\ddot{\vec{\delta}}|$. Figures 4.14 and

112
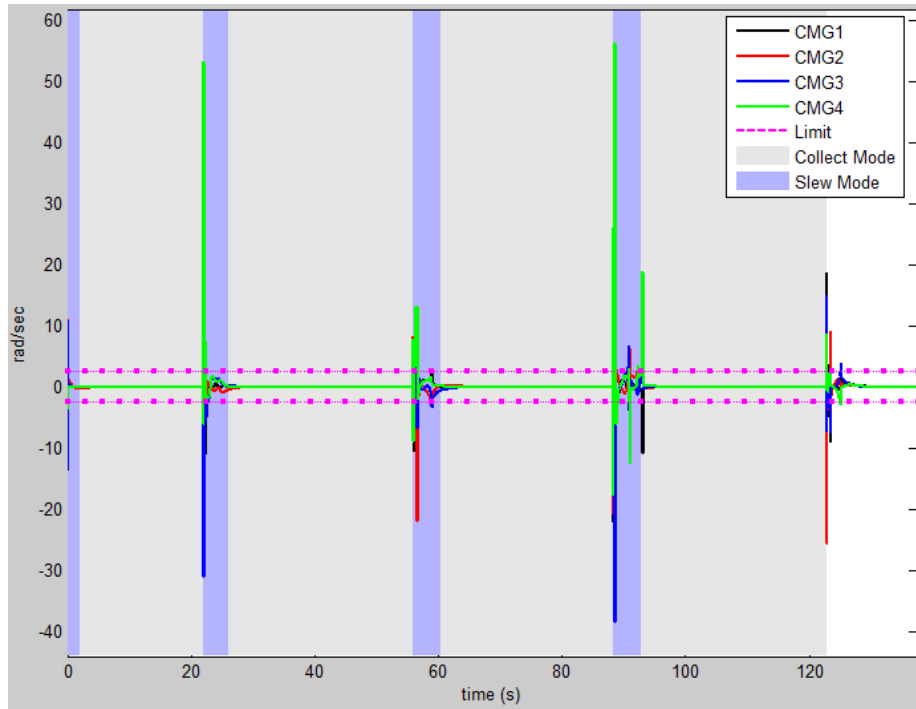
Figure 4.13: CMG Gimbal Rate vs. Time - Analytical Simulation with Limits Off

4.15 show the performance of the limit enforcement block on CMG gimbal acceleration. Note that CMG four reaches a peak of 594 radians per second squared when slewing to target two in the unlimited plot. The highest gimbal acceleration in the run with the limiter enabled is less than 19 radians per second squared making the Limit Enforcement algorithm 97% effective for $\left| \ddot{\vec{\delta}} \right|$.

As explained in Section 3.2.4, reaction wheel rates limits are not stressed with the RWCMG representative mission and careful use of null motion. An examination of singularity metrics with respect to the Limit Enforcement block does provide one more interesting finding however. Plots of singularity indices for the same RWCMG mission with and without limits enforced are shown in Figures 4.16 and 4.17 respectively. Note in Figure 4.17 that the CMG gimbals are in a near singular state during the entire collection period of target three. The gimbals are not rotating during the collection phase of this particular RWCMG setup since null motion is not being used. The reaction wheels are in
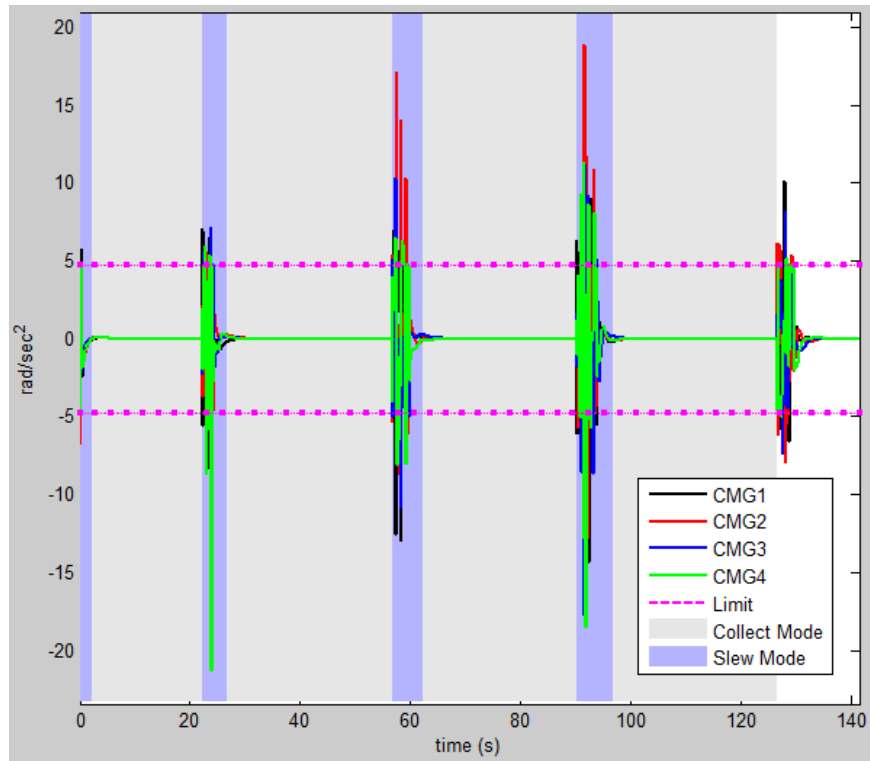
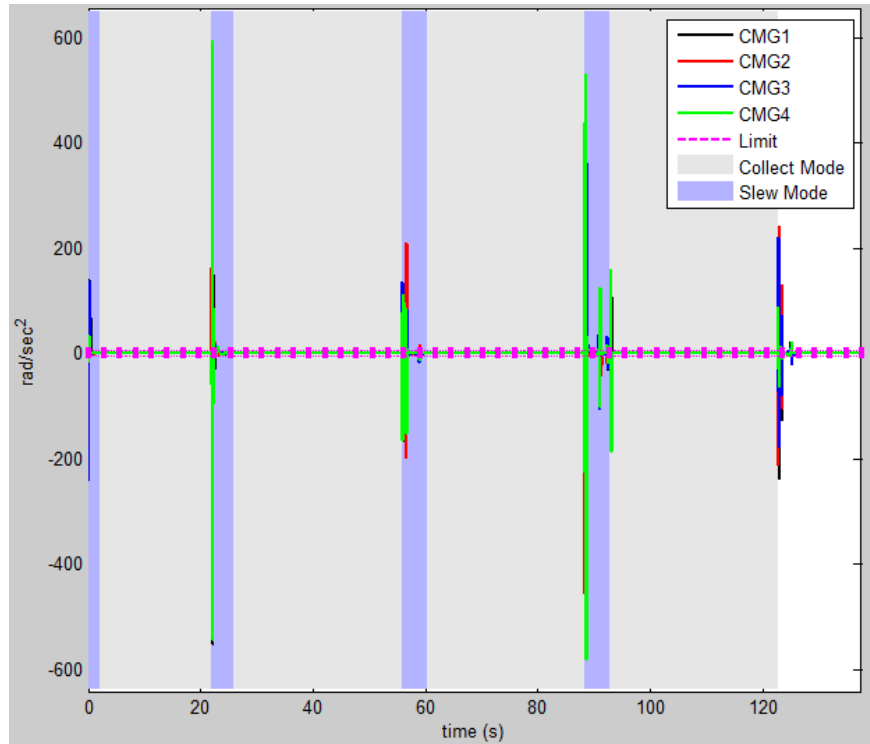Figure 4.14: CMG Gimbal Acceleration vs. Time - Analytical Simulation with Limits On

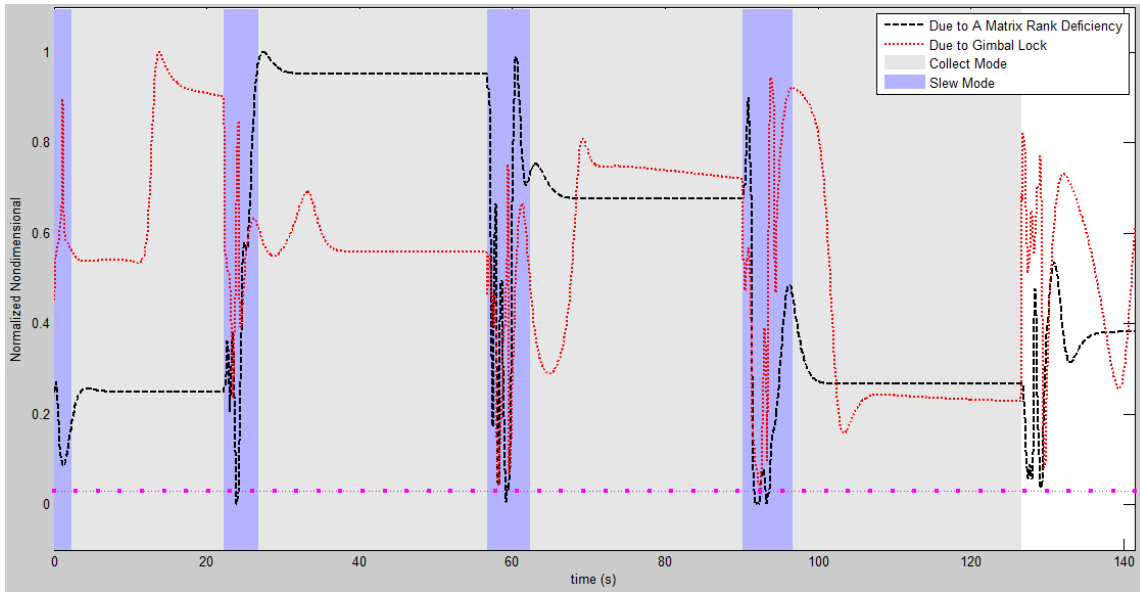Figure 4.15: CMG Gimbal Acceleration vs. Time - Analytical Simulation with Limits Off

Figure 4.16: Singularity Metrics vs. Time - Analytical Simulation with Limits On
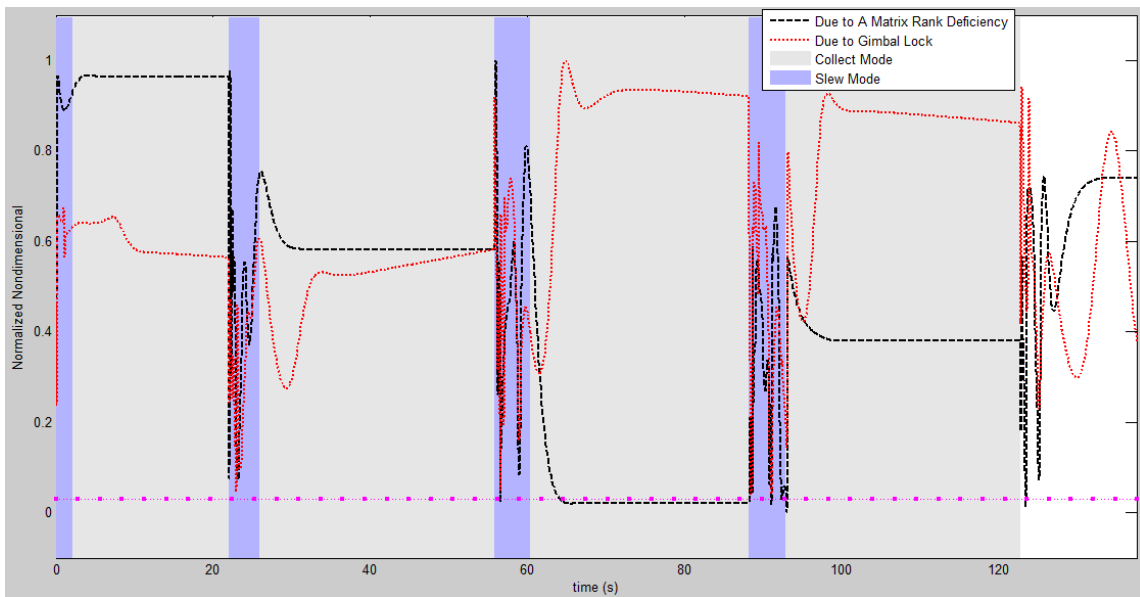
Figure 4.17: Singularity Metrics vs. Time - Analytical Simulation with Limits Off

115

complete control of the spacecraft after the transition period. Thus, the gimbals happened to stop moving at the end of the transition period slewing to target three and stayed there for the whole transition period. Singularity avoidance algorithms are required to act quickly at the end of target three collection to provide the required torque to slew to target four. If one were to evaluate the number of near-singularities for the RWCMG mission without constraints imposed, the value seems very large compared to results from the controller evaluation above - 247 time steps spent in a near-singular condition out of a simulated mission consisting of 1228 total time steps. However when noticing that 243 of those time steps are a result of the gimbals holding stationary for the collection phase, the metric takes a different meaning.

The metrics for the two RWCMG cases - with and without limits imposed - are shown in Table 4.3. Note that the final time for the unlimited run is almost seven seconds faster than any of the hardware runs of Table 4.2. Analytical runs in the controller simulation of Table 4.1 are performed with the Limit Enforcement block active and match the hardware experiment completion time metric much more closely.

Table 4.3: Limit Enforcement Metrics for the RWCMG Mission - Analytical Simulation

	Limited	Unlimited
Completion Time (sec)	126.5	122.7
Total RSS Error (deg)	10.79	12.01
Total RMS Error (deg)	0.215	0.237
Number of Near-Singularities	18	247
Average Singularity Measure	0.518	0.485

116

4.3 Preferred Gimbal Angle and Null Motion Performance Evaluation

With the analytical simulation at least marginally limited with respect to known constraints, attention now turns to evaluation of both analytical simulation and hardware experiments in performing null motion of gimbal angles. Recall from Sections 3.2.5 and 3.3.1 that the desired operation of the satellite during collect mode is to use reaction wheels to maintain the required attitude while the CMG gimbals are rotated through trajectories of null motion to preferred angles. The section begins with a discussion on tuning the null motion gain k of Eq. (3.31). Next, each controller from Section 4.1 is used in the RWCMG mission with null motion and evaluated. Results from implementing the three methods of deriving preferred gimbal angles for the analytical simulation and two methods for SimSat hardware experiments are shown next. Another analysis is made by starting the RWCMG mission with various starting gimbal angle configurations. Finally, the RWCMG actuation technique with null motion is compared to a traditional CSCMG actuation scheme in order to quantify benefits of the RWCMG system.

4.3.1   Null Motion Gain Tuning.

The gain k of Eq. (3.31) controls the maximum CMG gimbal rate $\dot{\delta}$ on their assigned null motion trajectories where a higher gain value corresponds with a higher gimbal rate. Since Eq. (3.31) minimized distance in a least-squares sense, the gimbals travel along null motion trajectories until no further overall improvement is available. Once reaching the least-squares distance from the preferred gimbal angles, the rotation stops. This stopping of gimbal rotation in pursuit of preferred values is labeled least-squares-close for future reference. When setting the null motion gain, two aspects of the RWCMG mission must be considered. First, the null motion gain must be set high enough that the gimbals all reach least-squares-close before the collect phase ends. If the gain is too low, the CMG gimbals will still be rotating when the next slew phase starts. In this low-gain case, the gimbals are not as close to the preferred values as possible which would result in a non-optimal gimbal

configuration for the next slew. A higher gain is needed to bring the gimbals closer to the preferred values. The second aspect of the RWCMG mission which must be considered when setting the null motion gain is disturbance torque. In the analytical simulation, disturbance torque is not modeled. Null motion of the gimbals occurs in a mathematically perfect null space and imparts no torque while the gimbals travel toward preferred values. In hardware experiments, perfectly torque-free null motion is not possible. Like the old quandary of whether walking or running through the rain results in getting the least wet, the question arises with null motion: does slower gimbal motion over a longer time period, or faster gimbal motion over a shorter time period induce less disturbance torque? Empirical hardware experiments with the RWCMG system are required in order to characterize the null motion disturbance torque not modeled in analytical simulation.

To analyze the first null motion aspect of the RWCMG mission - ensuring gain is high enough to reach least-squares-close to preferred values - consider a hardware simulation which uses the Vadali [2] preferred angle set of $[45°, −45°, 45°, −45°]$. Figure 4.18 shows gimbal angles during collect mode for target three of a RWCMG mission. Dashed lines on the plot show the preferred angles of $+45°$ for gimbals one and three and $−45°$ for gimbals two and four. Shading on the plot shows the transition from slew mode in blue to collect mode in dark gray at 64 seconds. Another shift from dark gray to light gray at 70 seconds shows when the six second transition from CMG control actuation to RW actuation occurs. Collection is proceeding during both gray sections - from 64 seconds to 92 seconds. Null motion is turned on for this mission with a gain value of $k = 0.15$ and begins at the start of the light gray background shading at 70 seconds. Note that the gimbals are still rotating (gimbal angle plot lines are not fully horizontal) when the collect mode ends at 92 seconds and the next slew begins. This means the null motion gain is not high enough for the gimbals to reach least-squares-close to the preferred values before the collect phase ends. Figure 4.19 shows the same RWCMG mission with a null motion gain of $k = 0.9$.
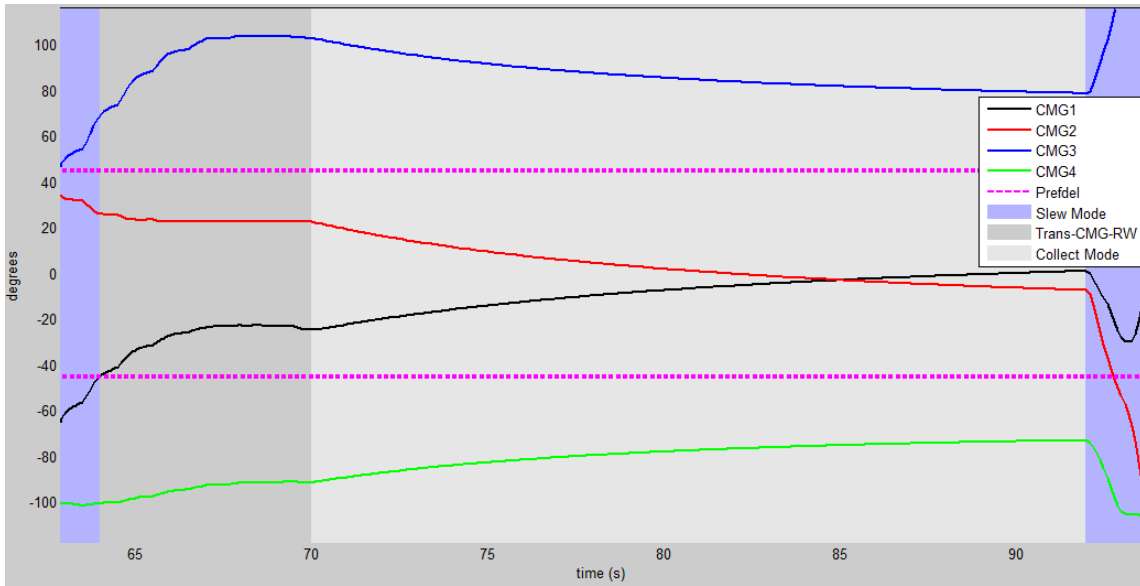
Figure 4.18: Gimbal Angles vs. Time for Target 3 of a RWCMG Mission and Null Motion Gain 0.15 - Hardware Experiment

With higher null motion gain the gimbals rotate toward the preferred values at a faster
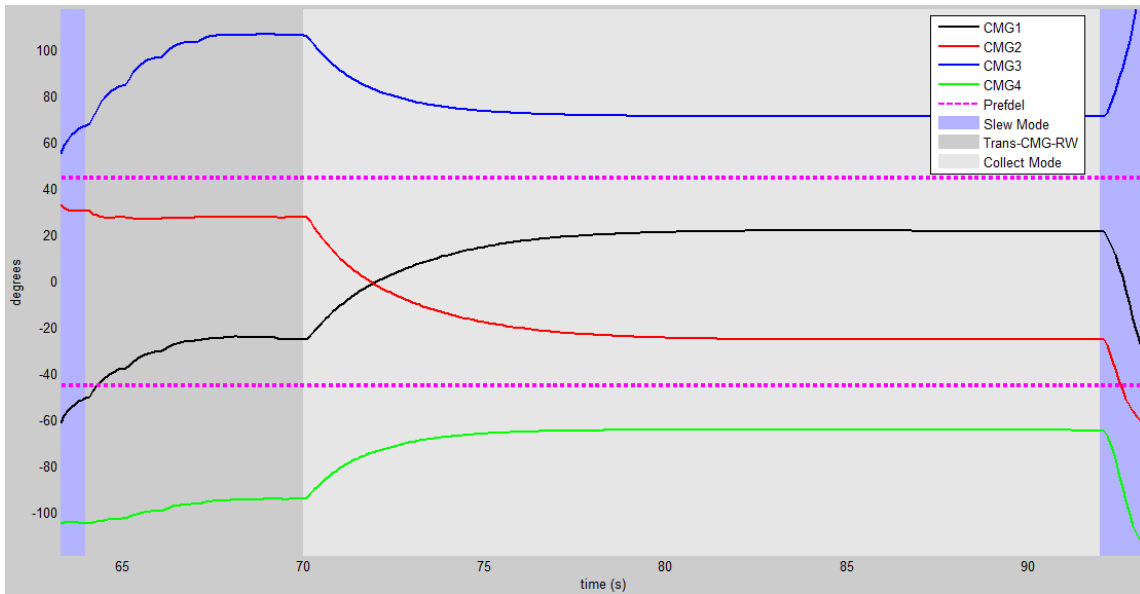
Figure 4.19: Gimbal Angles vs. Time for Target 3 of a RWCMG Mission and Null Motion Gain 0.9 - Hardware Experiment

rate and reach least-squares-close at approximately 80 seconds. From 80 seconds until the start of the next slew the gimbals hold at a constant angle. Taking the two-norm of the difference between achieved and preferred gimbal angles allows a parametric study of null motion gain and the rate of achieving least-squares-close. The results of three hardware experiment runs with varying values of k are shown in Figure 4.20. As shown in Figure
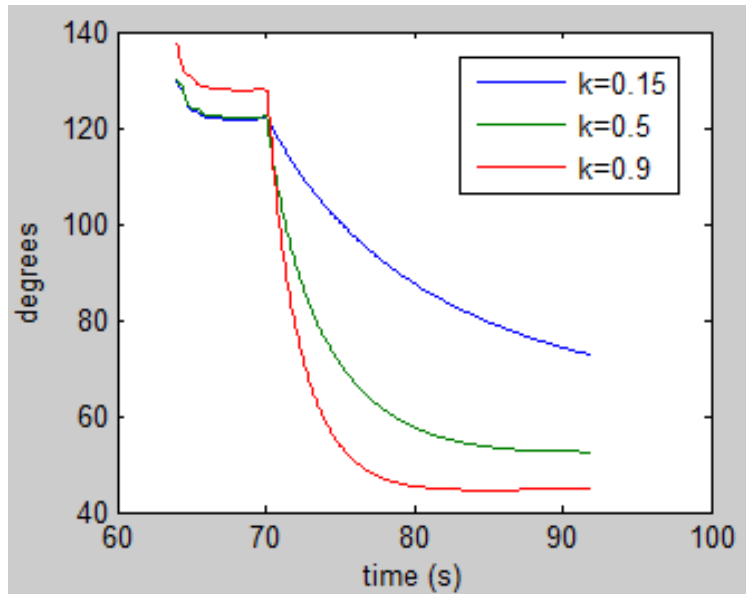
Figure 4.20: Maximum-Normalized Error Between Achieved and Preferred Gimbal Angles vs. Time - Hardware Experiments

4.18, the normed error of the RWCMG hardware run with $k = 0.15$ did not reach a steady least-squares-close value when the collect phase ended. Runs with $k = 0.5$ and $k = 0.9$ did achieve least-squares-close. When running RWCMG experiments the engineer must tune the null motion gain to ensure all possible benefit (faster slews and improved singularity avoidance) of the null space is used.

The second aspect of null motion gain tuning is disturbance torque. Recall the question is whether a greater overall level of disturbance torque is imparted with a longer slower null motion period or with a shorter faster period. Though instantaneous disturbance torques are higher with a faster gimbal motion, the application of the RWCMG control scheme does

not result in reaction wheel saturation from instantaneous torques. Recall the null motion occurs during a relatively calm collection mode - the reaction wheels are assumed to have adequate torque capability to compensate for instantaneous disturbance torque spikes while controlling the spacecraft. The question being asked is what null motion scheme - fast or slow - produces the smallest aggregate level of disturbance torque over the course of the collect phase. To answer this question a method of quantifying the overall disturbance torque is necessary. Toward this end, a hardware run in which no null motion occurs acts as the baseline for reaction wheel rate. Similar to the controller tests from Section 4.1, a RWCMG hardware experiment which uses the CMG pyramid to slew to the targets, enters a transition period where control is passed to the reaction wheels, and performs a collection phase in which the CMG gimbals are locked at their current angles allows a 'clean' run to characterize the required reaction wheel rates to image the targets. Next, a comparison of reaction wheel rates from the three hardware runs in which null motion is used to the clean run reaction wheel rates yields a metric to characterize the overall disturbance torque levels.

Looking at the same target three collection phase as used in the above least-squares-close study, the reaction wheel rates for the no null motion case and three varying values of k cases are shown in Figure 4.21. Taking the two-norm of the difference between reaction wheel rates of cases using null motion and the case in which no null motion is used yields a plot of values for the three null motion gain cases which represent the amount of disturbance caused by the null motion. Taking the sum of those norm values over the time period of the collect phase gives what is termed here as a Disturbance Torque Score. The lower the Disturbance Torque Score, the lower the overall level of disturbance torque on the system. Results of this study are shown in Figure 4.22. Perhaps contrary to engineering intuition, the case with the highest null motion gain, $k = 0.9$, produces the lowest Disturbance Torque Score. This case produces the highest magnitude of disturbance
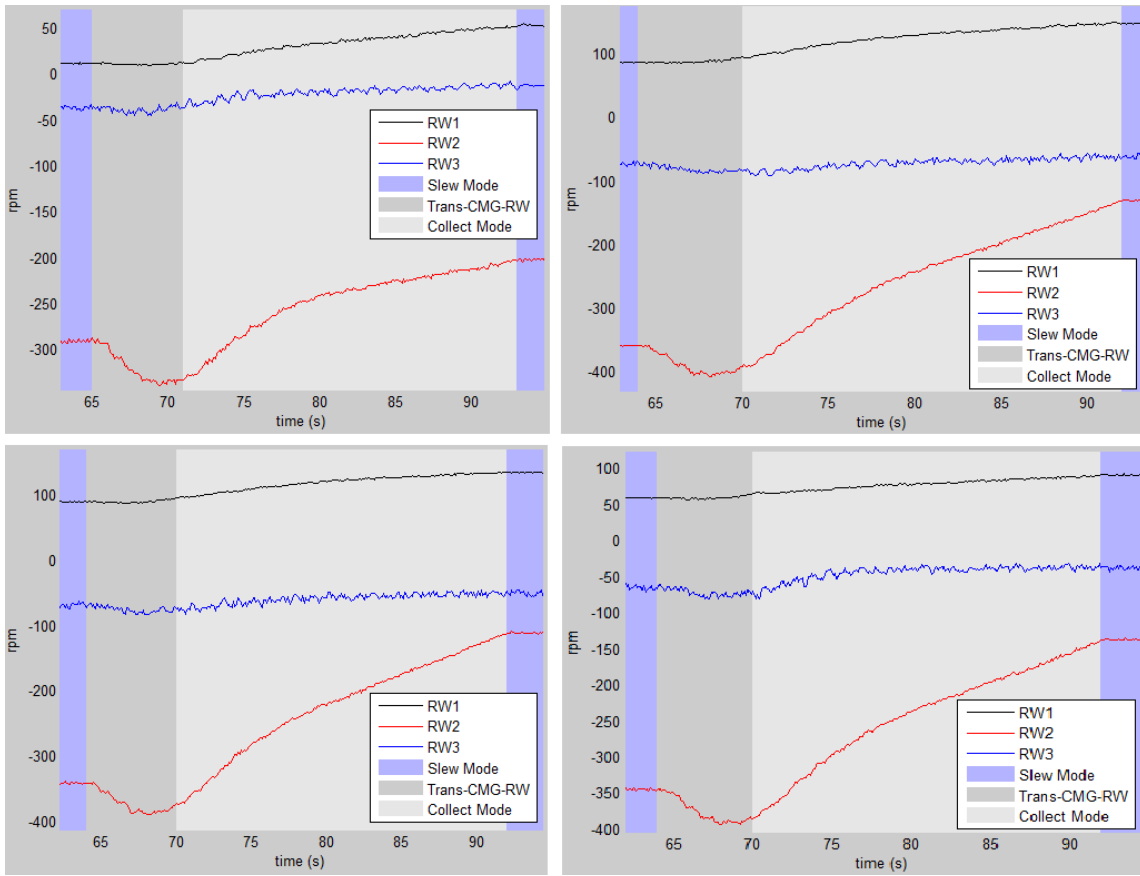
121

Figure 4.21: Reaction Wheel Rates vs. Time for Cases: No Null Motion (top left), $k = 0.15$ (top right), $k = 0.5$ (bottom left), $k = 0.9$ (bottom right)

torque early in the collect phase, but the overall level of disturbance torque on the system is the lowest. With the results of the two aspects of null motion gain tuning in hand, the recommendation for future RWCMG users is to set the null motion gain as high as possible while monitoring for any instantaneous disturbance torques that might cause trouble for the reaction wheels. Characterization of the null motion disturbance torque with hardware experiments is considered a contribution of the presented research. With a more complete understanding of null motion gain tuning, results of using the investigated controllers for null motion cases now follows.

4.3.2   *Controller Performance for Null Motion.*

In Section 4.1, the PID, QF, LB, and CB controllers were evaluated for the RWCMG mission without null motion in order to baseline performance. Now a short examination is made with respect to each controller's performance with null motion on. Each of the RWCMG runs for the null motion controller experiment use the Vadali preferred gimbal angles [2]. Limit enforcement algorithms are turned on for the analytical simulations. Table 4.4 shows metrics for each controller performing the RWCMG mission with null motion for analytical simulation (A) and hardware experimentation (H). Some performance trends from Section 4.1, in which the RWCMG mission is performed without null motion, continue when null motion is performed. The LB controller results yield slightly worse singularity metrics than the other controllers. The PID controller fails to achieve the pointing accuracy and completion time in the family of the other controllers. In fact, the PID controller completes the mission 7% slower running the RWCMG mission with null motion than the PID mission without null motion. The reason for this goes back to the fact that the PID controller is not able to maintain pointing tolerance once first achieved. Due to the multiple switches between collect mode and slew mode for the PID, the gimbals are frequently forced to resume control of the spacecraft to regain pointing tolerance. By the time the PID-controlled mission achieves a lasting fix on the target there is not enough time
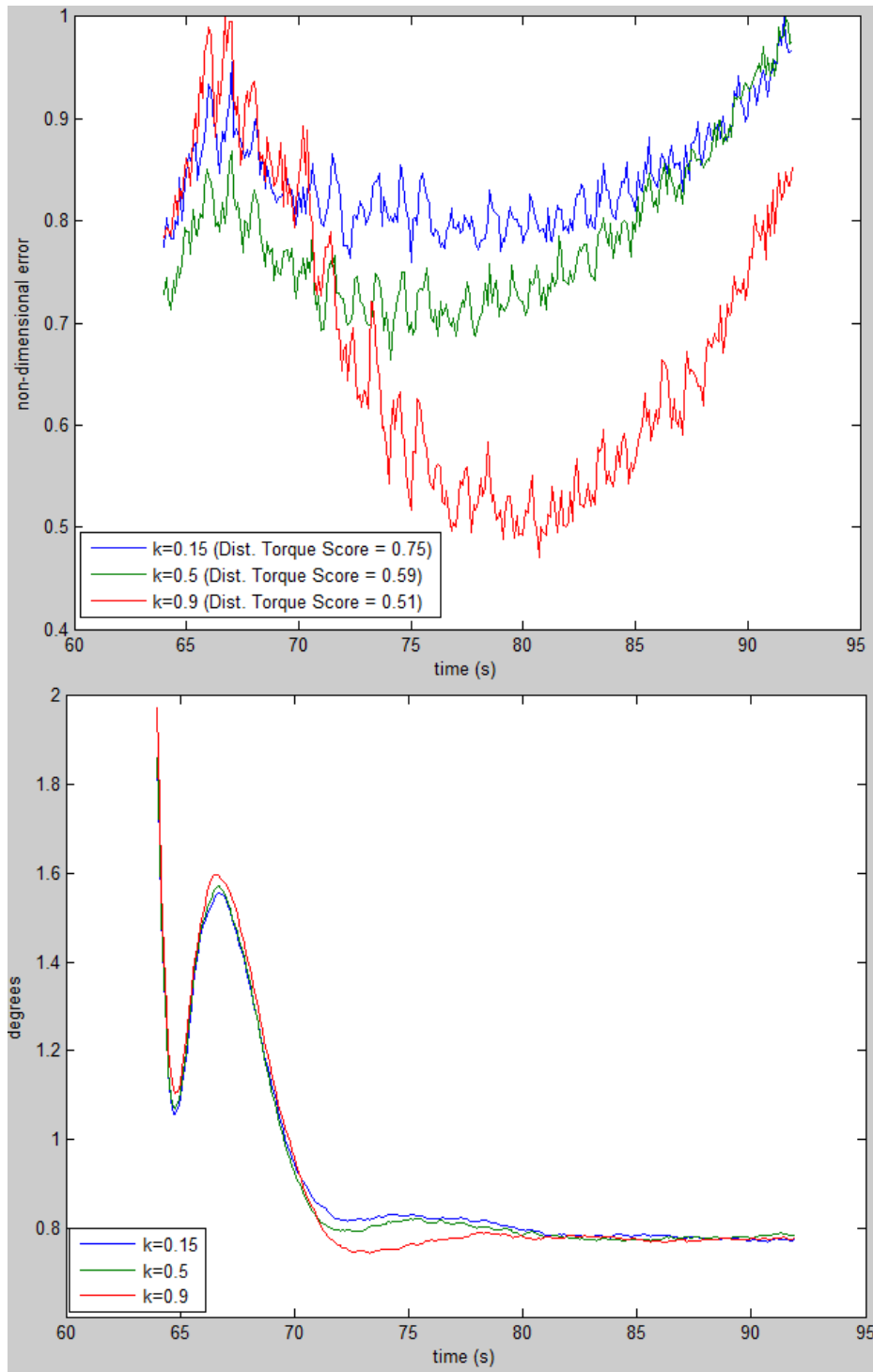
123

Figure 4.22: Maximum-Normalized Error Between Reaction Wheel Rates While Null Motion Occurs and Without Null Motion vs. Time (top) and True Pointing Error vs. Time (bottom) - Hardware Experiments

124

Table 4.4: Comparison of Controllers for the RWCMG Mission with Null Motion - Analytical Simulation (A) and Hardware Experiment (H)

	PID		QF		LB		CB	
	A	H	A	H	A	H	A	H
Compl. Time (sec)	181.7	141.1	129.5	130.6	127.0	130.6	130.5	130.7
Ttl. RSS Err. (deg)	47.84	37.97	23.45	32.63	10.86	15.71	11.64	18.85
Ttl. RMS Err. (deg)	1.084	1.127	0.470	0.920	0.217	0.441	0.234	0.531
# Near-Sing.	18	2	0	1	17	3	2	2
Avg. Sing. Measure	0.404	0.618	0.502	0.653	0.556	0.473	0.493	0.660

left in the collect phase to get least-squares-close to preferred gimbal angles. This situation can leave the gimbals in less than favorable positions and hinder operations. Therefore, the requirement for the controller to be able to maintain pointing accuracy once first achieved is stressed by this experiment. The LB and QF controllers succeed in maintaining the required pointing accuracy throughout the mission during hardware experiments with null motion. Error statistics for all hardware experiments with null motion are worse than the corresponding values run without null motion, from Table 4.2, due to the disturbance torque imparted by gimbal null motion. However, the larger benefit of using null motion with the RWCMG system is with singularity avoidance which will be explained further in Section 4.3.4. First we will look at the results of the various preferred gimbal angle determination methods to see if better gimbal angles yield faster slew times or improvements in the singularity metrics.

4.3.3 Preferred Gimal Angle Impact on Null Motion.

Three methods of determining preferred gimbal angles for the analytical simulation are explained in Section 3.2.8: Offline, SQP, and Vadali [2]. The Offline and Vadali

methods are used on the hardware experiments. A listing of the metrics for each method is shown in Table 4.5. The LB controller is used for this analysis. The columns for the Vadali method contain the same metrics from the LB columns of Table 4.4 since the Vadali method was used for the controller analysis. Analysis of the preferred gimbal angle determination methods shows that null motion seeking angles calculated offline through pseudo-spectral optimization results in a 4% lower total RSS than null motion seeking Vadali preferred angles in hardware experiments, but do not necessarily improve the performance in the other statistics from Table 4.2. In the simulation with offline optimized preferred angles, the gimbals are stopped in a near-singular condition during collection of target one. Since the null motion of four gimbals with four degrees of freedom is only capable of reaching least-squares-close to the preferred values, the faster slew times sought from the offline optimization is not achieved. The analytical SQP technique decreased the error metrics by 1% compared to the simulation using Vadali angles, however the SQP produced worse completion time and singularity metrics than the other methods of Table 4.1. Note that the metrics generated thus far have all been run with initial gimbal angles in favorable positions. Whether set at Vadali angles or optimized angles, the initial condition of every run thus far, including the runs without null motion from Section 4.1 has been low-risk in terms of gimbal singularities. The next section tests the RWCMG system with null motion when the CMG gimbals start the mission in a less favorable condition.

4.3.4 *Initial Gimbal Angle Impact on Null Motion.*

In situations when agile satellite operators receive a high priority impromptu mission the gimbal angles may not currently be in such advantageous conditions as the cases studied thus far. For situations where the gimbal angles start in a near-singular condition, the control scheme must navigate around or through this singularity to deliver the desired control torque. In a system which has large CMG gimbals and rotors, the large inertia of the control system dictates relatively small gimbal rates. Thus if a pyramid of CMG gimbals

126

Table 4.5: Comparison of Preferred Gimbal Angle Determination Techniques - Analytical Simulation (A) and Hardware Experiment (H)

	Offline		SQP	Vadali	
	A	H	A	A	H
Completion Time (sec)	127.4	130.8	128.1	127.0	130.6
Total RSS Error (deg)	10.83	15.09	10.67	10.86	15.71
Total RMS Error (deg)	0.217	0.424	0.214	0.217	0.441
Number of Near-Singularities	114	12	21	17	3
Average Singularity Measure	0.524	0.550	0.475	0.556	0.473

are resting in a near-singular configuration they may stay near that singularity for a large portion of the mission. Null motion with the RWCMG actuation scheme can eliminate that risk. Though the SimSat gimbals are smaller than those of agile imaging s/c, experiments with the gimbals starting in a near-singularity show the ability of the null motion scheme to improve singularity avoidance performance. For the SimSat configuration where the gimbal angles at the start of the mission δ_s are $[90°, -90°, 90°, -90°]$, the initial singularity measure ν is near-zero. RWCMG runs starting gimbal angles in the disadvantageous δ_s condition illustrate the benefit of using null motion to seek preferred gimbal angles. First, a δ_s baseline run with combined CMG and reaction wheel actuation but no null motion is run. Next, the same poor initial gimbal configuration is run with null motion as described above, seeking Vadali [2] preferred angles for targets two through four. One more run is made with δ_s for target one and null motion seeking the offline optimized gimbal angles. Results of these three hardware experiments are shown in Table 4.6.

The RWCMG hardware experiment ran with null motion and Vadali preferred gimbal angles results in a 5% reduction in total RMS error and 6% improvement in average

Table 4.6: Null Motion Impact when Gimbals Start in Near-Singular Condition - Hardware Experiment

	No Null Motion Baseline	Null Motion with Vadali Pref. Angles	% Impr. from Baseline	Null Motion with Offline Pref. Angles	% Impr. from Baseline
Compl. Time (sec)	131.2	131.4	(-)	130.1	(0.8%)
Ttl. RSS Error (deg)	15.36	14.50	(5%)	14.32	(6%)
Ttl. RMS Error (deg)	0.432	0.408	(5%)	0.401	(7%)
# of Near-Sing.	6	5	(16%)	5	(16%)
Avg. Sing. Measure	0.491	0.524	(6%)	0.645	(31%)

singularity measure value over the case with no null motion when the gimbals are started in a singular condition. A small reduction in completion time and a 31% improvement in average singularity measure value are achieved with the use of null motion toward offline preferred gimbal angles. Overall, the use of null motion during collect mode is beneficial to the RWCMG representative mission when the gimbal angles are not initialized to advantageous values prior to the first slew.

4.3.5   RWCMG Actuation Compared to Traditional CSCMG.

The final analysis to characterize the RWCMG system is to compare performance with the current system in use. As mentioned in Chapter I, imaging satellites currently use control moment gyroscope arrays without the benefit of added reaction wheels. A pyramid of four CSCMG is thus the baseline for this analysis. Hardware runs with the AFIT SimSat platform using CMG-only actuation is compared against the RWCMG system, trading parameters studied above: choice of controller and starting gimbal angles. The results are shown in Table 4.7.

Traditional control schemes using a PID controller and a pyramid of CSCMG actuators have slower completion times, suffer higher pointing error, and encounter more singularity

Table 4.7: Comparison of CSCMG and RWCMG Actuation with Various Starting Conditions and Controllers - Hardware Experiment

Initial Gimbal Angles	δ_s				Vadali	
Controller	PID		LB		LB	
	CSCMG	RWCMG	CSCMG	RWCMG	CSCMG	RWCMG
Completion Time (sec)	149.2	142.8	134.3	131.4	130.8	130.6
Total RSS Error (deg)	36.19	39.46	14.21	14.50	14.57	15.71
Total RMS Error (deg)	1.101	1.182	0.404	0.408	0.409	0.441
Number of Near-Singularities	67	23	28	5	1	3
Average Singularity Measure	0.425	0.443	0.466	0.524	0.533	0.473

problems than the RWCMG system. However, starting the gimbal angles in a favorable position before the mission starts does significantly improve performance regardless of the actuation scheme. When gimbal angles start the representative mission in the near-singular δ_s configuration, the RWCMG system results in a 5% decrease in overall mission completion time with PID controllers compared to the traditional CSCMG system. Total RSS error increases by 9% with use of the RWCMG system and PID controllers due to disturbance torque. While the CSCMG system suffers 67 near singularities when the gimbal angles start in δ_s, the RWCMG system drops that number to 23 and improves the average singularity measure metric by 4%. When examining the case of using the LB controller with initial gimbal angles set to δ_s, the RWCMG system improves completion time by 2% compared to the traditional CSCMG system. The number of near singularities drops from 28 to five and the average singularity measure is improved by 12% with the RWCMG system and LB controller compared to the CSCMG system with LB controller. When gimbal angles start the mission in the Vadali preferred angles, no benefit in metrics

is measured. The statistics observed above apply to the specific representative mission set used in the dissertation research.

With three extra reaction wheel actuators, the RWCMG system is capable of placing gimbals in favorable positions without the use of non-renewable fuel consumed by thrusters which might be used on a CSCMG system. The LB controller generally reduces total RSS and RMS error compared to the PID controller by over 50%. The RWCMG actuation scheme generally improves the average singularity measure over the CSCMG scheme by 12-45% depending on the controller selected, unless gimbal angles are already set in a favorable condition at the start of the mission. When the RWCMG system is used without null motion, as in Table 4.2, total RSS error is 2% lower than the CSCMG system. Thus, the RWCMG system offers the capability to choose to use null motion to improve singularity metrics at the cost of slight pointing accuracy degradation, or use the RWA for collection without performing CMG gimbal null motion for increased pointing accuracy. In terms of the mission completion time, the representative mission used for this presented research consists of 108 seconds of dwell time during collection. If the required 108 seconds of dwell time is taken out of the mission completion time metric, the gains achieved by the RWCMG system are seen as applying to s/c slews only. Along this line of reasoning, the RWCMG system improves mission slew times by over 19% for the PID-controlled experiment with δ_s initial gimbal conditions and 11% for the LB controller with the same initial gimbal condition. Mission slew times improvements are negligible with the RWCMG system for the case with Vadali initial gimbal angles. Further collection of data to make statistically significant assertions in this experiment is a recommended item for future research in Chapter V.

In many of the representative mission runs for this section the differences in metrics are small. Differences seen in the RMS metric in particular is of a relatively small order of magnitude in many runs. Therefore, filtering techniques can be useful to

130

ensure measurement and dynamic noise are properly accounted for in developing metrics. The following section discusses results of filtering techniques applied to the analytical simulations.

4.4   Stochastic Estimation Performance Evaluation - Analytical Only

Sections 2.7 and 3.2.6 presented the equations and use of the EKF and UKF filters in the analytical closed-loop control scheme. The EKF and UKF are not implemented in the hardware experiments due to lack of external devices for recording dynamic attitude and spacecraft angular rate measurements. SimSat does have a means of filtering what McFarland calls "isolated gyro corruption" [32]. Through the use of a low-pass filter McChesney diminished the effect of spikes in the SimSat LN-200 IMU spacecraft angular rate measurements. This filtering method results in IMU measurements with adequate accuracy for the duration of each RWCMG mission. The IMU is re-zeroed between each RWCMG experiment to ensure consistency.

Results for the EKF and UKF applied to the RWCMG analytical closed-loop control scheme are shown below in terms of ensemble mean error and average ensemble RSS error with respect to the truth signal. Standard deviation is shown on the RSS of ensemble mean error plots as dashed lines for each filter. The setup for the filter analysis includes the LB controller, null motion using the Vadali [2] preferred gimbal angles, and 100 Monte Carlo runs with normally distributed measurement and dynamics noise. Figure 4.23 shows mean error of the ensemble for the quaternion states. An RSS of the mean error value for each filter and state is shown in the legend. Application of the EKF results in a smaller standard deviation than the UKF, however the UKF results in a slight advantage in mean error and overall RMS values for quaternions during the RWCMG mission runs. The UKF gains this advantage during many of the slew modes, out-performing the EKF during periods of faster spacecraft motion. Mean error and standard deviation plots for the s/c angular rate states are shown in Figure 4.24. The same pattern of performance is seen with the angular rate
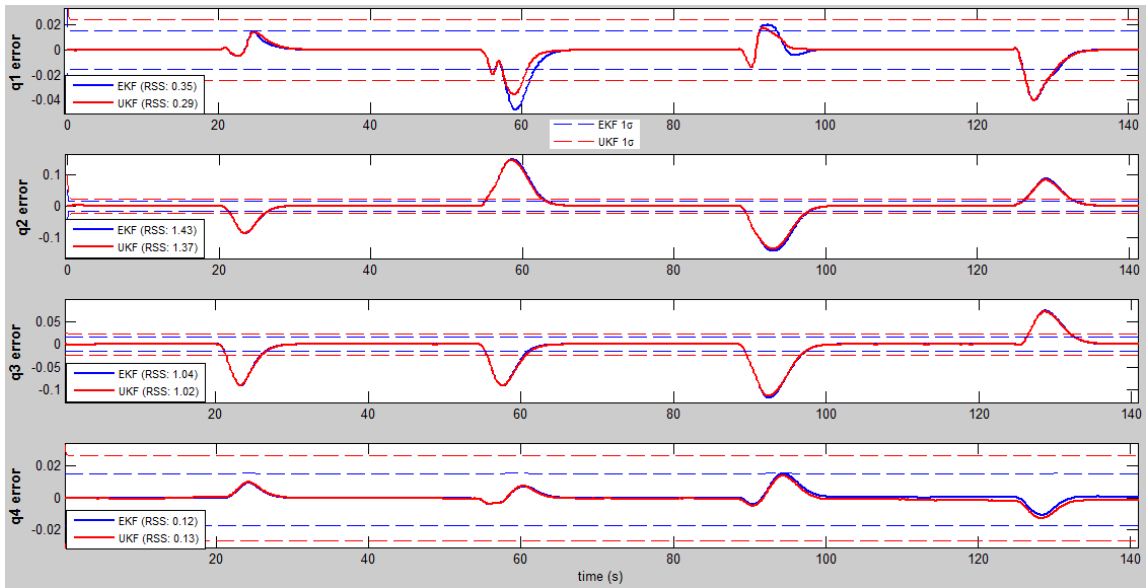
131

Figure 4.23: Quaternion Mean Error (Ensemble) for EKF and UKF 100 Monte Carlo Runs - Analytical Simulation
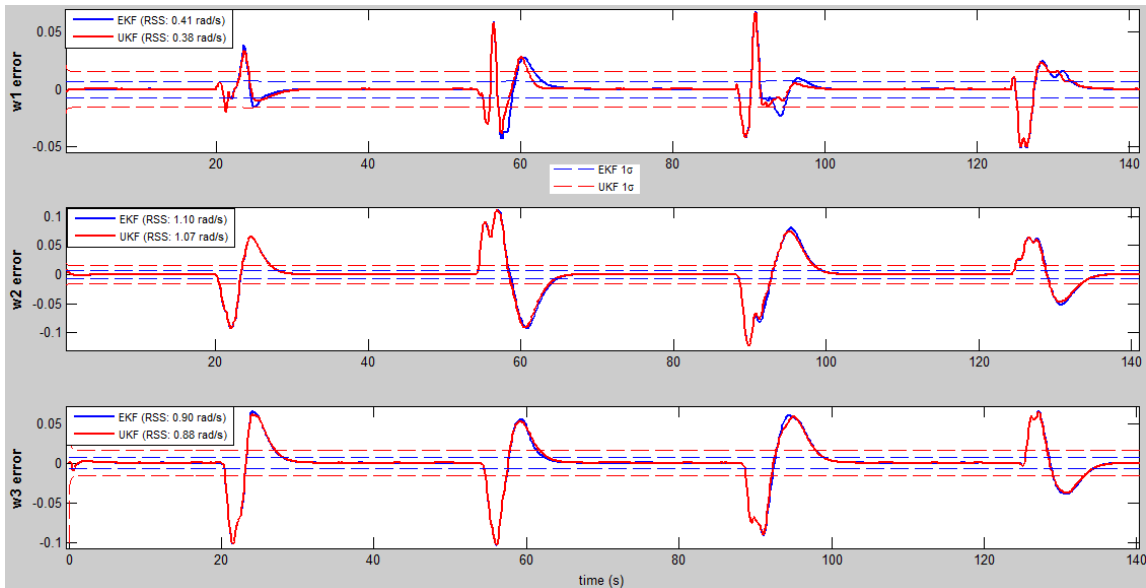

Figure 4.24: Angular Rate Mean Error for EKF and UKF 100 Monte Carlo Runs - Analytical Simulation

132

states as with the quaternions. The UKF performs slightly better during slew mode than the EKF. Standard deviation is smaller with the EKF. Figures 4.25 and 4.26 show average ensemble RSS error plots for the seven filtered states for each filter.   Except for q_4, the

Figure 4.25: Quaternion Average Ensemble RSS Error for EKF and UKF 100 Monte Carlo Runs - Analytical Simulation

UKF results in lower RSS during slews. Therefore, the overall performance during slew modes favors the UKF over the EKF. No clear performance advantages are discernible on the spacecraft angular rate RSS plots. The conclusion of this study is that the UKF is a slightly better filter during slew modes and the EKF is a slightly better filter during collect modes. Since the UKF is approximately 6% slower in terms of computation times (based on Monte Carlo run times) the recommendation based on this research is to use the EKF during non-mission time for a satellite and during collect modes; and switch to the UKF during slew modes if greater measurement accuracy is required. This concludes the results chapter. Chapter V will discuss overall conclusions based on the research project, explain contributions to the field, and recommend topics for future research.
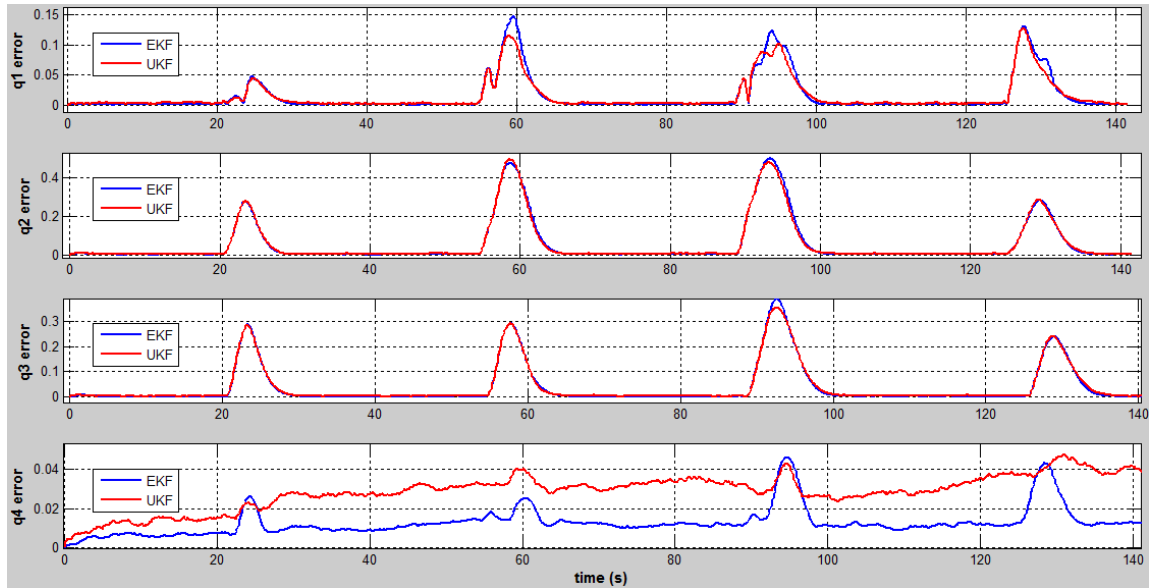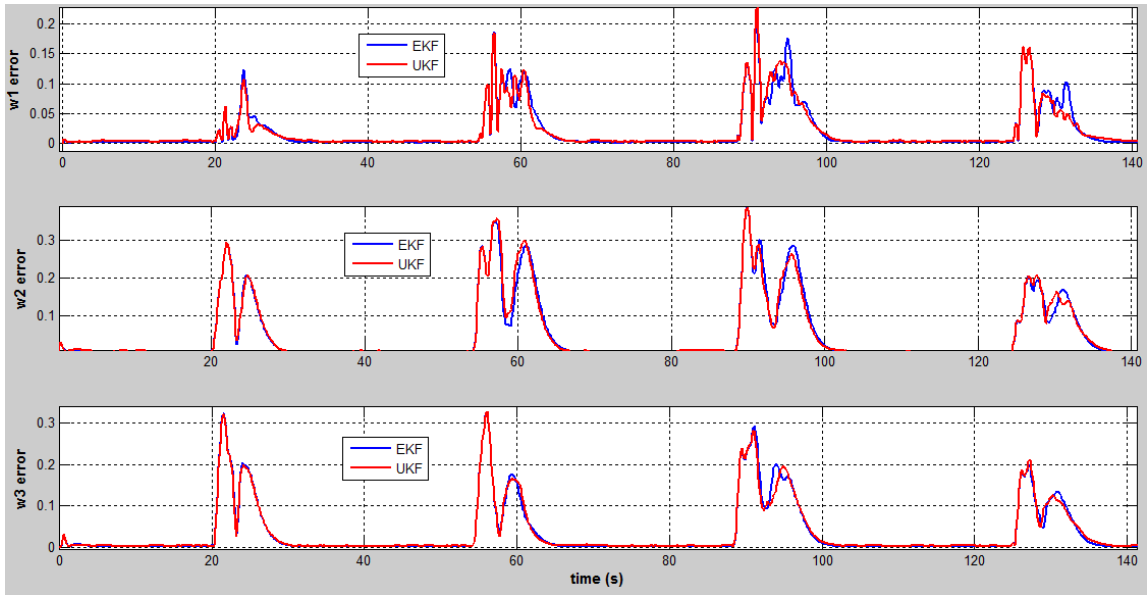
Figure 4.26: Quaternion Average Ensemble RSS Error for EKF and UKF 100 Monte Carlo Runs - Analytical Simulation

V.   Conclusions

This chapter presents an overview of the research on combined CMG and RWA (RWCMG) actuation for agile spacecraft. Analytical simulation and hardware experiments were conducted to characterize RWCMG performance over a representative target field. Metrics were used to assess RWCMG performance in areas such as mission completion time, pointing error, and singularity avoidance parameters. Chapter I provided an explanation of the s/c actuation problem and introduces the research areas pertaining to the problem. Boundaries of current research in the research areas were presented in Chapter II. The RWCMG analytical and experimental closed-loop control scheme methods were explained in Chapter III. Results of simulation and hardware experiments were presented in Chapter IV. Conclusions drawn from the RWCMG research are presented in Section 5.1 below. Contributions to the field are listed in Section 5.2. The chapter concludes with recommended topics for future research in the field of RWCMG optimal s/c control.

5.1   Research Conclusions

Agile spacecraft imaging missions require the s/c to have the ability to quickly slew from one target to the next, and when collecting imagery on a target, pointing accuracy requirements must also be met. Traditional s/c control systems use one set of actuators to accomplish both functions. This presented research explores a combined CMG and RWA actuation system for an agile s/c through analytical simulation and hardware experiments. The relatively high torque of CMG arrays is used for the slew function, while the relatively high pointing accuracy of the RWA is used for the collect function. With a surplus of actuators, CMG gimbals may travel null motion trajectories toward preferred values during collection and the reaction wheels can also be used for singularity avoidance.

5.1.1 *RWCMG Research Areas.*

Eight research areas are required in the development of this RWCMG system. These eight areas are:

- Multi-target Collection

- Variable Speed CMGs

- Applicable Controllers

- Singularity Avoidance

- Null Motion

- Stochastic Estimation

- Preferred Gimbal Angles

- Applied Optimization

Previous research with multi-target s/c tracking provides recommendations for controller singularity avoidance schemes. Variable speed CMG theory serves as a background in developing the equations of motion for a RWCMG system; however no VSCMG systems have been demonstrated in hardware to date. Three controllers are selected for investigation with the RWCMG system: PID, QF, and LB. Singularity avoidance techniques are required when using CMG actuation and are facilitated with the addition of RWA actuation components. Null motion of CMG gimbal angles requires equations which impart minimal residual torque to the s/c while achieving the closest fit to the solution as possible during the collection window. Stochastic estimation techniques afford improved measurement accuracy for s/c states. Preferred gimbal angle theory suggests that angles may be calculated off-line through optimization or backward integration techniques - both of which are applied with the current RWCMG research. Finally, the applied optimization

area is used for several applications with the presented research: benchmarking, preferred gimbal angle calculation, and maximum torque calculation. These eight research areas are applied throughout this research. In the cases of preferred gimbal angles and null motion, the research is expanded through numerical simulation and experiments with the AFIT SimSat hardware. Simulation and experiments for characterization of the RWCMG system requires use of closed-loop control schemes which are discussed next.

5.1.2 RWCMG Closed-Loop Control Scheme.

Analytical simulation of the RWCMG representative mission is executed via a closed-loop control scheme with eight major components as shown in Figure 3.3. First, several parameters must be calculated including quaternion error, rotation matrices, and angular momentum. Next, a selected controller calculates the desired control torque. Singularity avoidance parameters must be computed next which feed into a limit enforcement function. This limit enforcement function attempts to impose constraints on the numerical simulation states which are derived from actual hardware limitations. Next, the steering laws are applied to compute noise-free derivatives. The null motion of gimbal angles occurs in the steering law step if the s/c is in collect mode. EKF or UKF stochastic filters are applied at the next step, providing updated versions of the filtered states based on noisy measurement signals. In the mission progress block, if the s/c is in slew mode, then progress toward meeting pointing accuracy requirements for the next target is monitored. If in collect mode, the progress toward meeting the required dwell time is computed. The final step of the analytical closed-loop control scheme is to compute preferred gimbal angles. This last step only occurs once per target at the start of each collect mode.

Converting the analytical RWCMG closed-loop model to the hardware platform model of Figure 3.4 requires elimination of the limit enforcement function since the hardware already has constraints based on physical limits. Other changes include the addition of the attitude determination function, and removal of the filtering step due to lack of external

137

dynamic measurement devices. Hardware experiments revealed the need for shortest-path gimbal null motion logic when seeking preferred values. The shortest-path gimbal null motion logic is a contribution of this presented research not known by the author to exist in the literature and is illustrated in Figure 3.5.

5.1.3 Controller and Limit Enforcement Performance.

Evaluation of RWCMG simulation and experiment components is accomplished through the study of five primary metrics: mission completion time, total RSS pointing error, total RMS pointing error, number of near-singularities, and average singularity measure. These metrics are defined further in Section 3.5. The first component evaluated is the choice of controller. The PID, QF, and LB controllers are tested in simulation and hardware experiments. A fourth controller derived from a combination of the QF and LB controllers is also evaluated. For both simulation and experiment, application of the PID controller results in mission completion times approximately 10-40% slower and error metrics approximately 150-300% worse than the LB controller. During simulations, the PID controlled mission fails to maintain pointing accuracy standards after the target first comes into view. This behavior means the PID controller is not feasible for use with the SQP preferred gimbal angle calculation technique. The LB controller provides the shortest mission completion times and lowest pointing error due to the inclusion of a nonlinear term in the LB controller which assists with tracking moving targets. The QF controller produces the highest average singularity avoidance measure of all controllers. While the intent with investigating the CB controller was to use the advantage of the LB controller on dynamic axis tracking and the advantage of the QF controller on static s/c axes, the simulation and experimental results did not show improved performance with the CB controller compared to the others. Results of the controller comparisons are found in Section 4.1.

The second component of the RWCMG research evaluated is the limit enforcement function for the analytical simulation. Plots of spacecraft angular rates, CMG gimbal

138

rates, and CMG gimbal acceleration show that the limit enforcement function reduces the constraint violations by 100%, 94%, and 97%, respectively, for those s/c states compared to running the simulation without the limit enforcement function active. However, relatively small constraint violations still occur with the limit enforcement function turned on. The likely reason for this small constraint violation is the required use of the pseudo-inverse in the equations of motion. Analytical simulations run with the limit enforcement function - which matches hardware limits - active produce results much closer to those seen in hardware experiments. Discussion of limit enforcement results is found in Section 4.1.2. With the analytical simulation sufficiently limited to resemble hardware limitations, evaluation of the various aspects of RWCMG null motion may begin.

5.1.4 Null Motion and Preferred Gimbal Angle Performance.

The first aspect of null motion and preferred gimbal angles to be discussed is gain tuning. Null motion gain determines how fast the gimbals travel along the null motion trajectories toward the preferred angles. Hardware experiments show that the gain can be adjusted to scale the amount of time the gimbals take to reach least-squares-close to the preferred values. When the gimbals reach values which are least-squares-close to the preferred values, no further gimbal motion occurs. If the null motion gain is too, low the gimbals do not reach least-squares-close and continue to rotate until the next slew starts. Hardware runs also indicate that although suffering a higher initial impulsive disturbance, an overall lower level of disturbance torque is imparted on the s/c when the null motion gain is high rather than low which may seem counterintuitive to engineering judgment. With the former case, the gimbals quickly rotate to the least-squares-close values, imparting a relatively large disturbance torque but over a short period of time. As long as the large disturbance torque does not cause a violation in pointing tolerance or cause too much jitter, the total level of disturbance over the collection period is shown to be lower than the case of a smaller disturbance torque over a longer period of time. Further discussion on null

motion gain tuning is presented in Section 4.3.1. With the null motion gain tuned to a level which ensures gimbals reach least-squares-close to preferred values and avoids causing disturbances which violate pointing tolerance, an assessment of the RWCMG with null motion turned on can begin. The first aspect of the system evaluated with null motion active is the selection of controllers.

Controllers are compared a second time, now with null motion and preferred gimbal angles active. The same performance trends noted in the original controller evaluation are witnessed in the tests with null motion. The LB controlled experiment produces the fastest mission completion time with the lowest error. The PID controlled experiment produced the worst performance with null motion active compared to without due to its inability to maintain pointing accuracy requirements throughout collection. The LB and QF controlled experiments with null motion produce mission completion times faster than the missions run without null motion. Controller evaluation with respect to RWCMG null motion is found in Section 4.3.2. The next aspect of the RWCMG system related to null motion is an evaluation of techniques for calculating preferred gimbal angles.

Recall that the desired operation of the RWCMG system is to have the CMG array slew the s/c to a target, and then the RWA assumes control during collection on that target. During that collection period, CMG gimbals are rotated along null motion paths toward preferred angles. Evaluation of preferred gimbal angle computation techniques (offline optimization, SQP (analytical only) and Vadali [2] lookup) is presented next. Experimental results demonstrate a 7% improvement in average singularity measure and a 5% decrease in number of near-singularities noted using the Vadali preferred angles over the case with no null motion. Null motion seeking angles calculated offline through pseudo-spectral optimization results in a 4% lower total RSS than null motion seeking Vadali preferred angles but does not result in faster mission completion times. A possible cause for not achieving shorter mission times with the preferred gimbal angles optimized to do so is

the fact that the CMG gimbals do not reach those optimal values. Null motion of four CMG gimbals in four degrees of freedom only allows the gimbals to get least-squares-close to the optimal angles, thus the potential benefits of specifically optimized angles is not realized. Analytical simulation with SQP gimbal angles results in a negligible decrease in the error metrics compared to the simulation using Vadali angles and does not improve the other metrics for the same reason the offline preferred angles did not improve mission time. Another possible cause for not achieving shorter mission times with preferred gimbal angles is the case when the CMG array provides the highest level of torque allowed by constraints regardless of the null motion. If the CMG gimbals are able to provide maximum torque from their current configuration, then no amount of null motion will improve the slew time. Results of preferred gimbal angle experiments and simulations are found in Section 4.3.3. All null motion experiments and simulations to this point are conducted with the s/c gimbals in favorable positions at the start of the mission - either Vadali angles or set exactly at optimized angles. When conducting an agile s/c mission, the gimbals angles may not be in such advantageous configurations at the start of the mission. The next evaluation tests RWCMG performance when CMG gimbals start in a non-favorable configuration.

Performance of the RWCMG system when the CMG gimbals start in a near-singular condition is evaluated in Section 4.3.4. Compared to the baseline case in which the RWCMG system runs without null motion, cases run using null motion with Vadali preferred angles results in a 5% improvement in error metrics and a 6% improvement in singularity metrics. Using preferred gimbal angles calculated offline with PS optimization, the RWCMG system achieves a 0.8% improvement in mission completion time 6% improvement in error metrics and 31% improvement in average singularity measure value. Overall, we find that the use of RWCMG null motion during collect mode improves performance when gimbal angles do not begin in favorable positions at the start of the

mission. With comparison of the RWCMG system with null motion to the RWCMG system without null motion, the final hardware experiment in this research on assessing RWCMG performance is to compare the system with a traditional pyramid of four CSCMGs.

5.1.5 RWCMG System Performance.

Unless gimbal angles are already set in a favorable condition at the start of the mission, the RWCMG actuation scheme generally improves the average singularity measure over the CSCMG scheme by 12-45%, depending on the controller selected. Total RSS error is 2% lower than that of the CSCMG system when the RWCMG system is used without null motion. The RWCMG system offers the capability to choose to use null motion to improve singularity metrics at the cost of slight pointing accuracy degradation, or use the RWA for collection without performing CMG gimbal null motion for increased pointing accuracy. For our scenario, if the required 108 seconds of imaging dwell time is taken out of the mission completion time metric, the gains achieved by the RWCMG system are seen as applying to s/c slews only. Along this line of reasoning, the RWCMG system improves mission slew times by over 19% for the PID controlled experiment in which gimbals start in an unfavorable condition. The RWCMG LB controlled experiment with unfavorable initial gimbal angles reduces slew times by 11% compared to the CSCMG system with LB control. Mission slew time improvement is negligible with the RWCMG system for the case with Vadali initial gimbal angles. Overall, the RWCMG system is found to improve mission completion time by up to 5% and singularity avoidance parameters by up to 45% over traditional constant-speed CMG systems. When omitting imagery collection times, the RWCMG system improves s/c slew times by up to 19% compared to traditional CMG systems.

Stochastic filters are tested with analytical simulation for the RWCMG system. The UKF produced slightly better error metrics than the EKF during slews. The EKF had lower standard deviation than the UKF. Since the UKF computation time is approximately

6% slower than the EKF and performance metrics are comparable during collect mode, a filtering system which uses the EKF for collection and UKF for slews is recommended. However, since filter performance does depend on the situation, more research in stochastic estimation associated with the RWCMG should be done in this area.

5.2 Contributions

The presented dissertation research makes several contributions to the field of optimal s/c attitude control.

1. Analytical simulation and hardware experiment closed-loop control schemes for the RWCMG system were developed and implemented using a representative agile s/c mission. A method for transitioning between CMG and RWA controllers was tested.

2. A new controller consisting of parts of exiting quaternion feedback and nonlinear Lyapunov-based controllers was tested for the RWCMG application. This combined controller showed potential for gaining the pointing accuracy benefits from the Lyapunov-based controller and the singularity avoidance benefits from the quaternion feedback controller.

3. An improvement to existing null motion equations was made in development of CMG gimbal shortest path logic. The new logic forces CMG gimbals to travel null motion trajectories which generate smaller disturbance torque on the s/c due to shorter distances travelled.

4. A method of characterizing disturbance torque was developed. The Disturbance Torque Score measures the overall level of disturbance torque which CMG null motion causes on the s/c by comparing RWA rates with and without the null motion. Hardware experiments revealed that the faster the CMG gimbals travel null motion trajectories and settle on least-squares-close value, the larger the initial impulse disturbance, but the lower the overall aggregate disturbance torque on the s/c.

5. Hardware experiments were conducted to compare the RWCMG control system to a traditional constant-speed CMG system. Improvements in slew times, pointing accuracy, and singularity avoidance were observed with the RWCMG system for the representative agile s/c mission and encourage further research in area.

5.3 Future Work

The presented research on RWCMG actuation covers a wide range of research areas of which eight were specifically broken out and covered in detail. This area of research shows promise and more research is recommended to realize the full potential of such a system. Several aspects of the research offer options for future research. Four general aspects of the RWCMG research which contain topics are closed-loop control scheme setup, optimization, null motion, and hardware experiments.

5.3.1 *Future Research Aspect: Closed-Loop Control Scheme Setup.*

The first suggested research topic is further refinement of controller gains in the closed-loop control scheme. Gains for the presented research are set based on equations which produce specific values for damping and natural frequency which help ensure fair comparisons between different controllers to determine which ones yield the best performance. Despite use of these gain equations, the PID controller failed to maintain pointing accuracy requirements during collection phases of the analytical closed-loop control scheme. Loss of pointing accuracy tolerance during the PID controlled simulation caused the mission completion time to be higher than the corresponding hardware experiment. All other controllers resulted in faster simulated mission completion times than the corresponding hardware experiment. Further research into gain adjustment for the analytical PID controller may bring simulated results closer to hardware results and yield improved RWCMG performance.

The second suggested research topic in the closed-loop control scheme aspect is further research into limit enforcement techniques. The Limit Enforcement algorithm of

Figure 3.3 significantly reduced violations of desired constraints, however small violations still occurred in the analytical simulations. These small violations are a likely cause for analytical simulation result deviance from hardware experiments. As explained in Section 4.2, the required use of the pseudo-inverse in the state equations of motion is a probable cause for the violations. Further research into the cause of constraint violations with the Limit Enforcement algorithm and corrections to eliminate the violations would provide a significant increase in fidelity to RWCMG analytical simulations. Embedding the application of limits within the filter/propagate stage of the closed-loop control scheme may allow further manipulation of states and improve accuracy as well.

5.3.2   *Future Research Aspect: Optimization.*

Now transitioning to the optimization aspect of the RWCMG research, the next suggested topic is tuning of the cost function scaling parameter α in Eq. (3.3). This cost function is used for offline PS optimization with the purposes of benchmarking and initial gimbal angle calculation. The scaling parameter α adjusts how much of the cost function is based on pointing error versus the final time of the mission. For this presented research, α is set based on knowledge of the approximate number of collocation points for the optimization runs - knowledge gained through previous attempts at running the optimization. Since α adjusts scaling for a running pointing error term (summed error over the time span of the optimization) the magnitude of the error term is dependent on the number of time steps or collocation points in the PS optimization. If optimization mesh tolerance is set at levels which cause multiple mesh iterations, the number of collocation points increases and the magnitude of the point error term increases. Thus for this presented research, mesh tolerances for the RWCMG problem were carefully monitored and set based on a history of PS optimization runs. The approximate magnitude of the pointing error term of the cost function Eq. (3.3) was then known and the scaling parameter α was set to make the final time magnitude the greater value since the goal with the PS optimization

145

is to achieve the shortest mission time possible. Research into better ways to scale the PS optimization cost function would prevent future engineers from having to perform multiple optimizations to characterize the problem prior to finding a suitably scaled solution.

The second topic for research in the optimization aspect of RWCMG systems is to apply the 'traveling salesman' optimization logic to the problem. The traveling salesman problem refers to a system which is able to import a set of impromptu targets and use optimization techniques in-flight, to determine the best order of those targets while staying within prescribed constraints. Current research at AFIT applies traveling salesman to aircraft applications but the problem has not yet been applied to a RWCMG satellite attitude control scheme [60]. Wrapping in-flight optimization of target order to the RWCMG system would greatly enhance the agility of the imaging s/c and work synergistically with gimbal angle optimization performed in this research.

5.3.3 Future Research Aspect: Null Motion.

Moving on to the null motion aspect of the RWCMG system, the next suggested topic for research is tuning the transition time between CMG and RWA actuation when collect mode starts. The transition time for this presented research was a hard-coded length of time over which the CMG array torque is linearly decreased and the RWA torque is linearly increased. The purpose of the transition time is to avoid RWA saturation as the s/c settles on the current target. Research into nonlinear methods of transition has not been done. In addition, equations could be developed to set the length of transition time based on factors such as disturbance torque or component power requirements. Future research into refinement of the CMG to RWA transition time could further improve the performance of a RWCMG system.

A second topic for research in the null motion aspect of the RWCMG system is development of a mathematical model to study the effect of adding N number of additional control actuators on the ability to seek preferred gimbal angles. Many spacecraft have

multiple payloads which are independently controlled. If each of these payloads is factored into the RWCMG control scheme from this presented research, the null space would grow and theoretically improve the capability to achieve preferred gimbal angles. Research which characterizes the benefits to null motion of gimbal angles as the number of actuators is increased would give s/c designers a new tool with which to make hardware decisions and plan operations.

5.3.4   *Future Research Aspect: Hardware Experiments.*

The final aspect of the RWCMG system is hardware experiments. Section 3.2.8 presented the SQP near real-time method for calculating preferred gimbal angles. This optimization technique is only applied in the analytical closed-loop control scheme in the presented research. Application of the technique to hardware experiments has not been done. A method for using the SimSat minibox to run the SQP optimization during the first few real-time seconds of each collect mode and pass the preferred gimbal angle solutions to the real-time controller would allow an assessment of the SQP technique. Adding additional processing hardware to SimSat would improve the SQP performance because it would allow the optimization to process more computations in the limited time window before null motion starts.

The second hardware-related topic for research is implementation of the EKF and UKF for RWCMG hardware experiments. An external laser-based attitude measurement system is currently on order for SimSat. When the new system arrives, application of the EKF and UKF tested in the RWCMG analytical closed-loop control scheme from this presented research can be applied to hardware experiments. The new system could also provide a 'truth' signal with which to update the SimSat onboard IMU during missions which require a large set of targets or long time spans.

The final topic for research is to gather more hardware data runs for a statistical analysis of RWCMG results. Unlike analytical simulation, multiple hardware experiments

run with the same problem setup do not result in the same exact solution every time. Factors such as static and dynamic balancing, air currents in the room, and battery power levels all contribute to deviations in performance not modeled in simulation. Multiple experiments run with the same problem setup, while monitoring factors such as balancing, air currents, and battery power levels would help to remove these sources of uncertainty from the solutions and produce more precise hardware results.

The RWCMG research conducted in this dissertation effort shows a potential for increasing agile spacecraft performance. While the author recognizes the technical challenge of supplying power to two actuator arrays, the addition of the RWA to a CMG pyramid could potentially reduce the size and power consumption of the CMG array to compensate. The addition of the RWA to a traditional CSCMG system also offers a level of redundancy and provide a higher mission assurance since only three actuator of any type are needed to control a s/c at a lower level of performance. RWCMG benefits to mission completion time, pointing accuracy, and singularity avoidance have been demonstrated through hardware experiments. Shortest-path null motion logic and null motion gain tuning experiments are not found in the literature to the knowledge of the author and are considered contributions of the research. Several topics for additional research are recommended to further investigate and improve the RWCMG system.

Bibliography

[1] F. A. Leve, "Matlab script: call_momentum_envelope_pm_v2 m-file," 2014.

[2] S. R. VADALI, S. R. WALKER, and H. S. OH, "Preferred gimbal angles for single gimbal control moment gyros," *Journal of Guidance, Control, and Dynamics*, vol. 13, no. 6, pp. 1090–1095, 11/01; 2014/01 1990, doi: 10.2514/3.20583; M3: doi: 10.2514/3.20583; 16. [Online]. Available: http://dx.doi.org/10.2514/3.20583

[3] M. Karpenko and M. Ross, *Implementation of Shortest-Time Maneuvers for Generic CMG Steering Laws*. American Institute of Aeronautics and Astronautics, 08/13; 2013/12 2012, 02; M1: 0; doi:10.2514/6.2012-4959; M3: doi:10.2514/6.2012-4959. [Online]. Available: http://dx.doi.org/10.2514/6.2012-4959

[4] Digital Globe, "WorldView-2," *http://www.digitalglobe.com/sites/default/files/DG*, no. October, pp. 1–2, 2009.

[5] ——, "World View- 3 World View- 3 Design and Specifications," pp. 1–2, 2014.

[6] ——, "World View- 1 World View- 1 Design and Specifications," no. September, 2007.

[7] W. J. Larson and J. R. Wertz, "Space mission analysis and design," Microcosm, Inc., Torrance, CA (US), Tech. Rep., 1992.

[8] H. Schaub and J. L. Junkins, *Analytical mechanics of space systems*. AIAA, 2003.

[9] ——, "Singularity avoidance using null motion and variable-speed control moment gyros," *Journal of Guidance, Control, and Dynamics*, vol. 23, no. 1, pp. 11–16, 2000.

[10] D. Kim, F. A. Leve, N. G. Fitz-Coy, and W. E. Dixon, "New startup method using internal momentum management of variable-speed control moment gyroscopes," *Journal of Guidance, Control, and Dynamics*, vol. 35, no. 5, pp. 1472–1482, 2012.

[11] H. Yoon and P. Tsiotras, "Spacecraft adaptive attitude and power tracking with variable speed control moment gyroscopes," *Journal of Guidance, Control, and Dynamics*, vol. 25, no. 6, pp. 1081–1090, 2002.

[12] H. Zhang and J. Fang, "Robust backstepping control for agile satellite using double-gimbal variable-speed control moment gyroscope," *Journal of Guidance, Control, and Dynamics*, pp. 1–8, 2013.

[13] W. H. Steyn, "A dual-wheel multi-mode spacecraft actuator for near-minimum-time large angle slew maneuvers," *Aerospace Science and Technology*, vol. 12, no. 7, pp. 545–554, 2008.

[14] A. V. Doroshin, "Attitude control of spider-type multiple-rotor rigid bodies systems," in *Proceedings of the world congress on engineering*, vol. 2, 2009.

[15] "Commercial satellite imaging market - global industry analysis, size, share, growth, trends, and forecast, 2013 - 2019," 2014.

[16] R. A. Weber and K. M. OConnell, "Alternative futures: United states commercial satellite imagery in 2020," *Department of Commercial, Commercial Remote Sensing Regulatory Affairs*, 2011.

[17] R. M. Schillinger, "The use of satellite imagery for domestic law enforcement," Ph.D. dissertation, Monterey, California: Naval Postgraduate School, 2013.

[18] P. Sutton, D. Roberts, C. Elvidge, and K. Baugh, "Census from heaven: an estimate of the global human population using night-time satellite imagery," *International Journal of Remote Sensing*, vol. 22, no. 16, pp. 3061–3076, 2001.

[19] B. C. Reed, J. F. Brown, D. VanderZee, T. R. Loveland, J. W. Merchant, and D. O. Ohlen, "Measuring phenological variability from satellite imagery," *Journal of vegetation science*, vol. 5, no. 5, pp. 703–714, 1994.

[20] "Satellite imaging corporation, woldview-2 satellite sensor," 2014.

[21] B. Wie, D. Bailey, and C. Heiberg, "Rapid multitarget acquisition and pointing control of agile spacecraft," *Journal of Guidance, Control, and Dynamics*, vol. 25, no. 1, pp. 96–104, 01/01; 2014/01 2002, doi: 10.2514/2.4854; M3: doi: 10.2514/2.4854; 08. [Online]. Available: http://arc.aiaa.org/doi/abs/10.2514/2.4854

[22] Y. Nanamori and M. Takahashi, "Steering law of control moment gyros using optimization of initial gimbal angles for satellite attitude control," *Journal of System Design and Dynamics*, vol. 5, no. 1, pp. 30–41, 2011.

[23] H. Bang, M.-J. Tahk, and H.-D. Choi, "Large angle attitude control of spacecraft with actuator saturation," *Control Engineering Practice*, vol. 11, no. 9, pp. 989–997, 9 2003.

[24] C. Li, K. L. Teo, B. Li, and G. Ma, "A constrained optimal PID-like controller design for spacecraft attitude stabilization," *Acta Astronautica*, vol. 74, no. 0, pp. 131–140, 0 2012.

[25] S. Seltzer, "A satellite digital controller or" play that PID tune again, sam," in *A collection of technical papers: proceedings, AIAA Guidance and Control Conference, San Diego, California, August 16-18, 1976*. American Institute of Aeronautics and Astronautics, 1976, p. 280.

[26] L.-L. Show, J. C. Juang, C.-T. Lin, and Y.-W. Jan, "Spacecraft robust attitude tracking design: PID control approach," in *American Control Conference, 2002. Proceedings of the 2002*, vol. 2. IEEE, 2002, pp. 1360–1365.

[27] B. Wie, *Space vehicle dynamics and control*. AIAA, 1998.

[28] J. Wright and E. Swenson, *Comparison of Statically Optimized Proportional-Integral-Derivative and Functionally Optimized Controllers*. American Institute of Aeronautics and Astronautics, 08/13; 2013/12 2012, 02; M1: 0; doi:10.2514/6.2012-4785; M3: doi:10.2514/6.2012-4785. [Online]. Available: http://dx.doi.org/10.2514/6.2012-4785

[29] M. Kemao, Z. Jiawei, and Y. Yafei, "Improved backstepping control for large angle maneuvers of spacecraft," in *Control Conference (CCC), 2012 31st Chinese*. IEEE, 2012, pp. 448–452.

[30] H. Kurokawa, "Survey of theory and steering laws of single-gimbal control moment gyros," *Journal of Guidance, Control, and Dynamics*, vol. 30, no. 5, pp. 1331–1340, 2007.

[31] R. A. J. Chagas and J. Waldmann, "Nonlinear filtering in a simulated three-axis satellite attitude estimation and control tested," *Journal of Aerospace Engineering, Sciences and Applications*, vol. 2, no. 2, pp. 37–49, 2010.

[32] C. D. McFarland, "Near real-time closed-loop optimal control feedback for spacecraft attitude maneuvers," 2009.

[33] D. Lee, C. G. Park, and H. Bang, "Gimbal angle reorientation for nonredundant single gimbal control moment gyros," 2013.

[34] Y. Kusuda and M. Takahashi, "Feedback control with nominal inputs for agile satellites using control moment gyros," *Journal of Guidance, Control, and Dynamics*, vol. 34, no. 4, pp. 1209–1218, 2011.

[35] D. Verbin and V. J. Lappas, "Rapid rotational maneuvering of rigid satellites with hybrid actuators configuration," *Journal of Guidance, Control, and Dynamics*, vol. 36, no. 2, pp. 532–547, 03/01; 2013/12 2013, doi: 10.2514/1.56405; M3: doi: 10.2514/1.56405; 02. [Online]. Available: http://dx.doi.org/10.2514/1.56405

[36] C. McChesney, "Design of attitude control actuators for a simulated spacecraft," 2011.

[37] B. Wie, "Singularity escape/avoidance steering logic for control moment gyro systems," *Journal of guidance, control, and dynamics*, vol. 28, no. 5, pp. 948–956, 2005.

[38] ——, "Singularity analysis and visualization for single-gimbal control moment gyro systems," *Journal of Guidance, Control, and Dynamics*, vol. 27, no. 2, pp. 271–282, 2004.

[39] B. Wie, D. Bailey, and C. Heiberg, "Singularity robust steering logic for redundant single-gimbal control moment gyros," *Journal of Guidance, Control, and Dynamics*, vol. 24, no. 5, pp. 865–872, 2001.

[40] H. Yoon and P. Tsiotras, "Singularity analysis of variable speed control moment gyros," *Journal of Guidance, Control, and Dynamics*, vol. 27, no. 3, pp. 374–386, 2004.

[41] H. Vadali, "Feedback control and steering laws for spacecraft using single gimbal control moment gyros," *The Journal of Astronautical Sciences*, vol. 2, pp. 183–203, 1991.

[42] T. Higuchi, S. Ueno, and T. Ohmura, *Singularity Avoidance Steering Logic for SGCMG Systems Using State Feedback*. American Institute of Aeronautics and Astronautics, 08/02; 2014/01 2010, 16; M1: 0; doi:10.2514/6.2010-8379; M3: doi:10.2514/6.2010-8379. [Online]. Available: http://dx.doi.org/10.2514/6.2010-8379

[43] L. L. Jones, R. A. Zeledon, and M. A. Peck, "Generalized framework for linearly constrained control moment gyro steering," *Journal of Guidance, Control, and Dynamics*, vol. 35, no. 4, pp. 1094–1103, 2012.

[44] Z. Sun, L. Zhang, G. Jin, and X. Yang, "Analysis of inertia dyadic uncertainty for small agile satellite with control moment gyros," in *Mechatronics and Automation (ICMA), 2010 International Conference on*. IEEE, 2010, pp. 813–818.

[45] T. Sands, J. J. Kim, and B. N. Agrawal, "Nonredundant single-gimbaled control moment gyroscopes," *Journal of Guidance, Control, and Dynamics*, vol. 35, no. 2, pp. 578–587, 2012.

[46] J. Wright, E. Swenson, F. Leve, and C. McChesney, *Hardware Testing of Hybrid Steering Logic for Single-Gimbal Control Moment Gyroscopes*. American Institute of Aeronautics and Astronautics, 08/13; 2013/12 2012, 02; M1: 0; doi:10.2514/6.2012-4971; M3: doi:10.2514/6.2012-4971. [Online]. Available: http://dx.doi.org/10.2514/6.2012-4971

[47] L. C. G. Souza and R. G. Gonzles, "Application of the state-dependent riccati equation and kalman filter techniques to the design of a satellite control system," *Shock and Vibration*, vol. 19, no. 5, pp. 939–946, 09 2012, m3: Article. [Online]. Available: http://search.ebscohost.com/login.aspx?direct=true&db=a9h&AN=80383158&site=ehost-live

[48] E. J. Lefferts, F. L. Markley, and M. D. Shuster, "Kalman filtering for spacecraft attitude estimation," *Journal of Guidance, Control, and Dynamics*, vol. 5, no. 5, pp. 417–429, 1982.

[49] S. J. Julier and J. K. Uhlmann, "A general method for approximating nonlinear transformations of probability distributions," Technical Report, RRG, Department of Engineering Sciences, University of Oxford, Tech. Rep., 1996.

[50] ——, "Consistent debiased method for converting between polar and cartesian coordinate systems," in *AeroSense'97*. International Society for Optics and Photonics, 1997, pp. 110–121.

[51] S. J. Julier, J. K. Uhlmann, and H. F. Durrant-Whyte, "A new approach for filtering nonlinear systems," in *American Control Conference, Proceedings of the 1995*, vol. 3. IEEE, 1995, pp. 1628–1632.

[52] S. J. Julier and J. K. Uhlmann, "A new extension of the kalman filter to nonlinear systems," in *Int. symp. aerospace/defense sensing, simul. and controls*, vol. 3. Orlando, FL, 1997, p. 3.2.

[53] J. Vitalich, "Design and simulation of a three-axis stabilized satellite and kalman filter rate estimator," Tech. Rep., JUN 2003.

[54] D. E. Kirk, *Optimal Control Theory An Introduction*. Mineola, NY: Dover Publications, 1970.

[55] J. S. Arora, *Introduction to Optimum Design*. Amsterdam: Academic Press, 2012.

[56] B. Fornberg, *A Practical Guide to Pseudospectral Methods*. Cambridge: Cambridge University Press, 1998.

[57] J. W. Wright, "Advancements of in-flight mass moment of inertia and structural deflection algorithms for satellite attitude simulators," 2015.

[58] "dSPACE company website," http://www.dspace.com/en/inc/home.cfm, accessed: 2015-10-30.

[59] P. Maybeck, *Stochastic Models, Estmiation and Control: Volume 1*. New York: Academic Press, 1979.

[60] N. M. Jodeh, "Optimal uas assignments and trajectories for persistent surveillance and data collection from a wireless sensor network," 2015.

153

REPORT DOCUMENTATION PAGE

1. REPORT DATE *(DD–MM–YYYY)*	2. REPORT TYPE	3. DATES COVERED *(From — To)*
17–12–2015	Dissertation	October 2012 - December 2015

4. TITLE AND SUBTITLE

Optimal Attitude Control of Agile Spacecraft Using Combined Reaction Wheel and Control Moment Gyroscope Arrays

5a. CONTRACT NUMBER

5b. GRANT NUMBER

5c. PROGRAM ELEMENT NUMBER

6. AUTHOR(S)

Doupe, Cole C., Major, USAF

5d. PROJECT NUMBER

5e. TASK NUMBER

5f. WORK UNIT NUMBER

7. PERFORMING ORGANIZATION NAME(S) AND ADDRESS(ES)

Air Force Institute of Technology
Graduate School of Engineering and Management (AFIT/EN)
2950 Hobson Way
Wright-Patterson AFB, OH 45433-7765

8. PERFORMING ORGANIZATION REPORT NUMBER

AFIT-ENY-DS-15-D-042

9. SPONSORING / MONITORING AGENCY NAME(S) AND ADDRESS(ES)

Withheld

10. SPONSOR/MONITOR'S ACRONYM(S)

11. SPONSOR/MONITOR'S REPORT NUMBER(S)

12. DISTRIBUTION / AVAILABILITY STATEMENT

Distribution Statement A:
Approved for Public Release; Distribution Unlimited

13. SUPPLEMENTARY NOTES

This work is declared a work of the U.S. Government and is not subject to copyright protection in the United States.

14. ABSTRACT

This dissertation explores the benefits of combined control moment gyroscope (CMG) and reaction wheel array (RWA) actuation for agile spacecraft. Agile spacecraft are capable of slewing to multiple targets in minimum time. CMGs provide the largest torque capability of current momentum exchange actuation devices but also introduce singularity events in operation. RWAs produce less torque capability than CMGs but can achieve greater pointing accuracy. In this research, a combined RWA and CMG (RWCMG) system is evaluated using analytical simulations and hardware experiments. A closed-loop control scheme is developed which takes advantage of the strengths of each actuator set. The CMGs perform slews for a representative target field. Borrowing from variable-speed CMG theory, a system of switching between CMG and RWA actuation allows the RWA to assume control of the spacecraft when desired pointing tolerance is met for a given target. During collection, the CMG gimbals may travel along null motion trajectories toward preferred angles to prepare for the next slew. Preferred gimbal angles are pre-computed off-line using optimization techniques or set based on look-up tables. Logic is developed to ensure CMG gimbal angles travel the shortest path to the preferred values. The proportional-integral-derivative, quaternion feedback, and nonlinear Lyapunov-based controllers are assessed for the RWCMG system. Extended and unscented Kalman filter techniques are explored for improved accuracy in analytical simulation. Results of RWCMG hardware experiments show improvements in slew capability, pointing accuracy, and singularity avoidance compared to traditional CMG-only systems.

15. SUBJECT TERMS

Optimal, Satellite, Control

16. SECURITY CLASSIFICATION OF:			17. LIMITATION OF ABSTRACT	18. NUMBER OF PAGES	19a. NAME OF RESPONSIBLE PERSON
a. REPORT	b. ABSTRACT	c. THIS PAGE			Dr. Eric Swenson, AFIT/ENY
U	U	U	UU	168	19b. TELEPHONE NUMBER *(include area code)* (937)255-3636x7479 Eric.Swenson@afit.edu